Development of an Advanced Low Energy Focused Ion Beam System Based on Immersion Optics

Dissertation

zur Erlangung des Grades eines Doktors
der Naturwissenschaften

der Fakultät für Mathematik und Physik
der Eberhard-Karls-Universität zu Tübingen

vorgelegt von

Michael Rauscher
aus Hechingen
2006

Tag der mündlichen Prüfung:	31.07.2006
Dekan:	Prof. Dr. Peter Schmid
1. Berichterstatter:	Prof. Dr. Erich Plies
2. Berichterstatter:	Prof. Dr. Oliver Eibl

Meiner Großmutter Gretel Türk.

Contents

I Introduction 1

1 Introduction 3

2 FIB Systems in TEM Sample Preparation 5
2.1 State of the art TEM sample preparation 6
2.1.1 Conventional sample preparation 6
2.1.2 FIB technique 6
2.2 Use of low energy focused ion beam systems 8

3 Low Energy Focused Ion Beam System Design 11
3.1 Operation modes 12
3.2 Systems with target on ground 13
3.3 Systems with target on high voltage 19

II Numerical Simulation 27

4 Aberration-Optical Treatment 29
4.1 Fundamentals of the aberration approach 29
4.2 Method 30
4.2.1 Quantification of the probe size 30
4.2.2 System optimisation 33
4.2.3 Software 34
4.3 Results 36
4.3.1 Gun lens 36
4.3.2 Objective lens 38
4.3.3 In-lens scanning 40
4.3.4 Lens optimisation 41
4.3.5 Summary and overall system performance 43

5 Impact of Coulomb Interactions 45
5.1 Characterisation of Coulomb interactions 45
5.2 Previous studies on low energy systems 46

5.3 Method . . . 48
5.3.1 Software . . . 48
5.3.2 Quantification of the probe size . . . 49
5.3.3 System optimisation . . . 51
5.4 Results . . . 53
5.4.1 Overall system performance including interactions . . . 53
5.4.2 Fully optimised system performance . . . 54

III Experimental System 57

6 Liquid Metal Ion Sources 59
6.1 Proprietary sources . . . 59
6.2 Sources by the FZ Rossendorf . . . 60

7 Mechanical Design 61
7.1 System Components . . . 61
7.1.1 Gun lens . . . 61
7.1.2 Isolation valve and beam limiting aperture . . . 65
7.1.3 Stigmator and beam alignment unit . . . 68
7.1.4 Liner tube and objective lens . . . 69
7.1.5 Scan deflector . . . 70
7.2 Test setup design and preliminary experiments . . . 72
7.2.1 UHV test setup . . . 72
7.2.2 HV test setup . . . 73

8 Power Supply 77
8.1 Column supply . . . 77
8.2 Beam scanning and image acquisition . . . 79

9 Experimental results 81
9.1 Beam alignment . . . 81
9.2 Measurements . . . 83

IV Summary and Outlook 87

10 Summary 89

11 Outlook 91

List of Frequently Used Symbols and Abbreviations

$\Delta\phi$ .... potential equivalent to energy width, i.e. energy width divided by charge
ΔE .... energy width (full width at half maximum)
κ_1, κ_2 .... gun lens immersion ratio, objective lens immersion ratio
ϕ .... ion kinetic potential, i.e. ion kinetic energy divided by charge
d .... probe size (general)
d_v .... virtual source size
d_{50} .... probe size containing 50% of particles
d_{geo} .... geometric image of source
d_{RPS} .... probe size calculated using RPS algorithm
I .... beam current
z .... position along optical axis
z_o, z_i .... object position, image position
J_Ω .... source angular current density
E .... beam energy
M .... magnification
m .... ion mass
q .... ion charge
wd .... working distance
EHT .... Everhart-Thornley detector
FFLV .... field free low voltage mode
FFLV-R .... field free low voltage mode with retarding objective lens
FIB .... focused ion beam
GND .... ground potential
HV .... high vacuum
LEFIB .... low energy focused ion beam
LMIS .... liquid metal ion source
MBE .... molecular beam epitaxy
PMT .... photomultiplier tube
SE .... secondary electron(s)
SEM .... scanning electron microscope, scanning electron microscopy
SI .... secondary ion(s)

TEM .... transmission electron microscope, transmission electron microscopy
UHV .... ultra-high vacuum
$V_{booster}$ .... booster voltage, i.e. ground related voltage of liner tube
VLV .... very low voltage mode

Part I

Introduction

Chapter 1

Introduction

Since the first focused ion beam (FIB) instruments were made commercially available about 20 years ago, they have continuously been improved in design and performance. State-of-the-art systems employing gallium liquid metal ion emitters and operating at 30 keV energy are capable of generating ion probes of approximately 5-7 nm in diameter in high resolution mode (at beam currents of the order of a few pA) and current densities of larger than 10 A/cm^2 (with beam diameters of the order of a few hundred nm) in milling mode. However, somewhat similar to the much earlier developments in scanning electron microscopy (SEM), there now seems to be a fairly recent trend towards also exploring the low energy performance of FIB systems.

One major driving force behind this development is the requirement for a fast but gentle preparation technique for transmission electron microscopy (TEM) samples. With a reduced ion energy any sample damage, such as amorphisation of crystalline material or undesired ion implantation, induced through the projectile's impact onto the sample can be expected to be also reduced.

The use of low energy focused ion beams for TEM sample preparation was first addressed in Tuebingen by Gnauck [1], who developed a simple two-lens setup operating at 5 keV energy. The system was successfully used for *in-situ* postprocessing of microscopy samples directly inside the TEM. Also based on the experience gained with this earlier design, an improved system setup with further enhanced performance (i.e. smaller probe sizes) at even lower landing energies of 2-3 keV was envisaged. Work on the development of the system, which ultimately is also to be used as an add-on to a SEM or TEM, started within the framework of a joint bmbf project [2] and was later carried on in collaboration with industrial partners.

This present study aims at introducing the resulting system design and in particular its novel approach towards low energy focused ion beam operation. It will be shown that by employing the concept of immersion optics, similarly to its application in low voltage SEM, and focusing the lenses in internal acceleration mode, a very good system performance in terms of the achievable probe size for

a given beam current can indeed be achieved.

While the realisation of this particular operation mode requires an adapted design of individual optical components and also power supply units, the classical two-lens setup has been chosen for the ion beam column. In this, ions from a gallium liquid metal ion source (LMIS) are accelerated using a three electrode gun lens. An electrically insulated liner tube then allows setting the interlens drift space on high potential to enable immersion operation and the beam is focused to the grounded target by means of a three electrode objective lens. The last electrode of the latter is set on ground potential in order to keep the target region field-free.

Below the potentials and limitations of this novel approach to low energy FIB design will be discussed on the basis of intensive numerical simulation that also includes the effects of mutual Coulomb interactions within the ion beam. Additionally, the increased demands on the design of mechanical system components and electrical supply units will be discussed on the basis of a purpose-built laboratory setup. Employing the latter, experimental experience with the new operation mode could already be gained and initial results will be presented.

To put this study into context, the discussion of this system (chapters 4-9) is preceeded by the introduction of the prevalent methods of TEM sample preparation using focused ion beams in chapter 2, and a review on earlier low energy design approaches in chapter 3. From the latter it will become evident that the afore mentioned trend towards exploring the low energy performance of FIB systems may indeed be considered as a revival of an earlier interest.

Chapter 2

FIB Systems in TEM Sample Preparation

With the continuous downsizing of semiconductor devices, transmission electron microscopy with its subnanometer scale resolution is becoming increasingly important in integrated circuit failure analysis [3]. However, traditional specimen preparation techniques have somewhat encumbered the application of the TEM for day-to-day use in an industrial environment and only the advent of the focused ion beam technology has made a routine utilisation possible. With modern FIB systems high quality site-specific cross-section samples of layered materials may be prepared within only a few hours, thus allowing rapid failure identification and analysis. However, compared to conventional sample preparation techniques employing low ion beam energies ($\leq$6 keV, see below) the use of high energy (30-50 keV) focused ion beams inevitably leads to an increase in sample damage. Consequently, the removal or dimunition of this damage - using a variety of techniques - has been an issue for some time and one possible approach is the utilisation of lower landing energies within the framework of the FIB method. Clearly, the operation of a standard focused ion beam system at its lower energy limit, e.g. for a final processing/polishing step, is associated with a dramatic increase in probe diameter. Here systems resolution-optimised for the low energy regime may be beneficially utilised.

In this chapter, we briefly discuss the prevalent methods of cross-sectional TEM sample preparation involving the use of ion beams, with the main focus on the technological aspects of the FIB technique. Subsequently, the existing experimental experience with the utilisation of low energy focused ion beams in specimen preparation is reviewed.

Note that a somewhat similar account of the potential application of low energy FIB for the removal of damage layers in TEM samples has been compiled independently by Kato [4] and may be used for further reading.

2.1 State of the art TEM sample preparation

Cross-sectional TEM sample preparation in material science typically involves the fabrication of an electron-transparent area of interest within a solid-state sample taken from bulk material. The overall sample size is limited to about 3 mm in diameter with an electron-transparent area of approximately 100 nm in thickness (high resolution TEM: about 10 nm) and several square microns in size.

2.1.1 Conventional sample preparation

Traditionally, the preparation of TEM cross-section specimens employs a combination of mechanical premachining followed by low energy broad ion beam (BIB) milling [5]. The technique involves cutting the sample into sections that are subsequently glued together to form a sandwich-like structure. After embedding this into a thin-walled tube, the latter is sectioned into disks for mechanical and ion thinning. Typical BIB systems employ two (mostly argon) gas ionisation guns. The ion beam is aligned at a small angle of incidence of the order of 10° to the rotating specimen surface. The actual milling angle is used as a variable to set the milling conditions: for angles of incidence up to about 30° the thinning rate increases with increasing angle, as does the ion penetration depth and hence the size of any induced damage layer. Usually beam energies of 3-6 keV and beam currents of up to several hundreds of μA are used. Due to the relatively large probe diameters of the order of one milimetre the associated probe current densities are rather low. Consequently, milling rates are comparatively small and thus the process of specimen thinning may take up anything between several hours to several days. With many BIB systems sample positioning completely relies on accurate mechanical alignment and hence site-specific preparation is a particularly delicate task. Furthermore, any preparation success in terms of sample transparency can finally only be evaluated in the TEM. Although there are multiple potential sources for the generation of artefacts in the specimen, like deformation stress during mechanical thinning or structural changes due to sample heating under ion bombardment, direct ion induced damage seems to be of less concern. Indeed, BIB milling has been used to reduce damage layers in FIB prepared TEM lamellas [6–8].

2.1.2 FIB technique

Having only been developed about 15 years ago [9, 10] the focused ion beam technique for preparing site-specific cross-sectional TEM samples is still comparatively recent. The vast majority of FIB systems are based on the use of gallium liquid metal ion sources and are optimised for beam energies of 20-30 keV. Probe diameters as small as 7 nm allow high-resolution imaging of the sample and accurate position control of the cross-section specimen. Beam currents are typ-

ically ranging from several pA (high-resolution) to several nA with associated beam current densities of up to 12 A/cm^2 [11]. Preparation can almost directly be done from bulk material using either the "trench" or "liftout" technique with only a minimum of additional mechanical pre- or post-processing steps [12]. Both methods involve the deposition of an about 1.5 μm thick metal strap on top of the region of interest within the FIB system. Using large beam currents (3-20 nA) the substrate material on either side of the metal is then removed to leave a lamella approximately 10-30 μm long and 5-20 μm deep. Using a reduced beam current of about 1 nA the lamella is thinned further to a width of about 200-500 nm. In order to reduce the amount of tapering of the final cross-section, the specimen is then tilted to small angles (1°-4° depending on the material) and further material is removed until the intended thickness is reached. The final thinning steps are performed by tilting the specimen to positive and negative angles in turn and removing about 30 nm of material at a time to balance the stress that can build up at the sidewalls during ion thinning. The liftout technique further involves the cutting free of the thus prepared lamella and its transfer onto a thin support membrane using a micromanipulator. This last transferring step still limits the yield of the method to 50-95% whereas the yield in the trench method is close to 100%. On the other hand, specimens prepared by the trench method allow only limited tilt angles within the TEM and may give rise to falsified signals during energy dispersive x-ray analysis. It should also be noted that further advancement has been achieved by combining focused ion beam systems with conventional scanning electron microscopes (early work carried out by Sudraud *et al.* [13]). This setup allows completely non-destructive (SEM) imaging of the specimen and the observation of the FIB preparation process as well as a first assessment of the final lamella's electron transparency [14].
Generally, the FIB method is thus capable of producing a cross-sectional TEM sample within only about two hours. Furthermore, compared to the BIB technique, focused ion beam milling appears to be less material specific [7, 15], thus making it particularly useful with layered materials. As already mentioned with an appropriate choice of the milling angle, specimens with near parallel sides may be prepared. On the other hand, the inevitable degree of sample damage induced by the high energy ions still poses a problem (Fig. 2.1). Direct implantation of gallium ions into the specimen can lead to substantial concentration values [15, 16]. In the context of TEM sample preparation the issue of sidewall damage is even more important. Apart from removing material from the sidewalls of the lamella during preparation the highly energetic ion beam will also induce some ballistic damage to the remaining matter. The resulting width of the damage layer is highly material specific and strongly dependent on the ion energy and the angle of incidence. For crystalline silicon a typical value for the amorphisized layer thickness is about 20 nm (see discussion in the next section). With the lamella being only about 100 nm tick the damage layer thus constitutes roughly 40% of the total specimen. A comparison of HRTEM images of samples

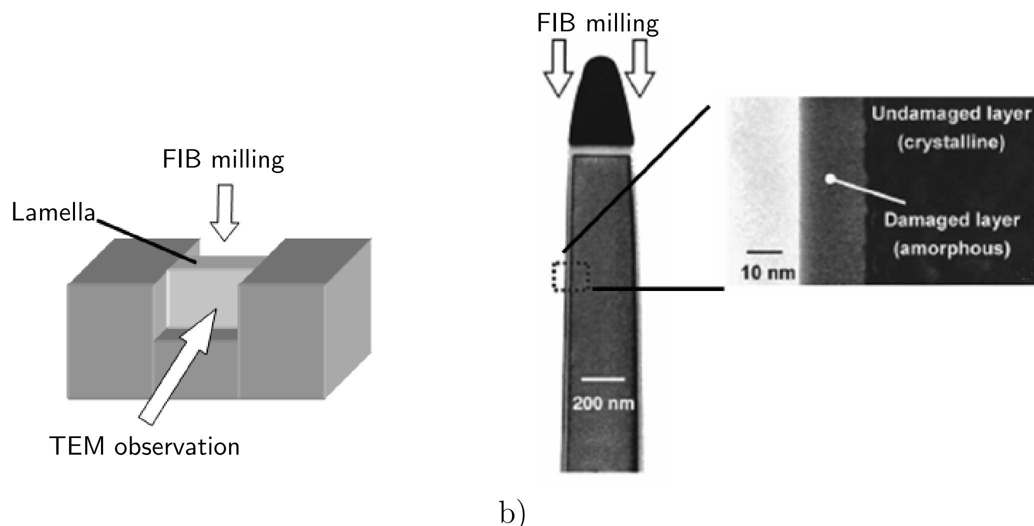

Figure 2.1: TEM sample preparation using FIB. (a) Schematic view of a specimen lamella prepared from bulk material. (b) Low magnification TEM image (lateral view) of lamella showing sidewall damage due to 30 keV FIB irradiation (from [6]).

with and without minimised damage layers, respectively, showed a significantly reduced and anomalous contrast in the latter case [6,17]. Numerous technological approaches exist for minimising the thickness of the damaged layer, such as the optimisation of the angle of incidence [18] or using a reactive halogen gas as an etchant (gas-assisted etching) [17]. Besides, intensive work has been undertaken to remove or at least reduce the damaged layer in a processing step succeeding the FIB milling (see [6] for a brief overview). Here the use of low energy ions either using the BIB or FIB method seems to be most promising.

2.2 Use of low energy focused ion beam systems

In order to overcome the aforementioned problems of gallium implantation and specimen amorphisation associated with the use of high energy ions, several authors have explored the possibilities of employing a lower beam energy within the framework of the FIB method for TEM sample preparation. Due to the optical system layout, however, the minimum practical energy at which an acceptable resolution is retained seems to be about 5 keV [19]. Furthermore, using a standard FIB system setup equipped with only unipolar power supplies the minimum possible energy may indeed be limited by the extraction voltage of the LMIS, i.e., typically 7-10 keV. To our knowledge, only semiconductor materials were investigated, with a focus on crystalline silicon and it should be noted that the latter seems to be particularly sensitive to ion bombardment [8]. The amount of damage was typically assessed using cross-sectional TEM images of FIB prepared lamellas. Walker *et al.* [21] compared the damage induced by 30 keV and 10 keV

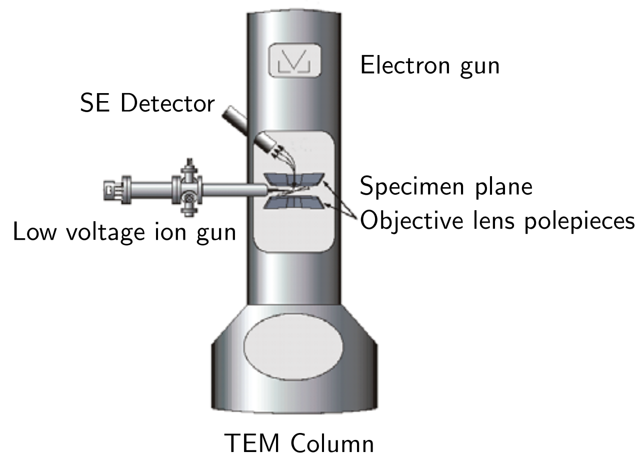

Figure 2.2: Schematic arrangement for TEM *in-situ* low voltage ion milling (drawing adapted from [20]).

focused ion beam milling, respectively, for the three most commonly used semiconductors: silicon, gallium arsenide, and indium phosphide. They found that in the case of low energy normal incidence milling, the width of the damage layer could be reduced by up to a factor of 6 in the case of GaAs compared to the high energy case. However, they also pointed out, that usually glancing angles are used during the final milling stage and that the observed damage layers for the high energy ions thus somehow represent worst case values. A thorough investigation of means of reducing the side-wall damage in TEM lamellas was presented by Kato *et al.* [6]. Cross-sections of crystalline silicon with a thickness of 100 nm were prepared by 30 keV ion milling and the amorphisation layer was found to be 20 nm wide on both sides, resulting in a total specimen amorphisation of 40%. The width of the damage layer was found to be independent of the beam current in the range of 100 to 400 pA. Using 10 keV FIB postprocessing with a beam current of 250 pA the damage layer could be reduced to 10 nm. This value was found to be only slightly larger than the value of 8 nm obtained using argon broad ion beam milling with a beam energy of 3 keV. Langford *et al.* also investigated the influence of low energy post-processing of a 100 nm silicon lamella. The original width of the damage layer after 30 keV FIB milling at an angle of incidence of 1.2° again was found to be 20 nm. For final polishing with an ion energy of 5 keV (beam current 100 pA) the specimen had to be tilted by 10° in order to be still visible. The damage layer was thus reduced by a factor of two. Additionally using iodine as etchant gas did not further improve this value. The amount of gallium in the amorphous layer was reduced by approximately a factor of 2.5 by reducing the energy from 30 kev to 5 keV. However, the same reduction was observed when using iodine gas assisted etching at 30 keV. The immediate use of low energies was studied by Liu and coworkers [22]. The original width of

amorphous silicon could be reduced from approximately 40 nm obtained by 30 keV ion milling to 14 nm at 10 keV (normal incidence values). In both cases the beam current was set to 5 nA. The processing time, however, increased from 45 minutes (30 keV) to 120 minutes (10 keV). When using a 5 keV ion beam with a probe current of 10 nA the damaged layer was found to be 32 nm, which the authors attributed to beam stability problems associated with an "unacceptable" rise in milling time. A possible combination of high energy milling with a final low energy processing step was also investigated in this study. An optimum value for the damage layer width of slightly less than 11 nm was found for 5 keV final milling energy in combination with a small tilt angle of approximately 5°. A similar procedure (again using silicone) was applied by Engelmann [8]: after 5 keV final milling in combination with a tilt angle of ±7° the width of the amorphisized layer was reduced from originally 17 nm to 7 nm. The author also notes that postprocessing using 10 keV beam energy did not result in any reduction of the damage layer. Gao *et al.* [23] again explored the possibilities of direct sample preparation employing 10 keV ions. They found a damage layer of 11 nm as opposed to 23 nm for the high energy case. These values are reported to be approximately constant for the investigated current range of 30 pA to 1 nA and independent of a particular choice of a (small) tilt angle.

A somewhat different approach was taken by Gnauck and Burkhardt [1, 20]. They used a dedicated low energy FIB system (see also section 3.2) for post-processing of TEM lamellas *in-situ*. The system was mounted onto a free port of the TEM's objective lens as shown in Fig. 2.2. The setup was successfully used for thinning of TEM lamellas as well as removal of oxide layers that usually build up during the transfer of the sample from the preparation tool to the TEM. The system worked effectively with an energy of 5 keV and a beam current of approximately 1 nA. The beam diameter was limited to a few microns.

Only very recently the successful operation of standard high energy FIB systems (by Zeiss and FEI) at 2 keV energy for removing amorphous layers in TEM lamellas has been reported [24]. The final polishing was accomplished using a beam current of 100 pA and a total milling time of 10-60 s. The probe size was estimated to about 1 μm (maximum intensity) with a tail intensity of approximately 70 μm in diameter.

Chapter 3

Low Energy Focused Ion Beam System Design

While the very first focused ion beam systems based on the use of liquid metal ion sources were designed for high energy operation [25], many researchers from an early stage also explored the possibilities and limitations of generating low energy beams. At the time the particular interest mainly originated from the potential application of LEFIB within semiconductor device fabrication processes where ion energies of the order of a few 100 eV were used (an overview is given in [26]). Although the (physical) sputter rate is virtually negligible in this energy regime, the ions still possess the capability of enhancing processing steps like chemical reactions while inducing only minimum damage, e.g., amorphisation in the case of crystalline samples, to the underlying substrate. More recently, as outlined in detail above, the application of low energy ion beams for micromachining in TEM sample preparation has been investigated. However, the energies used for this purpose are comparatively higher, typically ranging from 1-5 keV.

In any of these applications the retention of a sufficiently high resolution (small probe size) for beam position control, e.g. by means of scanning ion microscopy, is an important issue. In order to limit the increasing influence of both, the chromatic aberration as well as the Coulomb interaction contribution the overall probe size with decreasing energy a suitable choice of system/lens design and mode of operation has to be made.

In this chapter - following some introductory considerations - an attempt is made to review existing low energy focused ion beam design approaches. Note however, that only systems will be considered where experimental data has been made available. For a rough classification - from a more practical perspective - the systems are discussed according to whether the target is held on ground or high tension.

3.1 Operation modes

For the majority of systems discussed in the following sections, the designers did not consider Coulomb interactions to be the limiting factor in the achievable probe size. Calculations carried out by Narum and Pease [27] and Hirohata *et al.* [28] both indicated a negligible effect of mutual ion interactions below beam currents of approximately 10 nA (see section 5.2). Consequently the main focus in system design was on the minimization of the chromatic aberration disc.

In order to balance the increase in $\Delta E/E$ with decreasing landing energy, the chromatic aberration coefficient must be reduced. Here the use of immersion objective lenses in which the object is placed on the low energy side of an decelerating immersion lens is one well known promising approach from modern low voltage scanning electron microscopy. In fact also the very first scanning electron microscope for low energy surface observation employed an immersion objective lens to decelerate the electron beam close to the specimen [29] - for a review on low energy electron microscopy see [30]. In the special case of an arrangement where the target is being "immersed" in a - usually - strong electric field and might thus itself be considered as a constituent of the immersion lens, the terms cathode lens, immersion objective or very low voltage mode (VLV) (according to Rose and Preikszas [31]) may be used. This denomination refers to both, the frequent application of this type of immersion lens as objective lens in a photo (or low energy) electron emission microscope as well as the typical "landing" energy range of the order of 10 eV. In case of an immersion lens where beam retarding is accomplished within the lens itself, i.e. the same potential is applied to the final objective lens electrode and the target, the term field-free low voltage mode (FFLV) has been proposed [31]. However, to prevent confusion, in the following the term FFLV-R mode will be used instead - the "R" indicating the retarding action of the lens. Furthermore, in the following the term acceleration will generally be employed, in particular also for negative acceleration, i.e., deceleration.

As already pointed out by Recknagel [32] any cathode lens may be regarded as a combination (doublet) of an acceleration lens and a focusing lens. Consequently the total chromatic and spherical aberration coefficients, C_c and C_s, respectively, may also be considered as being composed of acceleration and focusing lens contributions. With very low voltage mode operation the total aberration coefficients are dominated by the accelerating lens and may be approximated by [33]:

$$
\begin{aligned}
C_c \approx C_s &\approx l\frac{\phi_{\text{target}}}{\phi_{\text{accel}}}\,\frac{\phi_{\text{accel}}^{1/2} - \phi_{\text{target}}^{1/2}}{\phi_{\text{accel}}^{1/2} + \phi_{\text{target}}^{1/2}} \qquad (3.1)\\
&= l\frac{\phi_{\text{target}}}{\phi_{\text{accel}}}\,\frac{1 - \left(\frac{\phi_{\text{target}}}{\phi_{\text{accel}}}\right)^{1/2}}{1 + \left(\frac{\phi_{\text{target}}}{\phi_{\text{accel}}}\right)^{1/2}}
\end{aligned}
$$

$$\approx \quad l\frac{\phi_{\text{target}}}{\phi_{\text{accel}}} \approx \frac{\phi_{\text{target}}}{E_{\text{accel}}} \qquad\qquad \text{for } \phi_{\text{target}} << \phi_{\text{accel}}$$

where l is the distance over which the kinetic potential changes from ϕ_{accel} (kinetic potential within the ion column) to ϕ_{target} (kinetic potential at the target) and E_{accel} denotes the acceleration field. Note that $\phi_{\text{accel}}/\phi_{\text{target}}$ is often referred to as the (target-side) immersion ratio (where the definition has been chosen to yield values > 1). With typical landing energies of 10 eV - corresponding to a kinetic target potential of 10 V - and an acceleration potential of the order of 10 kV very small aberration coefficients can be realised.

In the case of FFLV-R mode operation the aberration coefficients of the acceleration lens are approximately given by [33]:

$$C_c \approx C_s \approx \frac{1}{2}\left(wd + l\left(\frac{\phi_{\text{target}}}{\phi_{\text{accel}}}\right)^{1/2}\right)\left(1 - \frac{\phi_{\text{target}}}{\phi_{\text{accel}}}\right) \tag{3.2}$$

Note, however, that in this case the aberration coefficients of the focusing lens can usually not be neglected. Consequently, compound electrostatic and magnetic lenses are used in low voltage scanning electron microscopy - with the magnetic part taking over the focusing action [34,35]. As a rule of thumb, the chromatic and spherical aberration coefficients of an electrostatic Einzel lens are larger than the corresponding values of a magnetic lens by a factor of two and four, respectively.

Despite the obvious advantages of using immersion lenses for generating low energy ion beams, objective lenses in Einzel lens mode - with the final electrode and the target being set on ground potential - have also been widely used. In this case systems are operated as in the high energy mode with a grounded final gun/condenser lens electrode. As this mode of operation is also characterised by a field-free region between the final objective lens electrode and the target it may equally be termed field-free low voltage mode. Hence - as indicated above - for a refined classification the terms FFLV and FFLV-R will thus be used (cf. fig. 3.1 for a graphical representation of the introduced operation modes). With the beam energy being comparatively low within the entire column in FFLV mode, Coulomb interactions may become a limiting factor and the system's performance is typically inferior compared to VLV or FFLV-R mode operation.

3.2 Systems with target on ground

Obviously, the most straightforward way to generate a low energy ion probe is to operate a high energy system at its lower energy limit in FFLV mode. For older

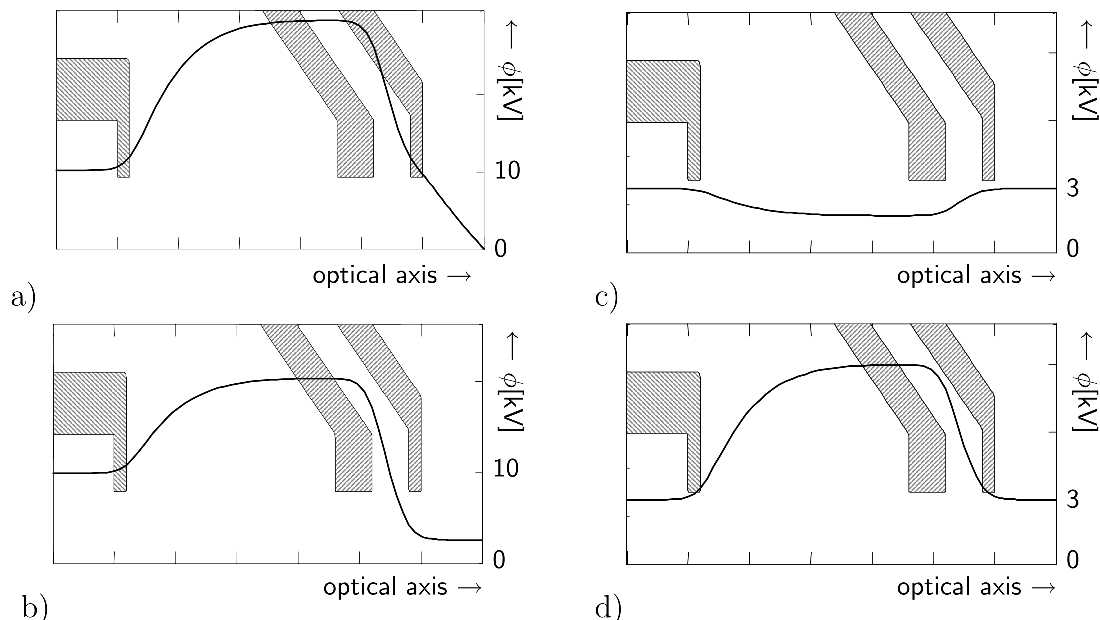

Figure 3.1: Schematic representation of four different modes for low energy focused ion beam system operation. Illustrations show part of the three electrode objective lens together with the course of the axial kinetic potential of the beam ϕ for a) VLV mode, b) FFLV-R mode, c) FFLV mode (internal deceleration focusing), and d) FFLV mode (internal acceleration focusing) operation. The target is assumed to be situated on the right boundary.

column setups the minimum energy may well have been limited by the smallest possible value of the extraction potential at which a sufficiently stable ion emission is obtained. The reason for this is the fact that the extraction voltage power supply initially was in many cases unipolar, i.e. it could only supply voltages ≤ 0 V with respect to the source voltage. Even though by using a bipolar supply, also very low beam energies could in principle be realised with this approach, it has mostly been employed for energies of 3 keV or higher. As indicated previously, one reason for this is the increasing influence of the chromatic aberration and the Coulomb interaction contribution to the total probe size at very low energies, respectively.

Orloff *et al.* [36] reported measurements (employing the knife-edge method) of a 5 keV energy ion probe using a two-lens column setup with a clear working distance of 25 mm [37]. Probe diameters of 159 nm, 480 nm, and 691 nm were obtained for beam currents of 250 pA, 1 nA, and 4 nA (angular current density 20 μA/sr), respectively. Interestingly, for the higher beam currents the values were found to be considerably smaller than obtained from third-order aberration-optical calculations, which predicted a dominant influence of the spherical aberration contribution (diameter calculated as 0.5 $C_s\alpha$, α denoting the image-side aperture) This finding was accredited to the fact, that by properly adjusting the

objective lens' excitation the image/measurement plane can be reconciled with a plane in which probe sizes much smaller than the "spherical limit" may be obtained.

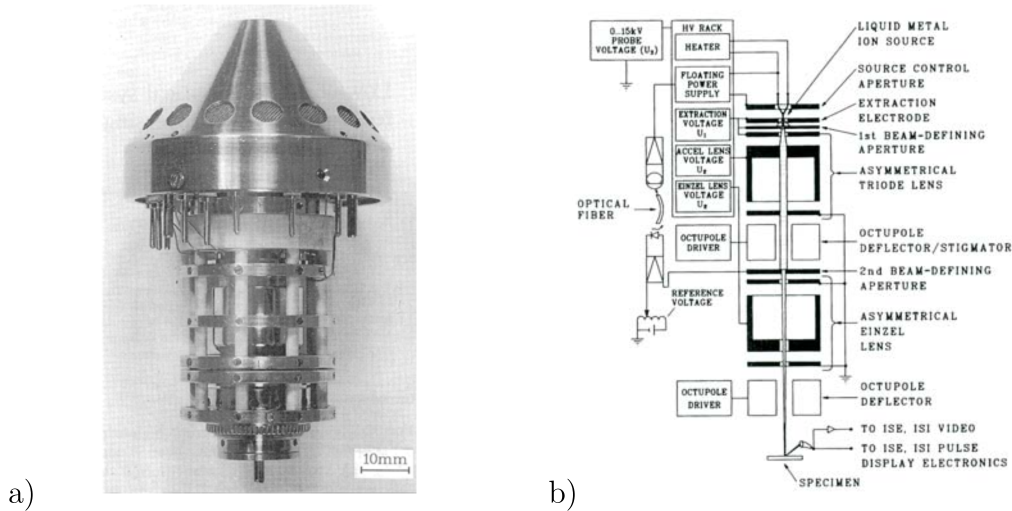

Figure 3.2: a) Photography of the compact column setup and b) schematic drawing of the ion-optical system designed by Driesel (figures from [38])

A modified commercial (FEI Company) single-lens FIB column mounted on an UHV chamber was used by Shedd and Russell [39] for studying the effects of low energy ion impacts on a graphite substrate. For energies as low as 250 eV the system was operated in the FFLV mode, whereas for lower energies the sample was biased positively to further decelerate the positive ions (see next section). Apparently, sufficient focusing, i.e. small enough ion probes, for beam current measurement with a Faraday cup was only possible for energies $\geq$ 1 keV.

Ion beam assisted etching of silicon using chlorine gas as etchant was studied by Komuro [40]. Gallium ions with an energy of 5 keV were employed. The beam diameter was reported to be 50-120 μm with an associated beam current density of 20-60 μA/cm^2 but no further information on the ion optical system was published.

Steckl *et al.* [41, 42] employed a MicroBeam Inc. NanoFab 150 for studying the effects of low energy ion implantation in silicon with energies of 3, 5, and 10 keV. A probe size of 1 μm at 5 keV energy and a probe current of 300 pA was reported [43].

A remarkable dedicated low energy two lens FIB system - similar to the design of Orloff [37] - was presented by Driesel [44]. The compact column design is shown in fig. 3.2 together with a schematic drawing of the ion optical system. A specially designed galllium LMIS provided stable emission (emission current $\approx 3\mu$A) at an extraction voltage of only 3 kV. The system performance was further improved by enabling internal acceleration mode (accel mode) focusing for both condenser/gun as well as objective lens. With this focusing mode the beam energy inside the lens is typically higher than outside and aberration coefficients are generally smaller

compared to deceleration (decel) mode focusing for which the beam energy inside the lens is mostly lower than outside. However, the required focusing voltages may become critical and special care has to be taken to avoid leakage currents or flashovers between adjacent electrodes. In order to allow accel mode focusing for the condenser lens at practical voltage values the source distance had to be increased. However, as this increase inevitably also results in an increase of the lens' aberration coefficients, a source distance value of 8 mm was chosen as trade-off. The probe size was determined experimentally at a clear working distance of 30 mm by means of the knife-edge method on a copper grid bar. The values obtained were generally in good agreement with theoretically predicted values. For a beam energy of 3 keV the smallest probe size measured was 0.2 μm at a beam current of 60 pA (probe current density 0.2 A/cm^2). For a beam current of 1.6 nA a probe size of 0.6 μm was found (probe current density 0.6 A/cm^2).

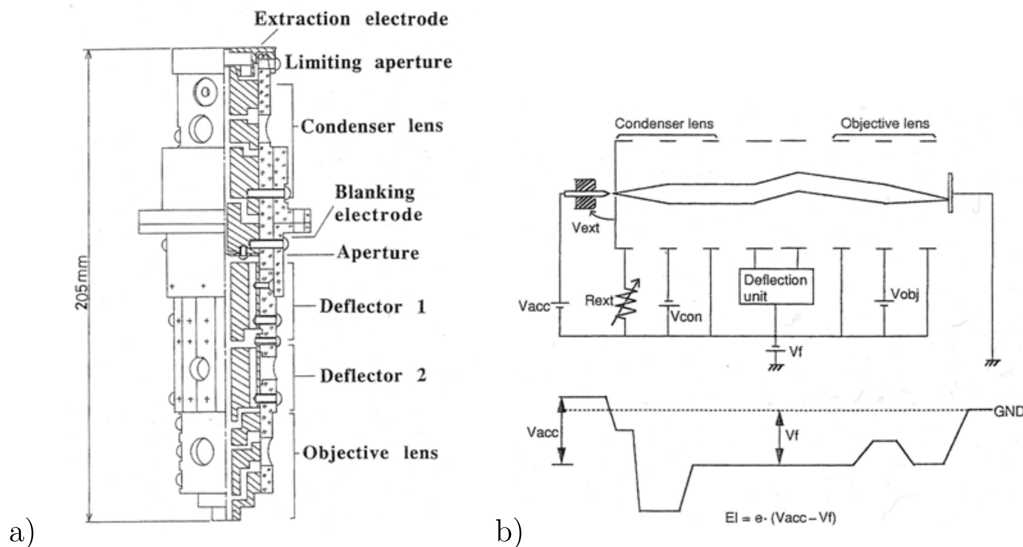

Figure 3.3: a) Schematic drawing of the optical column designed by Pak *et al.* b) Corresponding course of electric potential (figures from [45]).

An advanced system was designed by Pak *et al.* [45,46] and is shown schematically in fig. 3.3 together with the corresponding course of the potential. After extraction from a LMIS the ions were accelerated to a high potential (ϕ_{accel} = 8-10 kV) and subsequently focused by two Einzel lenses (according to fig. 3.3 b) the first and second lens employed internal acceleration and deceleration mode focusing, respectively). A beam alignment/deflection unit was placed in the intermediate lens space on high potential. The beam was finally decelerated by the retarding field between the objective lens final electrode and the grounded target. From calculations a probe size of approximately 500 nm and 250 nm were expected for a source aperture angle of 3 mrad at energies of 100 eV and 3 keV, respectively. Measurements of the probe diameter were carried out using directly

deposited gallium films on a Si substrate at an acceleration voltage of 8 kV and a beam current of 4.4 nA. The irradiation time was set to 10 sec. and values of 6.7 μm, 6.9 μm, and 7.4 μm were found for energies of 50 eV, 30 eV, and 10 eV, respectively. These values were found to be in fairly good agreement with calculated data.

Nebiker *et al.* [47] again modified a commercial (Raith/Orsay Physics) system to operate at low energy. For a landing energy of 4 keV the system was operated in FFLV mode with both the condenser lens as well as the objective lens operated as Einzel lenses. In the case of the condenser lens this was made possible by realising stable ion emission at 4 kV extraction voltage. For lower energies the system was operated in VLV mode by positively biasing the sample (see next section). No probe size measurements were published for the 4 keV landing energy. However, measurements were published for a beam energy of 5 keV in an earlier publication [48]. Here a probe size of 662 nm at a beam current of approximately 80 pA was obtained using the knife-edge method.

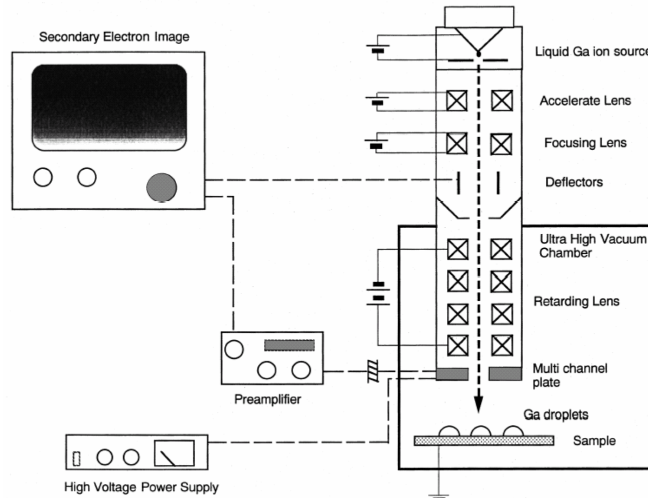

Figure 3.4: Schematic drawing of the low energy focused ion beam column designed by Chikyow *et al.* (figure from [49]).

Chikyow and coworkers [49,50] report on a system design similar to that of Pak *et al.* (see above) in which the ions are initially accelerated to comparatively high energy (10 keV) and subsequently retarded within a multi-electrode decelerating lens to their final energy. Unfortunately, the available details on the optical system are rather imprecise. Three lenses were employed, and while the voltage allocation remains somewhat unclear, apparently the optical concept of FFLV-R mode operation has been adopted. The setup was used for direct deposition of gallium droplets on a sulfur terminated GaAs substrate and the probe size was estimated to be about 5 and 10 μm at 100 and 30 eV ion energy, respectively.

A dedicated 5 keV ion beam system was developed by Gnauck [1] (based on an earlier design by Mayer [51,52]) for *in-situ* specimen finishing inside the TEM. The two lens system consisted of a gun lens (source distance 2 mm) based on a slightly modified Orloff/Swanson design [37] and a symmetric three electrode objective lens. An additional pair of deflection plates was assembled in front of the usual (postlens) scanning plates which were used to pre-compensate for the deflection of the ion beam within the field of the TEM objective lens. Gallium ions were extracted from specially fabricated LMIS at approximately 3.5 kV extraction voltage. The angular intensity of the sources for emission currents of 1-2 μA was measured to about 10 μA/sr. Due to the intended application the system was designed for a clear working distance of 35 mm. System performance was characterised by scanning the ion beam across a rough copper grid bar (TEM 100 mesh, i.e. 100 lines/inch) in low magnification (fig. 3.5a)). The results are summarised in fig. 3.5b).

Only very recently the operation of state-of-the-art high energy FIB systems (Zeiss Cross Beam 1540 and FEI Strata 400 DB) at 2 keV energy (FFLV mode) with surprisingly good resolution has been reported [24]. The probe size was estimated by analysing the spot mode profile after 1 minute milling at 500 pA beam current. The maximum intensity region was roughly estimated to about 1 μm with a significant intensity tail of approximately 70 μm in diameter.

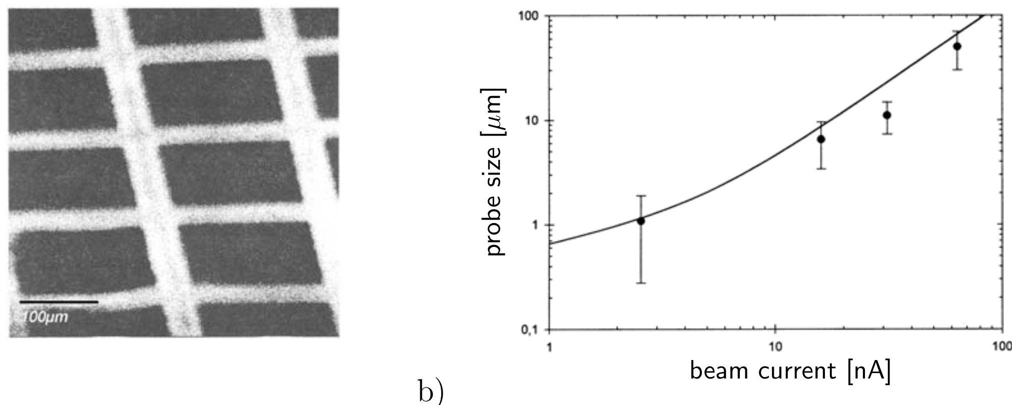

Figure 3.5: a) Exemplary ion induced secondary electron image used for probe size quantification by Gnauck (estimated resolution approximately 6.8 μm). b) Measured (data points) and calculated (line) system performance. All figures adapted from [1].

3.3 Systems with target on high voltage

Generating a very low energy ion beam using a commercial high energy FIB system operated in VLV mode may be accomplished by setting the target on high potential with the distinct advantage that no changes to the ion optical column itself are necessary. Somewhat surprisingly, only a small number of publications report on using this approach - although clearly not all applications might have been published or indeed been retrieved in a literature review. In order to keep insulation requirements for the target moderate the beam energy within the column is often chosen as low as practically possible - e.g. as forced by the smallest extraction voltage that allows stable ion emission. Consequently, the system performance of the dedicated high energy systems deteriorates, possibly also due to an increase in Coulomb interactions within the column. And even the improvement in aberration coefficients of the objective lens in VLV mode operation as indicated in equation (3.2) obviously cannot compensate entirely for this. Note however, that the obtainable probe size or current density was apparently of less concern for the scientists using this approach, as their focus clearly was on fundamental research relating to possible applications of low energy ion beams.

Shedd and Russell [39] used a single lens focused ion beam system by FEI for investigating the effects of low energy gallium ion irradiation of graphite. The ion energy within the column was 250 eV and for landing energies below that value the target was biased positively. Although this made insulation requirements less stringent, the authors report that sufficient focusing (i.e. for Faraday cup probe current measurements) could only be realised for energies $\geq$ 1 keV. Hence no data on the probe characteristics has been published.

As mentioned in the previous section Nebiker *et al.* [47] used a Raith/Orsay Physics FIB for generating a low energy ion beam. Ions were extracted from an alloy LMIS and subsequently selected by means of a Wien filter (resolution $m/\Delta m = 60$). Ion species employed were gallium, silicon, gold, and gold clusters at landing energies as low as 40 eV. The ion energy within the column was 4 keV. Signal detection was realised by measuring the probe current transmitted through a fine copper grid. From transmission images of a 1000 mesh copper grid placed on top of a Faraday cup, the probe size of a Au beam was estimated to 3 μm at a total beam current of 200 pA.

A simple single lens (possibly self-constructed) ion beam column was used at the Cavendish laboratories at Cambridge University [53–56] for three-dimensional semiconductor device fabrication. The system was mounted on an UHV chamber and used in combination with a molecular beam epitaxy (MBE) system (VG V80H MBE) for *in-situ* processing. The ion beam energy within the column was 1-2 keV (i.e. liner tube kinetic potential ϕ_{lt} = 1-2 kV) and for lower energies the sample was biased positively up to 1950 V. The system was operated with Sn and Si employing a Wien filter for mass separation. For the Sn ions a probe size of $<$ 20 μm at a working distance of 450 mm at a beam current of 1.2 nA and a beam

energy of 50 eV has been reported [53]. For Si^{2+} ions a value of approximately 30 μm at 1.1 nA beam current and an energy of 100 eV was found [56].

Even though these systems were undoubtedly used for important research issues, they are from an optical engineering point of view rather nondescript. However, apparently originating from the growing interest in the application of low energy ion beams in semiconductor device manufacturing/mask repair, several groups started designing dedicated ion beam systems for very low energy operation at a comparatively large scale in the 1980s. Basically four different development lines may be distinguished that will be discussed in some detail in the following. Note that concluding from available publications, research on this type of systems apparently seized in 1997/1998.

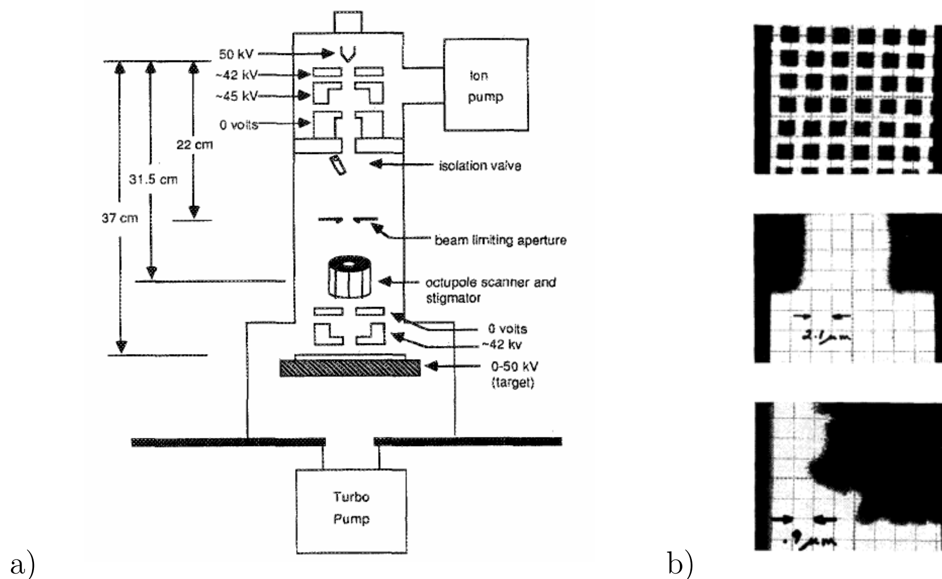

Figure 3.6: a) Schematic drawing of the optical column designed by Narum and Pease. Voltages refer to a source potential of 50 kV. b) Transmission ion images of a 1000 mesh nickel grid (gallium ions, ϕ_{accel} = 30 kV, I_{beam} = 1 nA, aperture diameter 100 μm). Low magnification (top), high magnification (middle) at ϕ_{target} = 25 V, and high magnification (bottom) at ϕ_{target} = 30 kV (figures from [57]).

Possibly the first publication proposing a dedicated low energy ion beam system employing a target on high potential is that by Yau *et al.* [58]. In [27] Narum and Pease notified the development of a low energy ion beam column to be integrated in a MBE system for *in-situ* processing of advanced semiconductor device structures. Experimental data was made available in 1988 [57, 59]. The system (schematically shown in fig. 3.6a)) employed an asymmetric gun lens to accelerate the ion beam to 30-50 keV. The target was used as the objective lens' final electrode and was kept at 0-50 kV resulting in a variable landing energy ranging from 50 keV (no retarding) to zero, i.e. complete retarding. The distance between

the final focus electrode and the target was 10 mm. For resolution measurements a special target electrode was used with 1 mm bore and a shallow countersink to mount a TEM grid. The transmitted ion current was collected by a Faraday cup. The probe size was estimated using the knife-edge method as well as by visual observation of transmitted current images (see fig. 3.6b). Assuming an acceleration voltage of 30 keV and a beam current of 1 nA the probe size was predicted to be 680 nm at 100 eV landing energy and 315 nm at 3 keV landing energy, respectively. Corresponding experimental values of 810 nm and 550 nm were found for a gallium beam (assumed source data: ΔE = 10 eV, J_Ω=20 μA/sr, d_v=50 nm). At the minimum energy of 25 eV a probe size of 950 nm was measured. A slightly modified version of the system for application in phase-shift mask repair was discussed in [60]. The basic idea was to further improve the system performance by introducing an additional (separate) final objective lens electrode to reduce the ratio of $\phi_{\text{target}}/\phi_{\text{accel}}$ in equation (3.2) thereby also reducing the aberration coefficients. Besides, the adaptation of a microchannel plate as a secondary electron detector directly below the final objective lens electrode was proposed. Although it was theoretically shown that the system performance could significantly be improved by these changes to the optical system, no measurements of the probe size or beam current were published. Nevertheless the system was successfully used for sputtering quartz substrate with energies ranging from 500 eV to 30 keV.

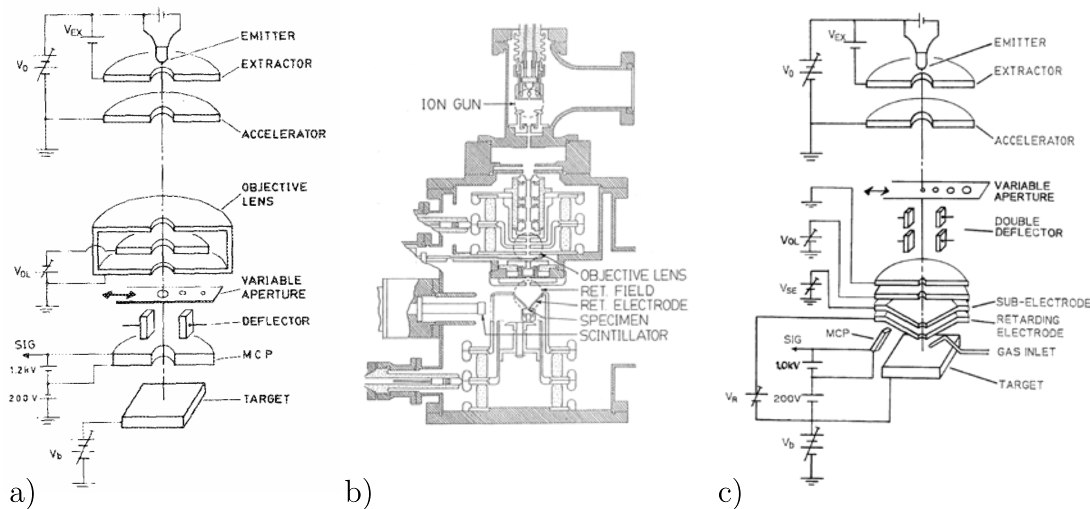

Figure 3.7: Low energy ion optical systems designed by Kasahara and co-workers. a) Schematic drawing of the original optical column (1988, [61]). b) Further improved design with retarding electrode (1989, [62]. c) Setup including additional sub-retarding electrode (1990, [63]).

Kasahara *et al.* [61] employed a simple gallium FIB column (assumed source data: ΔE = 10 eV, J_Ω=10 μA/sr, d_v=50 nm) with a single Einzel lens operated

in internal acceleration mode as shown in fig. 3.7a). The ion beam was initially accelerated to an energy of 30 keV and retarded at the target. First-order optical properties and aberration coefficients were calculated using programs by E. Munro [64]. In VLV mode operation (ϕ_{target} = 1 kV) $C_{s,i}$ and $C_{c,i}$ were calculated to be 390 mm and 1 mm, respectively, whereas in high energy operation (ϕ_{target} = 30 kV) the coefficients were found to be 12 000 mm and 87 mm, respectively. Signal detection for image acquisition was carried out using a scintillator for detecting secondary electrons in FFLV mode and a microchannel plate for detecting ions in VLV mode. From SI images the resolution was estimated to 0.1 μm, 0.2 μm and 0.2-0.3 μm for landing energies of 10 keV, 5 keV, and 1 keV, respectively, at a probe current of 100 pA. In a further publication [62] the authors adressed the particular problems encountered when exposing the target to a retarding field in VLV mode operation. In particular, the clearly inferior signal-to-noise ratio in the SI images compared to standard SE images due to the comparatively lower SI yield was discussed. The system was thus expanded in order to enable SE detection also in VLV mode. This was achieved by incorporating an additional electrode into the system that was kept on the same voltage as the target, thus making the target region field-free and - strictly speaking - changing to FFLV-R mode. Several geometrical configurations for the shape and the assembly of this so-called retarding electrode were investigated. Common to all designs was the fact that the optical properties were worsened compared to the setup without additional electrode. A cross-sectional view of the experimental system is shown in fig. 3.7b). Unfortunately, the predicted performance could not be verified experimentally as the image quality of the SE images deteriorated strongly when lowering the landing energy to values below 2 keV. In order to restore some of the (theoretical) system performance lost due to the incorporation of the additional electrode a design was introduced [63, 65] in which the optical system was further expanded by a further electrode (sub-retarding electrode) assembled directly above the retarding electrode (see fig. 3.7c)). The approach by Kosugi *et al.* [63] was based on the original system [62] but with an acceleration voltage of only 15 keV. Experimentally a probe diameter of 2.5 μm at 1 keV landing energy and a probe current of 300 pA was measured, which was in fairly good agreement with calculated data. The similar setup by Sawaragi *et al.* [65] was designed for an acceleration energy of 70 keV. At a landing energy of 3 keV a probe size of approximately 180 nm at 100 pA probe current was predicted. Measurements however were only published for landing energies of $\geq$ 11 keV as the SE detection efficiency was strongly decreasing with decreasing landing energy. The objective lens design was also used in a combined focused ion and electron beam system [66]. Here the ion probe size was estimated by SI imaging to be 300 nm at 45 pA probe current at a landing energy of 1 keV - about three times the predicted value. The acceleration energy of the beam was chosen to be 25 keV. The column design was later expanded by a mass filter and studied as a FIB lithography system for the energy range of 10-160 keV (single charged ions) [67].

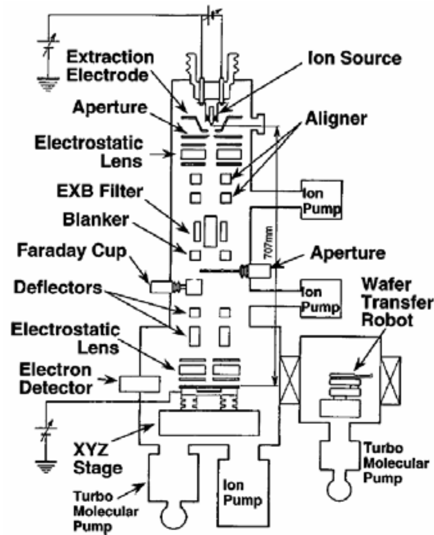

Figure 3.8: Systematic representation of optical setup by Nagamachi *et al.* (figure from [68]).

The low energy focused ion beam used by Nagamachi and coworkers [68] is shown in fig. 3.8. A $Nb_{10}Au_{50}Cu_{40}$ alloy ion source was used in conjunction with an $\mathbf{E}\times\mathbf{B}$ mass filter (mass resolution $\Delta m/m = 1/60$) for use in direct deposition for the fabrication of superconducting devices. Details on the optical system were published in [69, 70]. The initial acceleration potential was 20 kV for single charged ions. Two Einzel lenses were used to focus the beam and retarding was again accomplished by setting the target on high potential. Calculations predicted a beam diameter of approximately 100 nm at 100 eV landing energy and 80 nm at 3 keV, respectively for a beam current of 100 pA (assumed source data: ΔE = 10 eV, J_Ω=20 μA/sr, d_v = 50 nm). The beam diameters in the energy range below 100 eV were calculated to be 1.6 to 1.9 times bigger than those at 20 keV energy. Direct scanning ion imaging was only possible in high energy (nondecelerated) mode using a secondary electron detector. Hence, the probe size in FFLV-R mode was estimated by observation of direct deposited patterns. The authors quite justly note that the thus measured data may be somewhat distorted by the influence of mechanical vibration, ripple on deflector potentials, and spread of the deposited pattern caused by ion migration after deposition. The probe diameter of a decelerated Au beam was reported to vary between 0.5 μm and 8 μm in the current range from 40 pA to 10 nA but unfortunately the energy used for these experiments was not clearly specified. Most probably the energy was of the order of 50 eV and hence the measured values were 5-10 times larger than those predicted. In a further publication [71] the discrepancy between measured and calculated data was attributed to false assumptions on the source characteristics. It was found that by assuming a virtual source size

of 130 nm, an energy spread of 30 eV, and an angular intensity of 10 μA/sr for the Au LMIS the measured probe sizes and beam currents could be reproduced fairly accurately. While the angular intensity was experimentally obtained, the adjustment of the virtual source size and energy spread was justified by the lack of data for the type of source used and the doubtful transferability of data obtained from gallium LMIS.

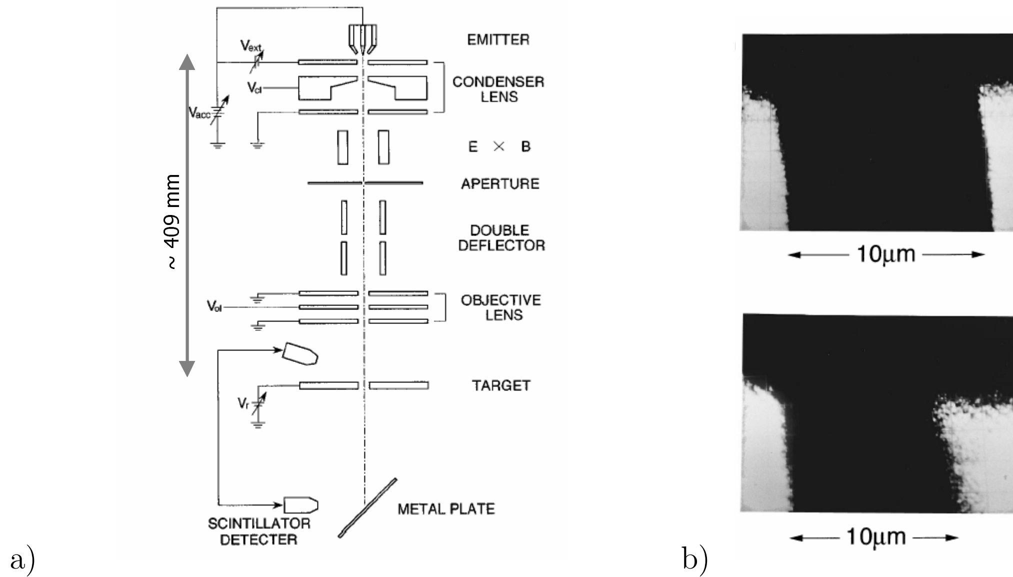

Figure 3.9: a) Schematic drawing of the optical column designed by Yanagisawa *et al.* b) SE images of a nickel grid induced by transmitted gallium ions (ϕ_{accel} = 25 kV, I_{beam} = 100 pA) for ϕ_{target} = 25 kV (top) ϕ_{target} = 100 V (bottom) (figures from [72]).

A similar system was presented in 1995 by Yanagisawa [72, 73] that was used in combination with an MBE system for fabricating 3-dimensional buried semiconductor structures [74–76]. A schematic drawing of the column setup is shown in fig. 3.9a). Two Einzel lenses were used for focusing and an E×B filter allowed the use of alloy LMIS for multi-element doping. The initial acceleration energy was chosen to be 25 keV. Calculations predicted a beam diameter of 100 nm at 100 eV landing energy (60 pA beam current) and approximately 80 nm diameter at 1 keV (100 pA beam current) (assumed source data: ΔE = 10 eV, J_Ω=20 μA/sr, no data on d_v). From Monte-Carlo simulations [28] (see section 5.2) the influence of Coulomb interactions were found to be practically negligible. Image acquisition/probe size measurement was accomplished by using a common SE detector above the target in standard high energy operation. In FFLV-R mode secondary electrons generated by ions impinging on a metal plate after being transmitted through a suitable nickel target mesh were detected again using a scintillator-photomultiplier combination. Resolution experiments were carried

out using a gallium LMIS. From SE images (see fig. 3.9b)) the probe size was estimated to be about 0.5 μm for the landing energy range of 100 eV-15 keV at a beam current of 100 pA. These values were 5-8 times larger than the predicted data and discrepancies were attributed to wrong assumptions of source/system parameters.

Part II

Numerical Simulation

Chapter 4

Aberration-Optical Treatment

The design of a scanning ion microscope (or indeed any charged particle instrument) involves the determination of the field distribution of a particular set of optical elements, e.g. electrostatic lenses and deflection elements. Following the computation of the first-order optical properties such as magnification and focal length, the relevant aberration coefficients and resulting aberration discs are determined. The overall probe size is then calculated according to some suitable algorithm. In optimisation, these steps are repeated for a number of optical elements or system geometries. This process, which may be summarised as aberration-optical treatment of a system, is the main focus of this chapter.

After some introductory remarks on the theoretical background and basic methodic issues, the individual components of the low energy focused ion beam system will be discussed. Short sections are dedicated to system and lens optimisation and the chapter concludes with a summary of the findings of the aberration-optical study and a compilation of the thus expected system performance.

4.1 Fundamentals of the aberration approach

In the case of a rotationally symmetric - with respect to the optical axis in z-direction - electrostatic lens, the overall potential $\varphi(x, y, z)$ may be approximated by a series expansion over the electrostatic potential $\phi(z)$ along the z-axis:

$$\varphi(x, y, z) = \varphi(\theta, r, z) = \varphi(r, z) = \phi(z) - \frac{r^2}{4}\phi''(z) + O(r^4) \tag{4.1}$$

With this series expansion the general non-relativistic equation of motion of an ion with charge q and mass m in the electrostatic lens field $m\dot{\mathbf{v}} = -q\nabla\varphi$ in paraxial approximation reduces to

$$r''(z) + \frac{1}{2}\frac{\phi'(z)}{\phi(z)}r'(z) + \frac{1}{4}\frac{\phi''(z)}{\phi(z)}r(z) = 0 \tag{4.2}$$

Generally any solution $r(z)$ of this linear, homogeneous, second order differential equation may be expressed as a linear combination of two basic solutions r_α and r_γ - also termed fundamental rays - i.e.

$$r = \alpha r_\alpha + \gamma r_\gamma \tag{4.3}$$

Commonly these fundamental rays are defined in the object plane at z_o by choosing

$$r_\alpha(z_o) = 0, \quad r'_\alpha(z_o) = 1, \quad r_\gamma(z_o) = 1, \quad r'_\gamma(z_o) = 0 \tag{4.4}$$

From the evaluation of the fundamental rays at the image plane located at z_i the lens' main optical characteristics such as the image-side focal length f_i, the angular magnification M_α, and the lateral magnification M may then be determined:

$$f_i = -1/r'_\gamma(z_i), \quad M_\alpha = r'_\alpha(z_i), \quad M = r_\gamma(z_i) \tag{4.5}$$

The object-side focal length f_o follows from

$$f_i/f_o = \sqrt{\phi_i/\phi_o} \tag{4.6}$$

where ϕ_i and ϕ_o denote the image and object-side potentials, respectively.
In order to determine the probe size of the ion beam, the lens aberrations have to be calculated. In scanning electron or ion microscopy usually only the first order chromatic and third order spherical aberration are taken into account. The corresponding (object-side) coefficients are found from basic integration:

$$\begin{aligned} C_{s,o} &= \frac{1}{16}\frac{1}{\phi_o^{1/2}}\int_{z_o}^{z_i}\frac{r_\alpha^4}{\phi^{3/2}}\left(\frac{5}{4}\phi''^2 + \frac{5}{24}\frac{\phi'^4}{\phi^2} + \frac{14}{3}\frac{\phi'^3}{\phi}\frac{r'_\alpha}{r_\alpha} - \frac{3}{2}\frac{\phi'^2 r'^2_\alpha}{r_\alpha^2}\right)dz \\ C_{c,o} &= \frac{3}{8}\phi_o^{1/2}\int_{z_o}^{z_i}\frac{\phi'^2}{\phi^{5/2}}r_\alpha^2 dz \end{aligned} \tag{4.7}$$

The image-side aberration coefficients again follow from basic calculus according to

$$C_{c,i} = C_{c,o}M^2\left(\frac{\phi_i}{\phi_o}\right)^{3/2}, \quad C_{s,i} = C_{s,o}M^4\left(\frac{\phi_i}{\phi_o}\right)^{3/2} \tag{4.8}$$

4.2 Method

4.2.1 Quantification of the probe size

Traditionally, the overall ion probe size d is calculated by quadratic superposition of the individual contributions, i.e.

$$d = \sqrt{d_{\text{geo}}^2 + d_s^2 + d_c^2} \tag{4.9}$$

The current contained in the thus determined probe is assumed to equal the total beam current:

$$I = J_\Omega \pi \alpha_o^2 \tag{4.10}$$

with J_Ω and α_o denoting the source angular current density and object-side aperture angle, respectively.

The geometric contribution d_{geo} is given by

$$d_{\text{geo}} = M d_{\text{v}} \tag{4.11}$$

where M denotes the overall system magnification and d_{v} is the diameter of the virtual source. For the most common case of a two-lens ion beam system the total spherical aberration disc d_s is calculated from the contributions $d_{\text{s},1}$ and $d_{\text{s},2}$ of the first (gun) and second (objective) lens, respectively, according to

$$\begin{aligned} d_s &= d_{\text{s}}^{(1)} + d_{\text{s}}^{(2)} \\ d_{\text{s}}^{(1)} &= 0.5\, M C_{\text{s},o}^{(1)} \alpha_o^3 \\ d_{\text{s}}^{(2)} &= 0.5\, C_{\text{s},i}^{(2)} \alpha_i^3 \end{aligned} \tag{4.12}$$

Note that the image-side aperture angle α_i is related to the object-side aperture angle α_o via $M_\alpha = \alpha_i/\alpha_o$.

Similarly the following equations hold in the case of the total chromatic aberration disc d_c:

$$\begin{aligned} d_c &= d_{\text{c}}^{(1)} + d_{\text{c}}^{(2)} \\ d_{\text{c}}^{(1)} &= M C_{\text{c},o}^{(1)} \alpha_o \Delta\phi/\phi_{\text{extr}} \\ d_{\text{c}}^{(2)} &= C_{\text{c},i}^{(2)} \alpha_i \Delta\phi/\phi_{\text{target}} \end{aligned} \tag{4.13}$$

Due to the relatively large energy width $\Delta E = e\Delta\phi$ of gallium ion sources of approximately 5 eV, the chromatic aberration contribution is dominant over a wide beam current range (cf. fig.4.1). Note that unless otherwise stated, an energy width of 10 eV has been assumed in the aberration-optical calculations below. This was done in an attempt to obtain a worst-case estimate of the resulting probe sizes for want of a method to include Coulomb interactions in the analysis. However, as will become evident from the results presented in chapter 5 (which have been obtained using a more realistic energy width of 5 eV), this simple estimate is insufficient to account for the actual infuence of ion-ion interactions on the system performance.

An alternative method for calculating the overall probe size is the so-called *Root-Power-Sum* (RPS) algorithm introduced by Barth and Kruit [77] on the basis of exact wave-optical calculations for high energy beams. The individual contributions to the probe size are chosen to contain 50% of the total beam current as calculated in equation (4.10). The geometric as well as the chromatic

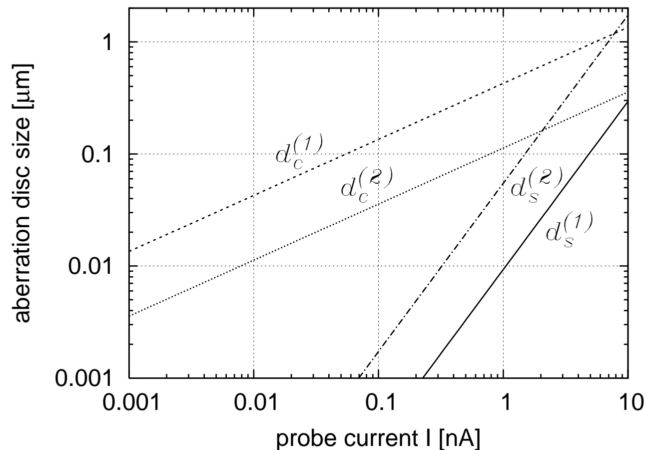

Figure 4.1: Probe size contributions for the system designed by Gnauck [1]. Source distance $z_o = 2$ mm, working distance $wd = 20$ mm, source angular intensity 10 μA/sr, extraction potential $\phi_{\mathrm{extr}} = 3.5$ kV, energy width $\Delta E = 5$ eV.

contribution are evaluated in the Gaussian image plane, whereas the spherical aberration is evaluated in the plane of minimum confusion:

$$\begin{aligned} d_{\mathrm{s,RPS}} &= 0.18\, C_{\mathrm{s}} \alpha^3 \\ d_{\mathrm{c,RPS}} &= 0.34\, C_{\mathrm{c}} \alpha \Delta\phi/\phi \end{aligned} \tag{4.14}$$

where C_{s} and C_{c} may either denote image or object side aberration coefficients. For an ion probe the resulting probe size is then calculated according to:

$$d_{\mathrm{RPS}} = \sqrt{\left(d_{\mathrm{geo}}^{1.3} + d_{\mathrm{s,RPS}}^{1.3}\right)^{2/1.3} + d_{\mathrm{c,RPS}}^2} \tag{4.15}$$

The RPS algorithm typically gives smaller probe sizes than the simple quadratic superposition and some experimental evidence [78, 79] suggests that it yields a better approximation to measured values. Note however, that the resulting probe current density in many cases does not differ significantly for the two calculation approaches as the probe current in the case of the RPS algorithm is only 50% of the total beam current.

As the RPS algorithm has been developed on the basis of wave-optical calculations for high energy (several tens of keV) particle beams its applicability to low energy beams is yet to be discussed. Despite this open issue, the RPS algorithm will nevertheless be used throughout this study for probe size calculations. The main reason for this choice is the simple transferability of the probe size definition (i.e. the disc containing 50% of the total beam current) to the data obtained from direct ray-tracing using the Image software package. Hence the results obtained with different calculation approaches (aberration-based or based on Monte-Carlo simulation/direct ray-tracing) may be quantified based on the

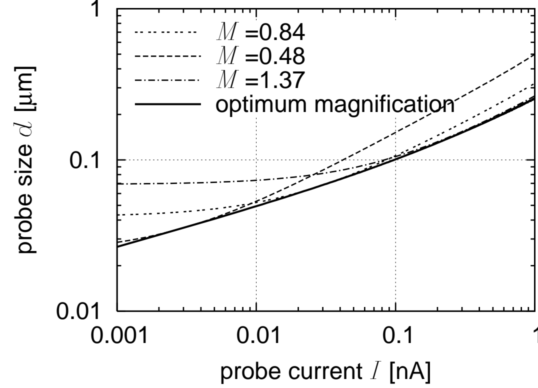

Figure 4.2: Optimum $I-d$ curve (solid line) showing the smallest possible probe size for a given beam current obtained by adjusting the overall system magnification M. The optimum curve is the envelope to corresponding data for fixed magnification as exemplarily shown for three different values of M.

same criterion. Additionally, also the simple quadratic superposition of aberration discs has no physical justification as the individual probe size contributions cannot be generally considered to be statistically independent.

4.2.2 System optimisation

Once a choice on the basic system setup, i.e. the geometry of lenses as well as the overall system geometry, has been made, the question of optimum performance may be addressed. The latter is usually characterised by a minimum probe size d vs. beam current I relation. For a specific beam current value (and hence source aperture angle calculated according to equation (4.10)), the overall system magnification (i.e. the ray-path in the intermediate lens space) is adjusted in such a way that the overall probe size becomes minimal. Mathematically we have

$$\frac{\partial d}{\partial M} = 0 \tag{4.16}$$

Figure 4.2 shows an optimum $I-d$ curve for a typical two-lens focused ion beam system operated at 3 keV energy as the envelope to the corresponding curves calculated with a fixed value of the system magnification. Note that only ray-paths without crossover (non-crossover mode) have been considered for which $M < 0$, as it can be shown [80] that these always yield smaller probe sizes than the corresponding crossover modes.

It should be noted that for most standard scanning electron microscopes only the aberration contribution of the objective lens has to be considered in the calculation of the overall probe size. In this case an optimised system performance is typically characterised by approximately balanced geometrical and aberration contributions.

In standard high energy focused ion beam systems the influence of the gun lens can usually not be neglected (except in the case of very low beam currents) and consequently the characterisation of optimum system performance tends to be more complicated. This is even more the case for focused ion beam systems operated at low energy. Following from equations (4.12) and (4.13) the influence of the gun lens on the chromatic and spherical aberration discs is determined by the overall system magnification M. Based on Liouville's theorem the latter can be expressed as

$$M = \frac{\alpha_o}{\alpha_i}\sqrt{\frac{\phi_o}{\phi_i}} = \frac{1}{M_\alpha}\sqrt{\frac{\phi_o}{\phi_i}} \tag{4.17}$$

As a result of this, for a given fraction of the aperture angles, i.e. angular magnification, the system's lateral magnification and hence the total influence of the gun lens aberrations is always larger for a low energy system compared to a high energy system.

Several authors have addressed the task of finding the optimum system performance based on (semi-)analytical calculus (e.g. [81–83]). A very comprehensive study was carried out by Wang [80]. His approach is based on the thin-lens approximation for the determination of aberration coefficients and the probe size calculation according to equation (4.9). Numerically calculated aberration coefficients for the gun and objective lens for infinite and zero magnification were used as input parameters. However, according to our own calculations, the thus found optimum $I - d$ relation tends to only yield sufficient accuracy in the case of an almost telecentric ray-path.

Consequently, the approach chosen in this study is the exact numerical calculation of the $I - d$ relation that initially involves the determination of the total chromatic and spherical aberration coefficients for all (in practice: for a discrete number) of possible system magnifications. Subsequently, the resulting probe sizes are calculated for a specific value of the beam current, i.e. a specific source aperture angle, and the minimum is determined. This process is then repeated for further values of the beam current and can easily be automated. Depending on the number of individual system magnifications considered, the beam current range of interest, and clearly also on computer speed, the computation of an optimum $I - d$ relation usually can be accomplished within several minutes.

4.2.3 Software

Two different software packages were employed in the aberration-optical analysis. Initially the proprietary set of programs Electron Optical Systems (EOS) by E. Kasper was used. The boundaries of any optical element have to be rotationally symmetric with respect to the optical axis but the boundary values may vary with the azimuth angle. Hence also multipole elements such as deflectors or stigmators can be treated. Field calculation itself is based on the

so-called charged surface method (CSM) (see [84, 85]) in which the electrodes are replaced by a number of circular apertures and charged rings (located inside the electrode). The potential in space of the latter components is available in analytical form and their position and substitute charge is chosen in such a way that the electrode surface carries the required constant potential. A ray-tracing program [86] allows the solution of the ray equation in its paraxial form according to equation (4.2) as well as the inclusion of non-linear terms that yield an (geometrically) aberrated ray. Hence by simulating an ensemble of rays using the latter exact ray-tracing the geometrical aberration disc may be determined. Additionally, the chromatic and spherical aberration coefficients are computed and an auto-focusing algorithm is also implemented.

The commercial program package Optics by MEBS Ltd. [64] relies on the finite-element method (FEM) [85, 87–89] for calculating the field of rotationally symmetric lenses as well as deflectors with a fourfold (geometric) symmetry in the plane perpendicular to the optical axis. The method involves minimisation of a functional of the form

$$F = \int_{\text{Volume}} \frac{\epsilon}{2} (\nabla\varphi)^2 dv \tag{4.18}$$

subject to given boundary conditions (ϵ is the permittivity). The area to be analysed is subdivided into a mesh of triangular finite elements and the potential is assumed to be a linear function of position in the case of the first-order FEM or a bi-quadratic function of position in the case of second-order FEM. The variation of the functional then yields a set of simultaneous algebraic equations which interrelate neighbouring mesh-points. The first-order optical properties are determined by numerically solving the paraxial ray equation and the third-order geometric and first-order chromatic aberration coefficients are computed by evaluating the appropriate aberration integrals (e.g. using equations 4.7).

As could be expected both packages yield virtually identical results both with respect to field computation as well as to the calculation of first and third-order optical characteristics. Initially, the EOS software was used almost exclusively as the comparatively simple generation of lens geometries for field calculation makes it particularly valuable for use in automated lens optimisation. On the other hand, Optics offers the clear advantage of compatibility to other programs by MEBS Ltd. which are required for further or advanced analysis. For example, the program package Image (see chapter 5) relies on electrostatic potentials computed by the second-order FEM.

4.3 Results

4.3.1 Gun lens

General design. In order to allow an independent choice on focusing condition and beam energy, at least a three electrode gun lens is required. The energy of the ions entering the lens is set by the first electrode while the last electrode determines the ion energy in the drift space between gun and objective lens. An additional electrode is used for focusing, i.e. adjusting the beam path and hence the overall system magnification. An investigation on the optical characteristics of different possible lens designs was carried out by Mayer [52] and the design by Seeliger [90] (later also studied in detail by Orloff and Swanson [91]) proved to be particularly suitable. However, in previous applications of this type of lens [1, 38, 52], the first electrode typically served as extractor electrode with a reduced bore diameter for increasing the extraction field strength. Due to the required increased source distance for the current system (see paragraph on internal focusing mode below) an additional extractor electrode has to be used (see fig. 4.3). Note however, that in order to simplify the setup and operation of the lens, extractor and first gun lens electrode are kept on the same potential.

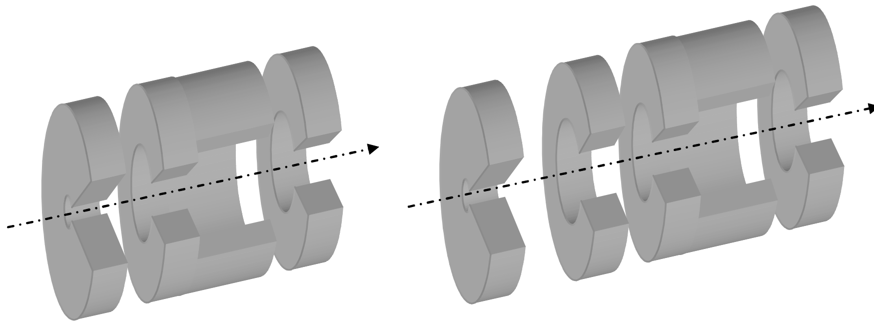

Figure 4.3: Gun lens design. Left: design used by Mayer [52] and Gnauck [1] with the first lens electrode serving as extractor. Right: modified design with separate extractor electrode. The arrow indicates the optical axis.

In the following calculations, the actual acceleration field between the emitter tip and the extractor electrode is substituted by a field-free half space assumed to be on potential ϕ_{extr}. This separation of emitter and lens domains alleviates the calculations significantly, in particular as no quantitative data on the details of the gallium emitter geometry (i.e. the so-called Taylor cone, see e.g. [92]) is available. The ions are assumed to originate at the position of the virtual source. A theoretical justification for this approach is given in [84, 93].

Immersion operation. The overall action of the gun lens in a two-lens focused ion beam system is to accelerate the ions from the extraction energy $q\phi_{\text{extr}}$ to the

drift space (liner tube) energy $q\phi_{\rm lt}$. For the vast majority of ion beam systems the latter also equals the landing energy, i.e. the objective lens is operated as an einzel lens (see discussion below). For a given geometry, the gun lens may be characterised using the immersion ratio

$$\kappa_1 = \phi_{\rm lt}/\phi_{\rm extr} \tag{4.19}$$

For a standard high energy focused ion beam system $\kappa_1 \approx 30/7$. With increasing immersion ratio the effective optical lens (determined by the position of the principal planes) is shifted further towards the low energy side of the physical lens. Figure 4.4a) depicts this exemplarily, showing the position of the principal planes for a typical gun lens operated in einzel and immersion mode. Finally, as a consequence of the reduced object (source) side focal length the object side aberration coefficients tend also to be reduced. However, as shown in fig. 4.4b), the reduction is running into saturation for high immersion ratios as the lens action is increasingly dominated by the immersion field alone.

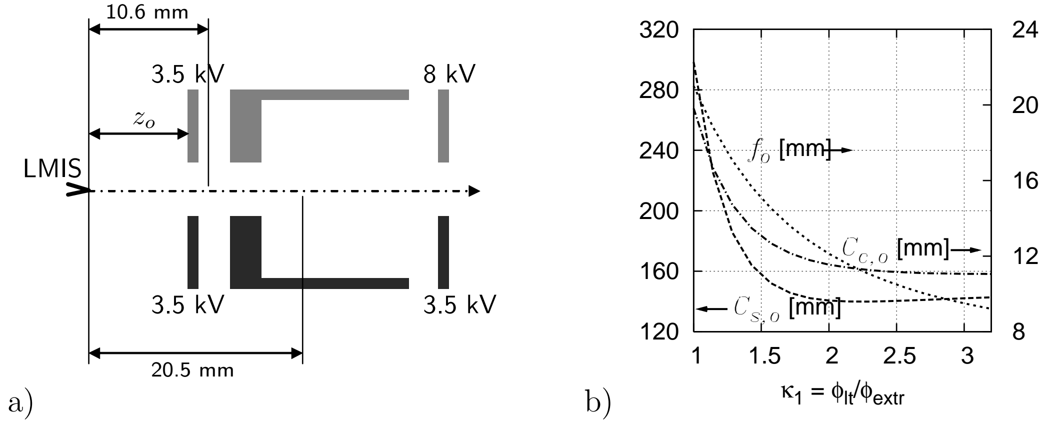

Figure 4.4: a) Position of object-side principal planes for the gun lens in einzel mode operation (lower part, $\phi_{\rm extr} = \phi_{\rm lt} = 3.5$ kV) and immersion mode operation (upper part, $\phi_{\rm extr} = 3.5$ kV, $\phi_{\rm lt}= 8$ kV). The source is assumed to be situated 9 mm in front of the first lens electrode. b) Influence of immersion ratio on object-side chromatic and spherical aberration coefficients $C_{c,o}$ and $C_{s,o}$ (infinite magnification), respectively, and object-side focal length for the gun lens. Source distance $z_o = 9$ mm.

Internal focusing mode. Generally focusing of a charged particle beam using an electrostatic lens may be achieved by two different values of the focusing voltage. In most cases, with one of these the beam energy inside the lens is higher than outside (acceleration or accel mode operation), whereas with the other the beam energy is lower inside the lens than outside (deceleration or decel mode operation). Usually, the lens optical data in terms of aberration coefficients are superior in the case of accel mode operation. However, this gain in performance

is clearly associated with a higher technical effort regarding power supplies and insulation requirements. In order to enable accel mode operation for the gun lens with respect to practicable voltage levels, the source distance z_o has to be increased. Following the above reasoning this inevitably leads to a deterioration of aberration properties and thus somewhat antagonises the benefits of immersion operation. Consequently, a trade-off has to be found. Figure 4.5 shows the optical parameters (infinite magnification) of the gun lens operated in accel mode as a function of the source distance for extraction potentials of 3.5 kV and 4.5 kV, respectively. The final gun lens electrode is kept at $\phi_{\text{lt}} = 8$ kV. The value of 3.5 kV corresponds to the initial assumption for the extraction potential [1], whereas the value of 4.5 kV is closer to the experimental reality. As expected with the higher entrance energy, the focusing voltage values are also increased. From fig. 4.5 a source distance of about 8-10 mm seems reasonable, avoiding both the steep increase in focusing potential for smaller values of z_0 as well as the increase in aberration coefficients for larger z_0, respectively.

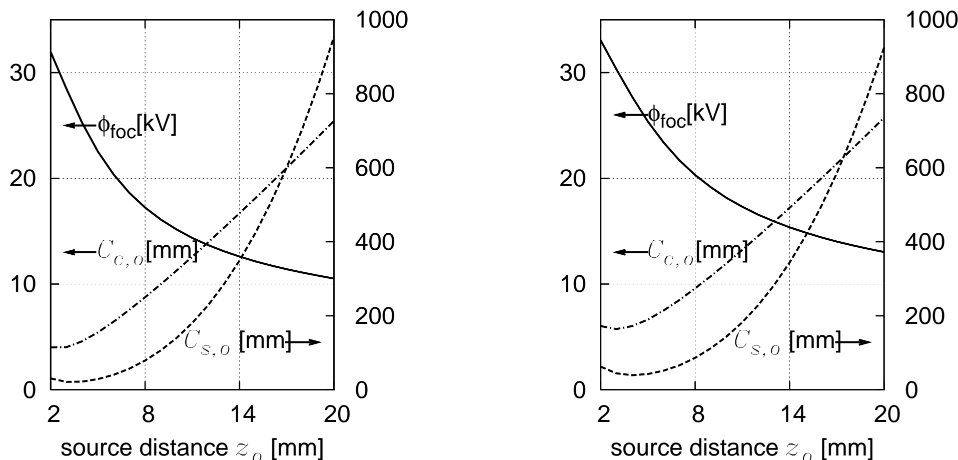

Figure 4.5: Gun lens parameters (infinite magnification) as a function of the source distance z_o for an extraction potential of 3.5 kV (left) and 4.5 kV (right), respectively. Focusing potential ϕ_{foc} and object-side chromatic and spherical aberration coefficients $C_{c,o}$ and $C_{s,o}$, respectively.

4.3.2 Objective lens

General design. Due to the originally intended application of the focused ion beam system as an add-on to a scanning electron microscope with a Gemini-type objective lens, the design of the FIB objective lens was somewhat constrained. With the tapered Gemini lens and the position of the adapter flange for the ion beam column, a minimum working distance (distance from final lens electrode to target) is achieved by choosing a tapered design for the FIB objective lens.

Again starting from the design by Seeliger, the geometry was altered accordingly. Assuming pre-lens or in-lens scanning (see following section) thus a working distance of 15 mm is possible, whereas with post-lens scanning the minimum working distance is about 28 mm. Figure 4.6 shows a sketch of the original and modified lens design, together with the relevant optical data for zero magnification at a working distance of 15 mm (accel mode focusing).

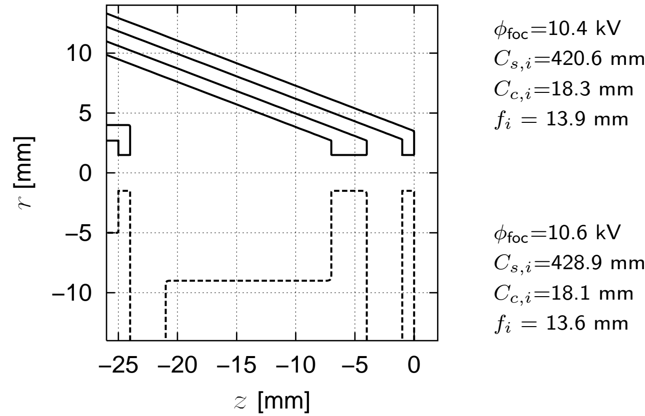

Figure 4.6: Objective lens design and relevant optical data for a final beam energy of 3 keV and 15 mm working distance (accel mode focusing, zero magnification, ϕ_{lt} = 8 kV). Focusing potential ϕ_{foc}, image-side chromatic and spherical aberration coeficients $C_{c,i}$ and $C_{s,i}$, respectively, and image side focal length f_i. The original design is shown in the lower part of the figure whereas the upper part shows the modified design.

Immersion and accel mode operation. With the design and consequently the optical data being similar, the previously discussed findings for the gun lens concerning immersion and accel mode operation also apply to the objective lens. However, clearly the source distance z_o has to be substituted by the working distance wd and the immersion ratio for the objective lens must be used:

$$\kappa_2 = \phi_{\mathrm{lt}}/\phi_{\mathrm{target}} \tag{4.20}$$

It should be noted that due to the overall decelerating action of the objective lens, the immersion ratio is a main factor determining the maximum possible working distance. For a given immersion ratio the latter is also critically dependent on the choice of the focusing mode (see fig. 4.7). Hence in order to realise very low landing energies for a certain working distance (often dictated by the application) the liner tube potential may have to be lowered.

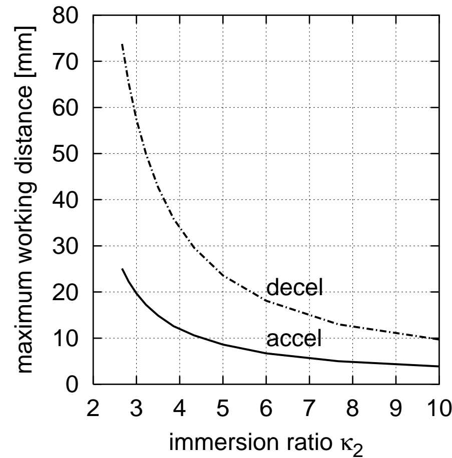

Figure 4.7: Maximum working distance as a function of the immersion ratio κ_2 (objective lens operated at zero magnification, $\phi_{\mathrm{lt}} = 8$ kV).

4.3.3 In-lens scanning

As discussed previously a small working distance is clearly advantageous in order to keep aberrations and hence the overall probe size small. In a typical high energy focused ion beam system the liner tube is grounded and any deflection elements are hence operated with respect to ground potential. Dynamic beam scanning for image acquisition may thus be realised by using a double stage deflection arrangement upstream of the objective lens without compromising the working distance. However, with the intermediate lens space set on high potential the implementation of such a deflection system may be more difficult. Apart from problems associated with electronic control and supply at fast pixel rates there is still the task of mechanical setup of an (ideally) eight-fold split and insulated liner tube. Obviously, the use of a single stage post-lens deflector downstream of the objective lens circumvents some of these problems although clearly at the cost of an increased working distance. Alternatively, a single stage in-lens deflector employing a split final objective lens electrode may be used. With this arrangement the deflector is operated with respect to ground (as in the case of post-lens deflection) while not affecting the working distance. Furthermore the deflection sensitivity is higher than in the pre-lens deflection arrangement (assuming FFLV-R mode operation) as the beam is retarded to the final landing energy within the last electrode. Figure 4.8 shows the increase in probe size vs. field size relative to the on-axis beam diameter for the in-lens deflection as well as for a simple post-lens deflection system assuming a working distance of 15 mm. The on-axis beam diameter is 100 nm in both cases. Obviously, for the particular lens and deflector design, the in-lens deflection system even outperforms the post-lens deflection arrangement. Additionally, given the geometrical constraints due to the SEM objective lens discussed above, a more realistic working distance

for the post-lens deflection arrangement would be 28 mm with a corresponding further increase in on-axis probe size.

For the arrangements discussed here the total probe size is dominated by the transverse chromatic aberration contribution for field sizes (field size = full side length of deflection field) up to about 1 mm. Note that although the increase in probe size for both arrangements is quite pronounced, it is still acceptable for imaging purposes.

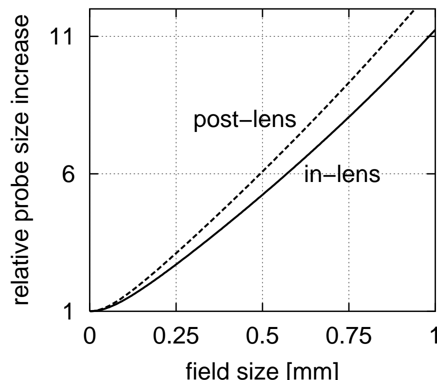

Figure 4.8: Relative increase in probe size vs. scanning field size for two different deflector arrangements. Working distance (from final lens electrode) 15 mm, on-axis probe diameter 100 nm. The distance from the lower deflector boundary to the target is 9 mm for the post-lens arrangement (deflector length 5 mm). Note that image distortion has already been corrected.

4.3.4 Lens optimisation

In order to round off this section, some remarks on lens optimisation are required. Indeed, a considerable amount of time was spent on more general investigations on the optimisation of a low voltage FIB system during an early phase of this study. The system setup of Mayer [52] was chosen as a starting point and the optimisation goal initially was to achieve the highest possible probe current density, i.e. the smallest possible probe size, at a total beam current of 1 nA at a beam landing energy of 1 keV. The system was assumed to be operated in FFLV-R mode with a liner tube voltage of V_{booster} = -5 kV, i.e. ϕ_{lt} = 6 kV, but with decel mode operation of the individual lenses. The source and working distances were taken to be 2 mm and 25 mm, respectively. From an analysis of the probe size contributions similar to fig. 4.1 it was found that the chromatic aberration disc of the gun lens was by far dominating the overall probe size for the current range of interest (assuming a telecentric ray path in the drift space). Hence the influence of a change in geometry of the first lens was investigated. Of the ten geometry parameters of the lens design shown in fig. 4.3 that may be varied independently

(4 bore diameters, 4 bore lengths, and 2 electrode distances) only the bore length and bore diameter of the first lens electrode were kept constant as the latter also served as extractor electrode. The other geometry parameters were varied in turn and only one at a time with the constraint that the design ought to be technically realisable. Also designs including high aspect ratios (i.e. bore length divided by bore diameter) were excluded due to potential problems with charging or secondary electron generation. From these simple calculations it soon became apparent that no substantial improvement in the lens data could be achieved by variation of a single geometry parameter. Consequently, the next step was to alter a number of geometry parameters simultaneously. It was found that by scaling the entire gun lens (apart from the first electrode) by a factor of two and subsequently using a minimisation algorithm of the Simplex type, the beam current density could be increased by 70%, i.e. the probe size was reduced from 1.33 μm to 1.04 μm. Additionally, lens optimisation using a genetic algorithm (GA) [94] was investigated. The GA was adapted to the EOS program package for automated execution, but the best lens geometry found was slightly inferior to the just mentioned scaled geometry. This was attributed to problems in the calculation of automatically generated lens geometries but also due to difficulties in automatically considering all practical constraints like bore aspect ratios or minimum electrode distances simultaneously. Although basically, it was felt that these difficulties could be overcome by more elaborate routines controlling the program execution, any further work was put back for the sake of a practical realisation of a laboratory setup. Indeed, by choosing appropriate operation modes for the individual lenses as well as the overall system as outlined in the previous sections, the predicted performance could be sufficiently improved to justify this procedure.

4.3.5 Summary and overall system performance

In the previous sections the design of individual system components has been discussed in some detail on the basis of purely aberration-optical calculations. These calculations served as a guideline to identify the key data for the experimental realisation of the ion beam setup, namely a source distance z_o of 9 mm and a working distance wd of 15 mm. It also became evident that the system performance may be improved by employing a liner tube on high voltage as well as focusing the ion beam in internal acceleration mode. For illustration purposes this envisaged mode of operation is again summarised graphically in fig. 4.9. Following the optimisation procedure outlined above, the expected system performance can now be quantified in terms of a minimum probe size d vs. beam current I graph. Figure 4.10 shows the results for different combinations of operation modes (immersion ratio, focusing mode). Additionally, table 4.1 exemplarily summarizes the potential values for a telecentric ray-path between the lenses. The extraction potential and final beam energy are assumed to be 4.5 kV and 3 keV, respectively. A distance between the lenses of 494 mm was used, which corresponds to the actual value of the experimental setup.

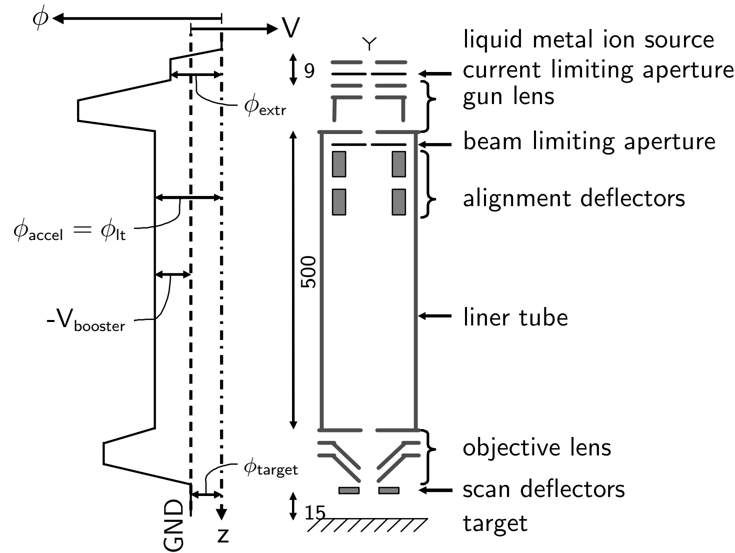

Figure 4.9: Sunmmary of envisaged operation mode showing the schematic course of the kinetic potential ϕ and the ground related potential V (voltage) for the low energy focused ion beam system. For single charged positive ions the relationship $\phi = \phi_{\text{target}} - V$ holds, where $q\phi_{\text{target}}$ is the landing energy at the grounded target. ϕ_{extr} = extraction potential; $\phi_{\text{accel}} = \phi_{\text{lt}} = \phi(\text{liner tube}) = \phi_{\text{target}} - V_{\text{booster}} > \phi_{\text{target}}$. V_{booster} is the negative potential used to “boost” the positive ions to high energy in order to reduce Coulomb interaction effects in the comparatively long liner tube. Distances in mm.

	ϕ_{lt}	$\varphi_{\mathrm{foc,\ gun}}$	$\varphi_{\mathrm{foc,\ objective}}$
mode A	8 kV	19.0 kV	10.3 kV
mode B	3 kV	10.5 kV	7.3 kV
mode C	8 kV	1.7 kV	2.2 kV
mode D	16 kV	22.2 kV	9.9 kV

Table 4.1: Source-related potentials for four different operation modes of the low energy ion optical system (telecentric ray-path between the lenses).

Concluding from this data, a very good system performance may be achieved by using an immersion ratio of $\kappa_2 = 8/3$ (which corresponds nicely to the results displayed in fig. 4.4b)) together with accel mode operation of both gun and objective lens. Further increasing the immersion ratio apparently does not result in a significant improvement in system performance but rather increases demands on technical (insulation) requirements. Consequently, the experimental setup was designed for a maximum liner tube voltage of V_{booster} = -5 kV and accel mode operation of gun and objective lens.

Unfortunately, as we shall see in the following chapter, these findings are somewhat qualified, when Coulomb interactions are taken into account.

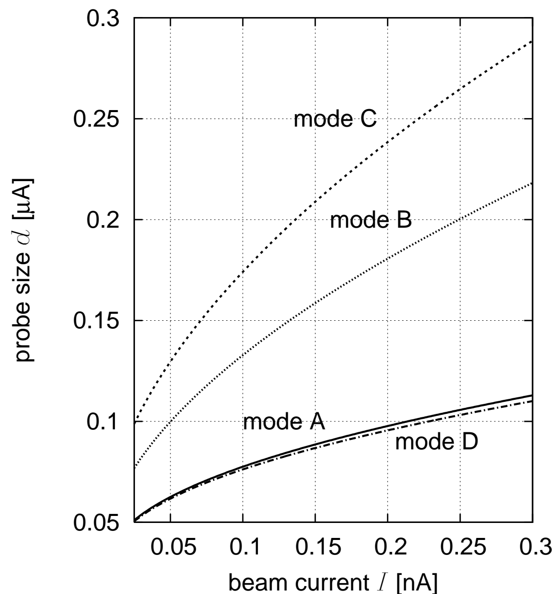

Figure 4.10: Comparison of different operation modes of the low energy ion optical system. Data from aberration-optical calculations. Mode A: accel mode focusing, ϕ_{lt}=8 kV; mode B: accel mode focusing, ϕ_{lt}=3 kV; mode C: decel mode focusing, ϕ_{lt}=8 kV; mode D: accel mode focusing, ϕ_{lt}=16 kV. Landing energy 3 keV.

Chapter 5

Impact of Coulomb Interactions

For any low energy ion beam the impact of mutual Coulomb interactions may be expected to be more significant compared to both, an electron beam of the same energy or an ion beam of higher energy. Yet, apparently no experimental evidence for any interaction influence was observed in previous low energy setups [1, 38]. Furthermore, effectively no directly applicable theoretical investigations on the impact of Coulomb interactions on low energy focused ion beam performance have been published. While qualitatively, the influence of beam energy and current, column length, and focusing mode are intuitively clear, meaningful quantitative data are more difficult to obtain. In this chapter an attempt is thus made to quantify the effects of mutual interactions within the low energy ion beam setup introduced above. While this analysis is naturally specific to the particular setup, the findings are nevertheless felt to provide more general guidelines for low energy FIB design.

Following some general considerations on Coulomb interactions and a brief summary of previous studies focusing on low energy FIB systems, the methods employed in this study are introduced. Subsequently, the predicted effects of mutual interactions on the system performance discussed in the previous chapter are presented.

5.1 Characterisation of Coulomb interactions

An excellent and detailed account on Coulomb interactions has been compiled by Jansen [95] and a somewhat abridged version focusing on beams under non-laminar flow conditions (see below) may be found in [96]. Essentially, three different effects of mutual interactions in a charged particle system may be distinguished. The so-called Boersch effect causes a broadening of the overall energy distribution and hence an increased chromatic aberration contribution. The trajectory displacement (or Loeffler) effect describes the lateral dislocation of the individual beam paths. Both these effects cannot be eliminated as they are of

statistical nature. Only the mean space charge effect that causes a beam defocus (negative lens action) due to the average charge within the particle beam may be compensated by appropriate refocusing of the lenses. The latter is strictly only true under the assumption of a uniform circular particle distribution. For non-uniform distributions, also the aberrations of the space charge lens may have to be considered.

A number of analytical equations have been proposed by several authors [95, 97, 98] to quantify the effects of statistical interaction effects. These expressions may provide a basic idea on how the main system parameters - or rather their variation - will influence the system performance. In the case of a pencil beam under non-laminar flow conditions (i.e. beam currents smaller than approximately 1 nA for a 3 keV gallium ion beam, see [96]) the following equations apply for the trajectory displacement and the Boersch effect, respectively:

$$\delta r \propto \frac{m^{3/2} I^3 L^3}{\phi^{3/2}} \tag{5.1}$$

$$\delta E \propto \frac{m I^2 L}{\phi^2} \tag{5.2}$$

Here m and L denote the particle mass and the length of the considered beam segment. It is important to note that the applicability of any analytical expression is limited by the assumptions underlying the chosen calculation model. For an arbitrary system setup, thus a numerical analysis (considering multiple trajectories and their interactions) is generally required.

5.2 Previous studies on low energy systems

As already indicated above only very little data on the expected effects of Coulomb interactions in low energy focused ion beam setups has been published and the available studies are exclusively dealing with setups operated in VLV mode (see also section 3.3).

Narum and Pease [27] used an extension of Monte-Carlo techniques earlier introduced by Yau *et al.* [58] to model space charge effects in a simple single-lens FIB setup. The initial beam energy and overall system length were taken to be 50 keV and 10 cm, respectively. The ions were assumed to be isotropically emitted from a disc of 30 nm into a cone with a 2 mrad semiangle ignoring both the acceleration field in the source region as well as the inherent energy spread of the LMIS. The lens was considered to be free of spherical aberration and the influence of the chromatic aberration was negligible due to the assumptions on the source. It was found that the observed beam broadening was mainly due to stochastic Coulomb interactions. The beam diameter was calculated from numerically modelling the (ideal) measurement of the edge spread function, and the results are displayed in fig. 5.1. As expected, in VLV mode the impact of

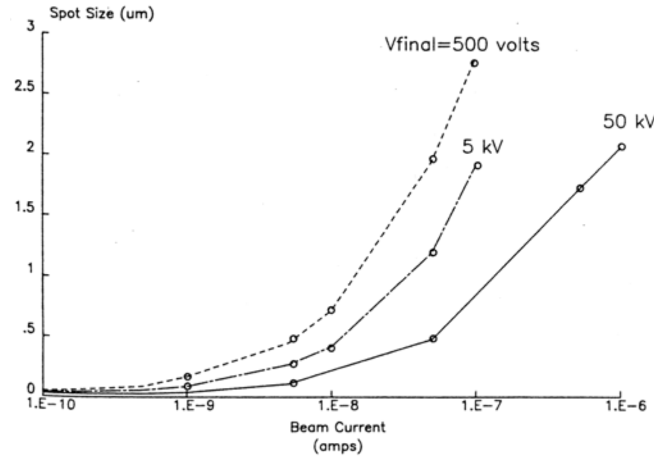

Figure 5.1: Results of the simulation of Coulomb interactions performed by Narum and Pease for different values of the target kinetic potential. The initial beam energy is 50 keV. Figure taken from [27].

mutual ion interactions was found to be significantly larger compared to standard high energy operation due to the increased interaction time. However, the overall beam broadening due to Coulomb effects only became significant for beam currents of 10 nA and higher.

Hirohata *et al.* [28] also used Monte-Carlo methods for calculating Coulomb effects but were also able to include (thin) lens aberrations in their analysis. Although the setup by Yanagisawa *et al.* [72] was chosen as a model system (cf. fig. 5.2a)), the study appears to be the result of a cooperation of several Japanese research groups. The virtual source size and energy width (full width at half maximum) of the LMIS was assumed to be 50 nm and 10 eV, respectively and the initial ion energy was taken to be 25 keV. An unrealistic value of 100-1000 μA/sr was chosen for the angular current density in order to artificially exaggerate Coulomb effects. Initial calculations showed that interactions were predominantly occurring in the retarding field region, i.e. in the region between the objective lens plane and the target and consequently only this region was considered for quantitative analysis. The results are shown in fig. 5.2b) for a angular current density of 100 μA/sr and different values of the final beam energy. The contribution of Coulomb effects to the overall probe size was found to be less than about 10% over the whole investigated current range of 0.1-10 nA.

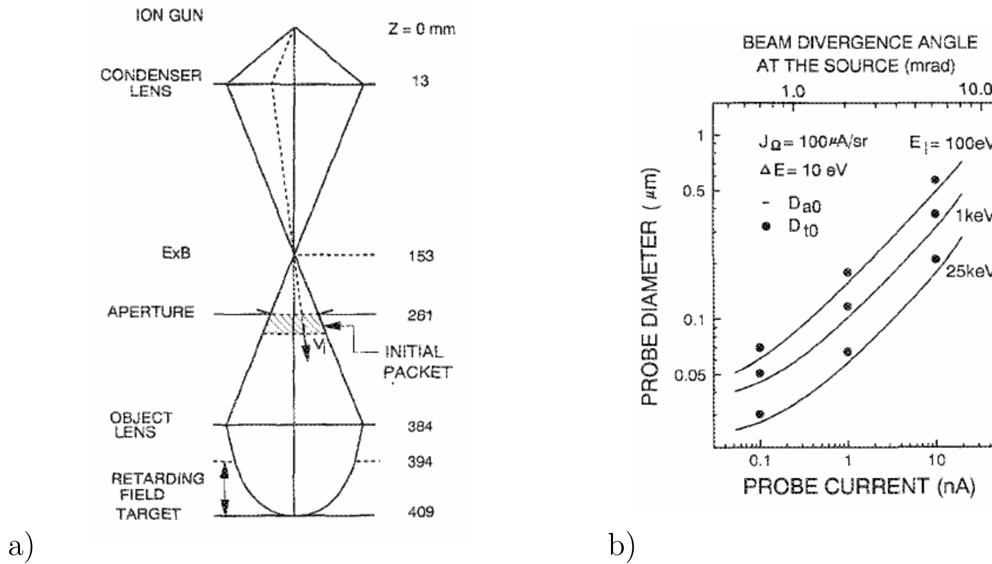

a) b)

Figure 5.2: a) Model system used for the Monte-Carlo simulations by Hirohata *et al.*. b) Results for different landing energies. Lines correspond to aberration-optical calculations whereas the circles show the probe diameters estimated from Monte-Carlo simulation including lens aberrations (figures from [28]).

5.3 Method

5.3.1 Software

For the analysis of Coulomb interaction effects the commercial program package IMAGE by MEBS Ltd. [64] was used which employs direct ray-tracing to simulate the combined effects of lens aberrations and Coulomb interactions.

Lens fields are first calculated using the second order finite element method. The resulting axial field functions are then fitted with a series of Hermite polynomials and the resulting analytic representation may be used to extrapolate the overall potential in space. After chosing suitable lens settings, i.e. electrode potentials in the case of electrostatic lenses, automated focusing of the paraxial ray to a specific image plane can be performed. Particle bunches with randomly generated initial conditions (regarding the angular intensity, lateral beam shape, and energy distribution) are then traced through the system. For each time step in the ray-trace the overall field created by the lens field as well as by surrounding particles is taken into account. The latter corresponds to the Coulomb interaction between the particles and may either be evaluated directly or using a fast tree-code algorithm.

Some considerations are required regarding the appropriate choice of the so-

called sample length Δ given as

$$\Delta = \sqrt{2\frac{q}{m}\phi_{\text{extr}}} N_q \frac{q}{I} \tag{5.3}$$

where N_q is the number of particles in the bunch. The parameter Δ basically represents the length along which the bunch particles are initially distributed for calculation. Generally, particles situated close to the edge of a bunch are excluded from numerical analysis as they only experience reduced interactions. Thus the sample length must be chosen large enough in order to prevent any artefacts arising from this cut-off. Ideally, Δ is of the order of the column length. Note however, that computation time approximately varies with $\log N_q$. For a gallium ion beam with an extraction potential of 4.5 kV, a value of $\Delta/N_q \approx$ 17.8 mm is found at a beam current of 10 pA. The number of particles in the bunch is varied in proportion to the beam current, thus resulting in an increased particle density within Δ. From a practical point of view, the number of particles in the bunch is chosen just large enough so that any further increase does not lead to a significant change in the simulation output. The overall accuracy of the simulation is dependent on the total number of simulated particles $N = N_b \times N_q$, where N_b is the number of bunches. Note that N should be approximately kept constant throughout the simulation in order to get comparable results.

5.3.2 Quantification of the probe size

The IMAGE software package offers the possibility to interactively evaluate the particle distribution in order to quantify a probe diameter. The two-dimensional particle distribution in the chosen image plane (or indeed in any plane parallel to the latter and user-defined by a value Δz) is binned into two one-dimensional distributions as shown in the screenshot of fig. 5.3. From the resulting bell-shaped projections the full width at half maximum (FWHM) is then output. Additionally, by integrating the projected distributions (the mathematical equivalent to the knife-edge-method), the 12%-88% as well as the 20%-80% rise distances are determined and also output. While the FWHM value has shown to be strongly dependent on the particular choice of the number of bins, the integration method appears to be less sensitive on binning parameters. However, as a consequence of mutual interactions, the particle distribution tends to be characterised by rather long beam tails. Thus, the integration method yields unreasonably large values for the probe diameter. Consequently, in default of a more suitable method the FWHM data was initially used for quantifying the probe size [99]. However, in order to obtain a more objective measure for the probe size and to also enable automatic evaluation of the particle distribution data, an improved method has been realised [100] that has already been employed in the context of Coulomb analysis before [95]. After calculating the distance $r_k = \sqrt{x_k^2 + y_k^2}$ (k $= 1 \ldots N$) from the optical axis of each of the N simulated particles at a given image plane,

the distances are sorted in ascending order and the probe size is then defined as $d_{N/2} = 2 \times r_{N/2} = d_{50}$. The probe size obtained in this way clearly corresponds to a probe current of 50% of the beam current and hence the results are equivalent to the RPS probe diameter values used in the aberration-optical calculations (see also discussion in section 4.2.1)

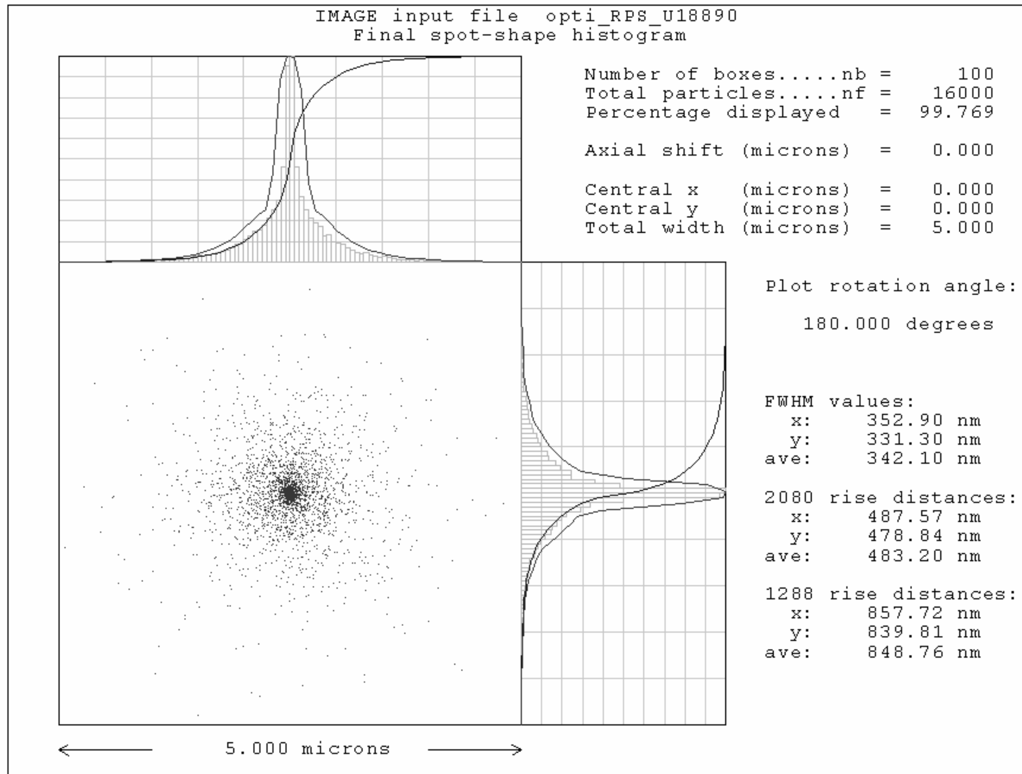

Figure 5.3: Screenshot of the output of the ImageSP program (provided as part of the Image program package) for interactively quantifying the probe size. The particle coordinates are binned in two perpendicular directions.

This method of automated probe size quantification also offers the advantage that the correction of the mean space charge defocus effect may easily be simulated without any user interaction: using the x coordinate of a particle x_k in the image plane as well as the slope of the corresponding trajectory x'_k the position of this particle in an parallel plane with distance Δz is calculated according to

$$\tilde{x}_k = x'_k \times \Delta z + x_k \tag{5.4}$$

After applying the same procedure to the y coordinates of the particle distribution, a new set of particle positions is obtained for which the probe size may then be determined accordingly. Due to the negative lens effect of the mean space charge only defocus values $\Delta z > 0$ have to be considered. From the resulting defocus series (cf. fig. 5.4), the plane of minimum confusion in which the ion probe size takes on its minimum value may easily be found.

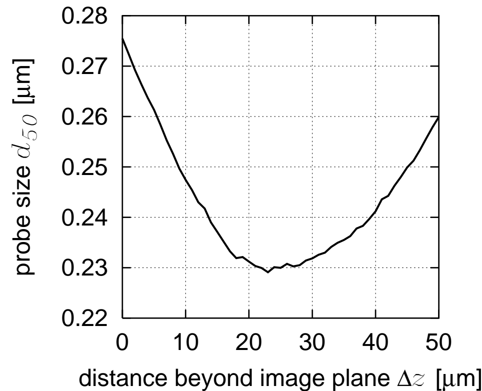

Figure 5.4: Defocus series to determine the plane of least confusion, where the mean space charge effect is minimised. The example shows the results for the ion beam system operated in mode A (see section 4.3.5) at a final beam energy of 3 keV and a total beam current of 120 pA. The value of $\Delta z = 0$ corresponds to the Gaussian image plane.

5.3.3 System optimisation

A simple (but somewhat inaccurate) method to estimate the impact of Coulomb interactions on the system performance as predicted by aberration-optical calculations is to select a number of data points from the optimum $I - d$ graph (described in section 4.2.2) and recalculate the corresponding ray-path using the IMAGE program, i.e. virtually switching on interactions. However, while these ray-paths are clearly distinguished in the case of neglected interactions, this remains no longer true in the presence of interactions. In other words, the minimum probe size for a given beam current is typically obtained at a system magnification different from the one found from aberration-optical calculations. Suppose that for a certain value of the beam current, the latter is denoted by M_{aber}, and the corresponding optimum value in the presence of interactions by M_{Coulomb}. Then the following inequality holds:

$$|M_{\text{aber}}| > |M_{\text{Coulomb}}| \tag{5.5}$$

This means that the optimum mode is shifted to more divergent ray-paths, thus reducing the beam current density within the ion column. However, this explanation does clearly not account for the pronounced increase in probe size when going to strongly divergent ray-paths (cf. fig. 5.5). Here a closer analysis of the beam current density distribution along the optical axis and the relative influence of classical aberration contributions is required.

An alternative but rather qualitative explanation is based on the fact that according to eqns. 4.11 and 5.5, the optimum geometric disc d_{geo} is always smaller in the presence of Coulomb interactions. Rather qualitatively this may be understood by using the analogy of a simple single lens setup without considering

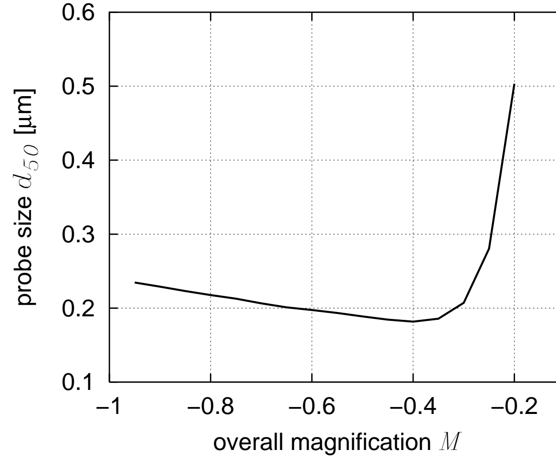

Figure 5.5: Influence of the variation of the system magnification M (< 0 for the non-crossover modes) on the achievable probe size in the presence of Coulomb interactions. The mean space charge effect has been corrected. The data shown corresponds to a final beam energy of 3 keV and a total beam current of 120 pA (mode A operation). The optimum magnification as obtained from aberration-optical calculations is $M_{\text{aber}} = -0.99$.

interactions. An optimsation for the latter is achieved, when the overall aberration disc $d_{\text{aber}} = \sqrt{d_s^2 + d_c^2}$ approximately equals the geometric disc: if $d_{\text{aber}} > d_{\text{geo}}$, the magnification may be increased without loss in resolution but possibly with a gain in probe current. If, on the other hand, $d_{\text{aber}} < d_{\text{geo}}$, the resolution (and hence the system performance) can in principle be improved by reducing the magnification. For a two lens system in which both lenses contribute to the overall aberration disc the explanation is less straight forward and even more so if Coulomb interactions also have to be considered. Nevertheless, in a full optimisation the geometric disc has to be somehow balanced against the sum of the contributions from lens aberrations and Coulomb interactions. Thus as the Coulomb interaction contribution is decreased by altering the ray-path, also the geometric contribution is decreasing. Figure 5.5 exemplarily shows the results of a variation of the overall system magnification using the Image program and the probe quantification routine described in the previous section.

It should be noted, that the just described full optimisation of the system (i.e. finding the optimum magnification value in the presence of interactions) is an extremely time-consuming task due to the required computational effort using the Image program. Consequently, fully optimised data has only been calculated for a limited number of operation modes (see below). Here, an alternative calculation approach as presented in [101] could possibly be beneficially employed.

5.4 Results

5.4.1 Overall system performance including interactions

The operation modes previously discussed on the basis of aberration-optical calculations (cf. section 4.3.5) have again been calculated including the effects of Coulomb interactions - this time however using a more realistic energy width of 5 eV. The corresponding results are summarised in fig. 5.6. Although this data must be considered a worst-case estimate due to non-adjusted system magnification, it certainly provides a suitable basis for a re-assesment of the optimum choice of system parameters such as focusing mode and liner tube voltage.

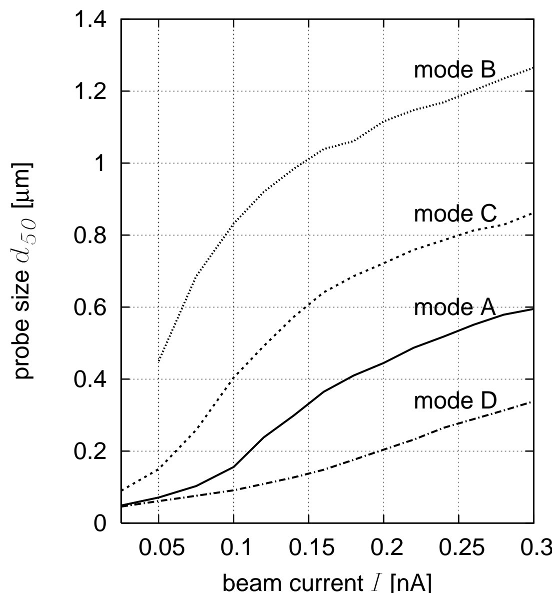

Figure 5.6: Comparison of different operation modes of the low energy ion optical system. Data including Coulomb interactions. Mode A: accel mode focusing, ϕ_{lt}=8 kV; mode B: accel mode focusing, ϕ_{lt}=3 kV; mode C: decel mode focusing, ϕ_{lt}=8 kV; mode D: accel mode focusing, ϕ_{lt}=16 kV. Landing energy 3 keV.

From a mere comparison of the ordinate range of figs. 5.6 and 4.10, respectively, it becomes immediately evident that Coulomb interaction effects indeed have a limiting influence on the predicted system performance. Consequently, the liner tube voltage, i.e. the ion's kinetic potential within the column drift space, is becoming the main factor determining the system quality. This effect is particularly obvious for operation modes B and C, which - qualitatively - have swapped places in fig. 5.6 compared to fig. 4.10. Also, operation mode D now significantly outperforms operation mode A with respect to the achievable minimum probe size.

In order to estimate the effect of interaction time, also the expected system

performance for operation mode A with a reduced drift space length of 350 mm (compared to 494 mm) has been calculated. The result is displayed in fig. 5.7. Note that although only the overall system length has been changed between calculations, the relative difference of the probe sizes is not constant but rather varies over the considered current range.

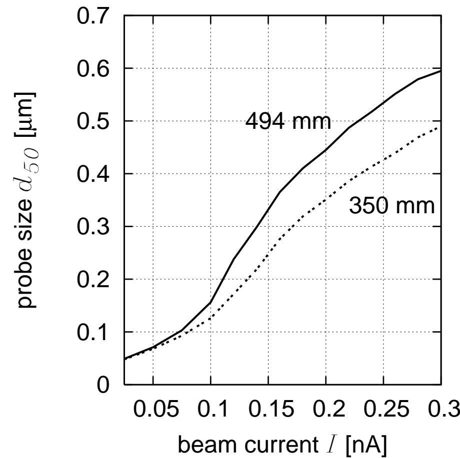

Figure 5.7: Influence of a reduced drift space length on the system performance. Systems are operated in operation mode A with a landing energy of 3 keV.

5.4.2 Fully optimised system performance

Operation mode A. As the experimental setup has been designed for operation mode A (accel mode focusing, ϕ_{lt}=8 kV) the expected optimum system performance for the latter has been calculated for a landing energy of 3 keV. The result is displayed in fig. 5.8a). For comparison also the data for the non-adjusted magnification case is shown. The maximum improvement is found at the maximum considered beam current and amounts to a factor of about 2. Figure 5.8b) shows the calculated fully optimised system performance for a landing energy of 2 keV, again assuming operation mode A.

Influence of the gun lens focusing mode. The required voltage for acceleration mode focusing in the case of the gun lens is one of the critical parameters of the ion beam setup (cf. section 4.3.1). In the light of the above results on the reduced influence of the focusing mode when interactions are taken into account, the effective gain achievable by acceleration mode operation has been more closely investigated.

Figure 5.9 shows the influence of Coulomb interactions on the system performance for the gun lens focused in acceleration and deceleration mode, respectively. The data in a) has been determined on the basis of the optimum

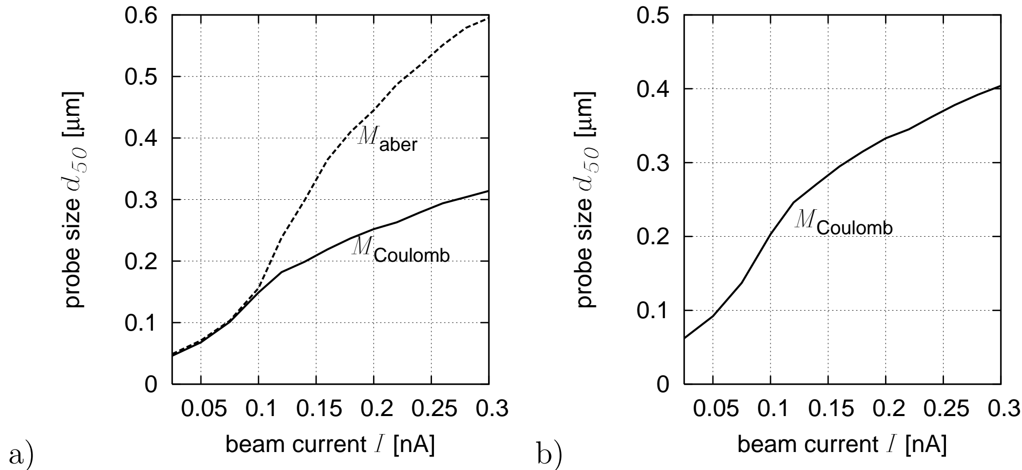

Figure 5.8: Calculated fully optimised system performance of the laboratory system (operation mode A) for two different values of the landing energy. a) Landing energy 3 keV. Also shown is the data obtained in the case of a non-adjusted magnification, i.e. using M_{aber} (but including Coulomb interactions). b) Landing energy 2 keV.

system magnification obtained from aberration-optical calculations, while in b) the magnification has been adjusted to the optimum value including interactions. Consequently, the "artefact" of the deceleration mode outperforming the acceleration mode vanishes. Note however, that the relative gain of using acceleration mode focusing is only about 10-15% on average. Clearly this result must thus be balanced against the possible technical difficulties in lens operation.

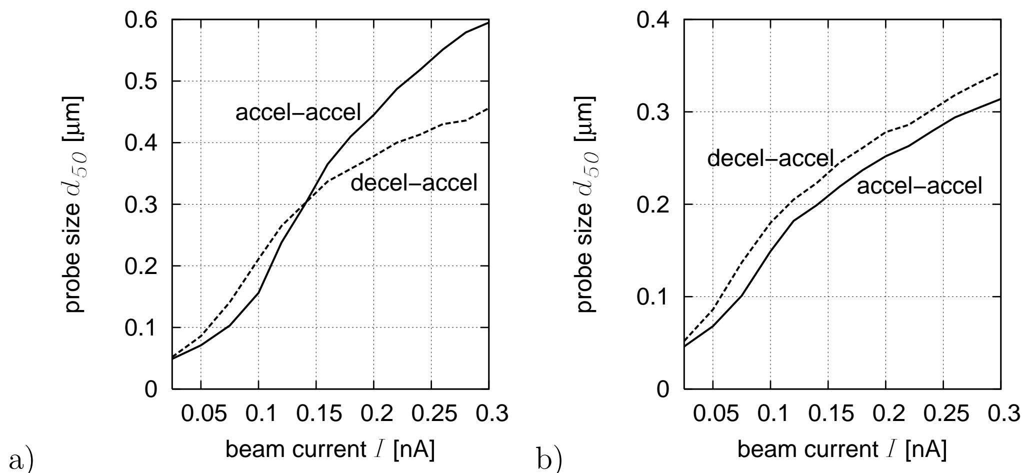

Figure 5.9: Influence of the gun lens operation mode (acceleration or deceleration focusing) on the system performance. a) Calculations on the basis of optimum magnification M_{aber}. b) Fully optimised data corresponding to M_{Coulomb}.

Part III

Experimental System

Chapter 6

Liquid Metal Ion Sources

Due to their high brightness accompanied with operational advantages such as good beam current stability and long life-time, most focused ion beam instruments today rely on gallium liquid metal emitters as ion sources. The general characteristics and aspects of operation of these sources have been dealt with in great detail elsewhere (see for example [102–104]) and will thus not be further discussed here. The focus in this chapter rather is on the specifics of the sources used during this study. The first section discusses source preparation using an proprietary technique, while a second section is dedicated to sources prepared by Dr. Lothar Bischoff of the Forschungszenrtum (FZ) Rossendorf. Due to their robustness even in poor vacuum conditions the latter have proven to be particular suitable for the experimental setup.

6.1 Proprietary sources

An method to prepare gallium liquid metal ion sources was developed during the dissertation of H.P. Mayer [52]. In this, the tungsten carrier material was etched using techniques adopted from the preparation of electron field emitters leading to comparatively small tip radii of only a few hundred nanometres. Consequently, constant emitter heating (with currents of 2-3 A) and good vacuum conditions ($p < 10^{-8}$ mbar to prevent damaging of the tip by ion bombardment) were required during operation. Employing special operation conditions, it was possible to achieve stable ion emission with an energy width (FWHM) of approximately 3 eV. The preparation technique was later also employed by Gnauck [1] and Burkhardt [105] but unfortunately the small energy widths could not be reproduced.

Initially, it was planned to also use these "in-house" sources for the low energy focused ion beam system. A number of working LMIS were prepared that displayed extremely steep characteristic curves (cf. fig. 6.1) and consequently showed a poor emission stability. Furthermore, the life time was limited to only

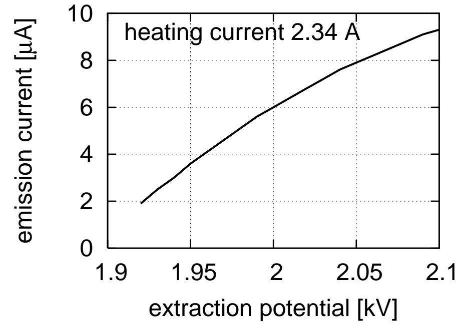

Figure 6.1: Characteristic curve of an "in-house" LMIS displaying a steep gradient of 50 μA/kV for emission currents < 6 μA.

a couple of operation hours. These characteristics were attributed to a deviation from the original preparation parameters which (due to the lack of available time) unfortunately could not be further narrowed down.

6.2 Sources by the FZ Rossendorf

Due to the just mentioned difficulties, the use of commercial LMIS was envisaged. However, this solution appeared to be too cost-intensive in the early experimental stage as the occurrence of voltage flashovers or poor vacuum conditions could not entirely be precluded. As a possible alternative sources obtained on a research collaboration basis from the FZ Rossendorf (Dr. Lothar Bischoff) were investigated (see fig. 6.2). Using a somewhat advanced preparation technique [106,107], these sources stand out due to their comparatively flat characteristic curves (gradients of typically 4 μA/kV) and extremely good long term emission stability. Furthermore due to the relatively large radius of the tungsten base tip of several microns the sources may be operated reliably at $p \approx 10^{-7}$ mbar. The typical life time of the sources is about 800 operation hours which equals the value guaranteed by commercial manufacturers.

With the adoption of these LMIS a distinct improvement in system operability could be achieved compared to earlier setups in which source handling caused more concern. Furthermore, in the course of the transition the type of the emitter carrier socket was also altered for easier and less critical source replacement (see section 7.1.1 for details).

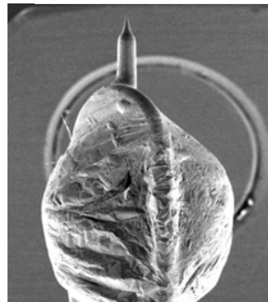

Figure 6.2: SEM image of a typical gallium liquid metal ion source by the FZ Rossendorf.

Chapter 7

Mechanical Design

As outlined in detail above, the envisaged operation mode of the low energy focused ion beam system was determined on the basis of the results of the calculational study presented in chapter 4. In this chapter the focus is now on the practical realisation of the experimental setup in terms of its mechanical system components.

It has to be noted that for the initial laboratory test system a pure ultra-high vacuum (UHV) setup was planned, which later was to be expanded in order to allow the ion beam system to be adapted to a standard (high vacuum, HV) SEM or TEM specimen chamber. Although this procedure somewhat limited the choice on materials and the flange standard, it also resulted in a functioning setup at a relatively early stage of this study. With this, initial experimental experiences could be gained, that in-turn influenced the further development of the ion beam system. Initially, the comparatively small CF35 standard was chosen as basis for the casing in order to keep the system dimensions reasonably small. As will be discussed below, this limitation was later partly abandoned in order to achieve an improved functionality.

In the following, first the mechanical design of the individual system components will be addressed - following the beam direction from the ion gun to the scan deflection system. The layout and design of suitable test setups for UHV and HV operation will then be the subject of a separate section.

7.1 System Components

7.1.1 Gun lens

The very compact setup of Mayer [51] shown in fig. 7.1 (and later also adopted by Gnauck [1]) served as model for the first ion gun design. In the original version titanium electrode carriers are assembled by means of four flange mounted aluminum oxide ceramic (Frialit) rods which are guided through bores on the

outer carrier rim. Once the axial position of the carrier is optimally adjusted, they are fixated by grub screws. The actual lens electrodes consist of movable inserts to the carriers and can be aligned with respect to the fixed extractor electrode bore using a light microscope. The electrodes are connected to high voltage ceramic-insulated feedthroughs on the mounting flange by means of thin titanium rods. With this design a critical step in the lens assembly is the placement of the extractor electrode above the ion source which has to be inserted first. With its four guiding rods the system is mechanically overdetermined and the electrodes get easily stuck. When inserting the extractor electrode thus particular care has to be taken not to accidentally damage the emitter tip. One additional drawback of the design is the fact that for changing the liquid metal ion source the entire gun lens has to be disassembled.

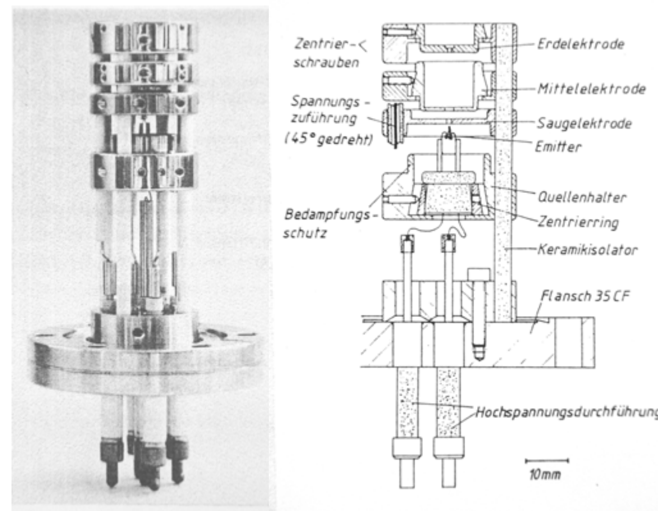

Figure 7.1: Gun lens design by Mayer which served as a model for the initial setup. a) Image of the assembled gun lens ready to be inserted into the housing. b) Schematic drawing of the assembly also showing the emitter base socket with two flexible wires for supplying the heating current. From top to bottom: (left side) centering screws, voltage supply (rotated through 45°), evaporation shield; (right side) ground electrode, focusing electrode, extractor electrode, emitter, emitter support, centering ring, ceramic insulator, flange CF35, high voltage feedthrough. Figures adapted from [51].

Figure 7.2a) shows the improved gun lens design developed during the early phase of this study. Two particularly straight ceramic rods are used to form an optical bench on which the individual lens components are mounted by means of titanium clamps [108]. The electrode bores may be turned without reclamping of the turn parts. Thus the setup may be considered as self-aligning and no additional radial adjustment of the electrode bores is required. The ion source is only put in after assembly and a fine thread allows to accurately control the

distance between emitter tip and extractor electrode. Obviously, this approach also allows an easy source exchange. After assembly the gun lens is inserted into the lens housing shown in fig. 7.2b). The individual lens electrodes are contacted by means of radially attached spring-loaded contact probes (mounted on welded ceramic feedthroughs) while the emitter unit is again contacted by feedthroughs on a CF35 flange. The gun area is kept at UHV conditions by means of a small (2 litre/s) ion getter pump.

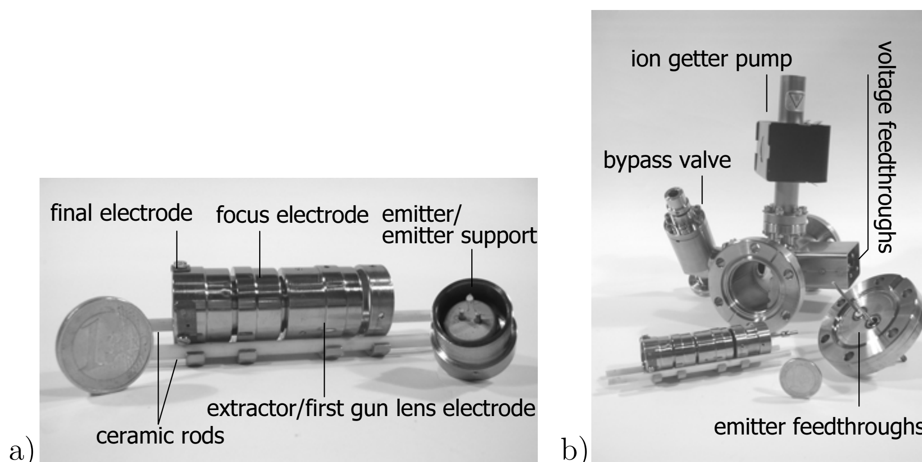

Figure 7.2: Initial gun lens setup. a) Gun lens assembled on ceramic rods ("optical bench"). The emitter unit is to be inserted in the threaded ring shown on the right end. The springs attached to the final lens electrode are used for contacting the isolation valve (see next section). b) Complete gun lens setup including the housing with ion getter pump and UHV bypass valve.

As in the design of Mayer the creepage path length is determined by the distance of support points of neighbouring electrodes. A certain lengthening may be achieved by introducing shallow radial groves on the ceramic rods with which the potential creepage surface becomes orthogonal to the field direction.

While clearly some of the disadvantages of the original design by Mayer are overcome with the just presented setup, the critical issue of source alignment remains unsolved. Practically any commercial ion microscope provides a means of (mostly mechanically) moving the source with respect to the optical axis of the gun lens during operation. Without this, alignment must be optimised in possibly several steps, all implying the demounting of the gun lens. As the result can finally only be judged during operation, this clearly remains an unsatisfactory solution. Thus it was decided to further expand the ion gun in order to provide a means of alignment during operation.

The practical realisation was inspired by the design of a commercial (ETEC Autoscan) gun head which originally was used in an electron beam tester employing a tungsten hairpin cathode and operated under HV conditions. Consequently

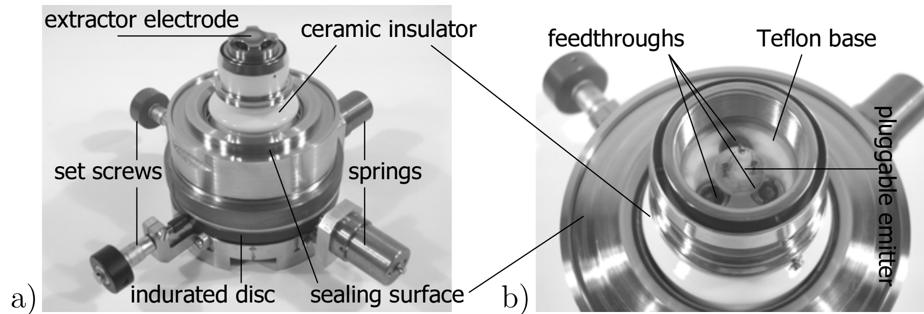

Figure 7.3: Advanced gun head design which allows the emitter to be shifted during operation. a) Complete gun head also showing set screws and opposing springs. b) View on the ion source mounted on a pluggable ceramic base socket for easy exchangeability. The threaded ring is used for screwing on the extractor electrode and aligning the latter with respect to the emitter tip.

- although the basic ETEC design remained unaltered - some changes regarding the choice of materials for the ion gun were required. In particular a high-grade steel corrugated bellow for moving the insulator-mounted emitter unit (also including the extractor electrode, see below) was used in the latter case, whereas in the original ETEC design a Tombak bellow could be employed. The latter material has an unacceptably high outgasing rate for UHV operation due to its comparatively large zinc allotment. Figure 7.3a) shows the thus developed gun head which has an outer diameter of approximately 200 mm. Displacement of the emitter unit in perpendicular directions is achieved by means of two set screws and opposing springs that move a disc of indurated steel to which the ceramic insulator as well as the corrugated bellow are attached. The ceramic insulator provides three high voltage feedthroughs which are all kept on source potential (with two additionally supplying the heating current for the gallium emitter). A two-part extractor electrode carrier is mounted onto a Teflon base that surrounds the feedthroughs and provides sufficient insulation between the emitter and the extractor electrode. The carrier consists of a fixed part as well as a threaded ring into which the actual extractor electrode is screwed - thus again providing a means of finely controlling the tip-electrode distance. Alignment of the electrode bore with respect to the emitter tip is achieved by moving the threaded ring using three grub screws positioned at 120°. Note that originally, it was intended to contact the extractor electrode via one of the feedthroughs within the ceramic insulator. However, as this proved not to be feasible due to insufficient voltage stability, contacting was realised via the first gun lens electrode (see below).

As a consequence of the redesign of the ion gun, also the gun lens had to be reengineered. While the basic concept was not altered the setup was upscaled to suit to the dimensions of the gun head. Figure 7.4a) shows the gun lens assembled on ceramic rods with the radial groves clearly visible. The insulated

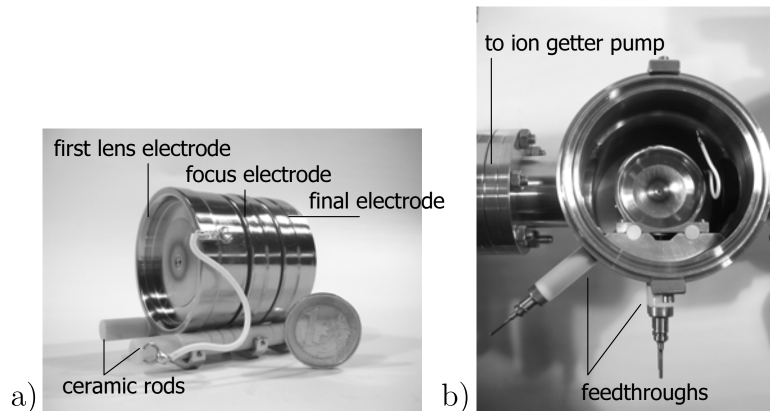

Figure 7.4: Second gun lens design. a) Gun lens assembled on ceramic rods with insulated wire for contacting the head mounted extractor electrode. b) Top view on housing with inserted lens.

wire is employed for contacting the extractor electrode, which - as outlined in section 4.3.1 - is on the same potential as the first gun lens electrode. Note that the actual first lens electrode bore is situated below the bore visible on the image, the latter merely serving as beam stop to limit the current entering the gun lens. The gun lens housing with inserted lens is shown in fig. 7.4b). Due to the increased volume of the UHV region a larger (30 litre/s) ion getter pump is used.

The gun head and the lens housing are connected using a Viton o-ring. Although with the latter in principle UHV conditions are easily maintained within the gun area, problems may arise when the movement of the emitter unit causes a dislocation of the sealing surface. However, the latter usually only occurs at maximum displacement, in which case the gun alignment is better reassessed after dismantling the gun. Prior to bakeout the vacuum within the ion gun is typically ranging from $5{\times}10^{-8}$ to $1{\times}10^{-7}$ mbar.

7.1.2 Isolation valve and beam limiting aperture

An isolation valve is required to separate the gun area (UHV conditions) from the vented specimen chamber during sample change if the ion beam system is to be used as an add-on to a standard SEM or TEM. During operation the valve head is moved out of the valve seat and the valve is open. A small aperture of typically several hundred microns in diameter situtated within the valve seat is used to keep a constant vacuum gradient between gun and chamber. With a chamber vacuum of better than $1{\times}10^{-5}$ mbar aperture diameters up to about 1 mm are acceptable to keep the gun vacuum better than $1{\times}10^{-8}$ [109]. Note however, that the validity of this rule of thumb is still clearly dependent on the available pumping speed and the chamber geometry.

In systems in which the interlens drift space (liner tube) is kept at ground potential, the practical realisation of the isolation valve is comparatively simple. If, however, the liner tube is to be set at high voltage, the valve head has to be insulated from the housing and the valve seat must be an integral part of the liner tube. This requires a vacuum-tight and at the same time insulating connection between housing and valve seat.

When the design of the isolation valve was first addressed, the CF35 flange size was still used as housing standard for the ion beam system and consequently a very compact design was required. Again a commercial solution served as design model: the isolation valve used in field emission SEMs by Carl Zeiss NTS. While the valve head could directly be adopted, realising the insulated valve seat proved to be more complicated.

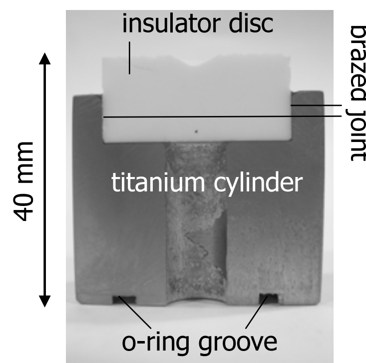

Figure 7.5: Cross-section of the simple test object used in this study to explore the usability of vacuum brazing for manufacturing vacuum-tight joints.

For manufacturing the required leakproof connection between the valve seat, insulator, and housing the technique of vacuum brazing was investigated. Although this method has been succesfully used for joining titanium electrodes to a ceramic insulator (Macor or Vitronit) before [110, 111], the leak tightness of the joints had not been an issue then. The possible applicability of the technique for this study was assessed using the simple test part shown in fig.7.5 in which a Vitronit disc is used to seal off a titanium cylinder. The brazing process (including the choice of materials) was adopted from Kienle and is described in detail in [110]. Using a standard leakage detector, the test object proved to be perfectly vacuum-tight.

Although the technique was thus found to be principally suitable, the manufacturing process is slightly more complicated in the case of the actual valve unit. Two circular brazed joints are required in order to join the valve seat with a ceramic insulator ring which in turn has to be joined to the lens housing. These joints must be manufactured in a single processing step as it cannot be ruled out that they disintegrate during a second heating. A further difficulty arises

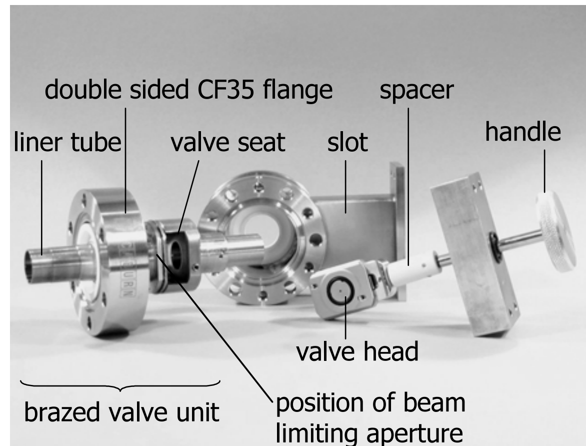

Figure 7.6: Disassembled valve unit indicating the position of the beam limiting aperture. The UHV region is to the left of the brazed component, i.e. the valve seat is situated in the HV region.

from the fact that three different materials have to be joined: titanium (valve seat), Vitronit (insulator), and high-grade steel (housing). While the thermal expansion coefficients of these materials are fairly similar, the geometries of the individual components are clearly not. Consequently, it was decided to manufacture the valve part containing the critical joints as a separate unit using a two sided CF35 flange as housing as shown in the left part of fig. 7.6. Two of these units were manufactured and tested successfully with respect to insulation and leak tightness. In one additional case the mechanical stress during the brazing process caused superficial cracks within the Vitronit ring. Although a leakage test proved to be negative, the unit was nevertheless not used in the setup. The valve head is guided within a narrow slot and insulated from the housing/handle using a ceramic spacer (cf. fig. 7.6). The dimension of the slot later proved to be critical with respect to high voltage flashovers. In one case a flashover partly burnt the valve head's o-ring (cf. fig. 7.7) and caused the gun to be aerated during a sample change. As the aperture within the valve seat also serves as beam limiting aperture a comparatively small diameter of 100 μm was chosen. With this, the gun vacuum is not gaugeably affected when the valve is opened.

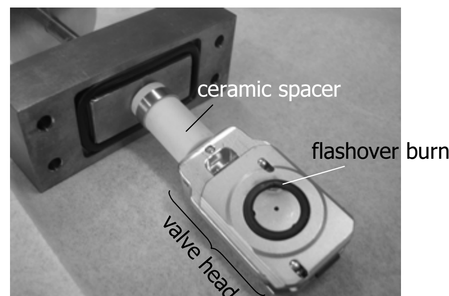

Figure 7.7: View on the valve head showing a partly burnt Viton o-ring.

7.1.3 Stigmator and beam alignment unit

Deviations from rotational symmetry of individual lens components, e.g., due to manufacturing tolerances, may cause an elliptic beam shape - the beam becomes astigmatic. In order to restore the circular profile a stigmator must be used. In an ion beam system the latter usually consists of two electrostatic quadrupoles arranged at an angle of 45° to allow correction in arbitrary directions. If the excitation of the first and second quadrupole is characterised by parameters U_1 and U_2 (for example representing the quadrupole voltage), respectively, the strength S and angle of correction ϑ (measured with respect to the x-axis, direction of U_1) of the stigmator are given by

$$S = c\sqrt{U_1^2 + U_2^2} \qquad \tan 2\vartheta = U_2/U_1 \tag{7.1}$$

where c is a geometry-dependent constant.

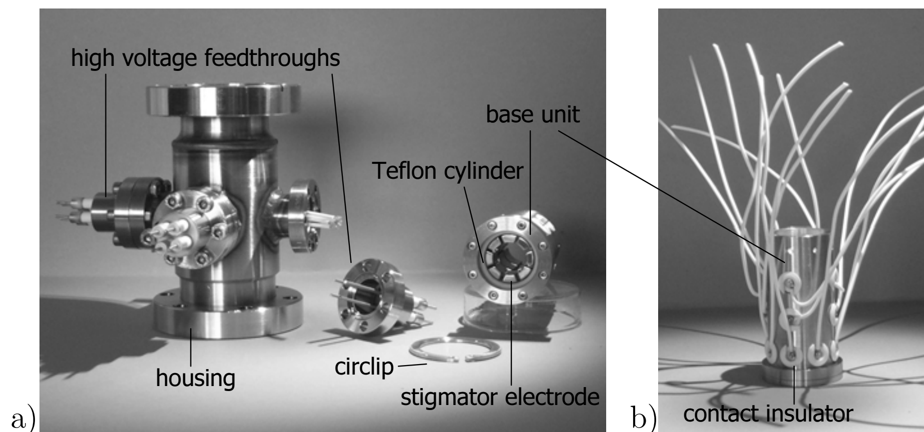

Figure 7.8: Stigmator/beam alignment unit. a) Partly disassembled unit showing an inside view of the base unit with the electrode configuration. b) Wired base unit. Additional contact insulators surrounding the threaded rods provide increased dielectric strength.

A deflection unit within the interlens drift space is required to align the beam to the optical axis of the objective lens after passing the beam limiting aperture. Ideally a double-stage deflector is used, which not only allows an angular deflection correction but also makes a parallel shift of the beam possible. With the correction voltages of the individual deflectors being typically small compared to the beam potential, a simple dipole geometry is expected to be acceptable in terms of introducing additional deflection errors.

Again, in systems in which the drift space is at ground potential, the realisation of these alignment elements is rather straightforward. However, with the drift space on high voltage, stigmator and alignment unit must be an integral part of the liner tube, i.e. must be insulated from the housing. Figure 7.8a)

shows the practical realisation of the stigmator/beam alignment unit for the low voltage ion beam system. Again the CF35 flange size was used as housing standard. The unit has been deliberately designed as a separate component in order to prevent possible redesigns to affect the overall system setup. The individual electrodes of the stigmator and double-stage deflector are first attached to the inner surface of a Teflon cylinder by means of threaded rods. The latter are guided through circular openings and screwed to the backside of the electrodes which are thus pressed against the insulator's inner surface. For an increased mechanical stability the Teflon cylinder is then inserted into a high-grade steel cylinder and the threaded rods are used for attaching insulated wires as shown in fig. 7.8b). This base unit is put into the housing and fixated using a circlip. Commercial high voltage (5kV) CF16 multi-pin feedthroughs (Caburn Ltd.) are employed to contact the wires. The overall stigmator/beam alignment unit has been tested for a dielectric strength of ± 6 kV with respect to ground. The maximum possible interelectrode voltage difference is about 1 kV.

7.1.4 Liner tube and objective lens

For the originally envisaged application of the low energy focused ion beam system as an add-on to a SEM the part of the liner tube starting below the stigmator/beam alignment unit has to bridge the distance between the host system's entrance port and the objective lens. For the experimental setup the length of the liner tube and the geometry of the objective lens were chosen to make the system compatible to the specimen chamber of a Carl Zeiss NTS Gemini microscope (see also discussion in section 4.3.2). Under the precondition that the FIB working distance is to be kept at a minimum and assuming post-lens deflection for the ion beam system, the liner tube length inside the specimen chamber amounts to 188 mm. A titanium tube with an inner diameter of 12 mm is used, which has been slotted at several positions along its length to improve vacuum conditions (see discussion in section 7.2.2). The tube is supported at two positions using Teflon rings.

As shown in fig. 7.9 the liner tube diameter is reduced at its far end to form the first objective lens electrode. As noted previously the dimensions of the objective lens are adopted from the design of Orloff and Swanson [91]. The focusing and the final (grounded) electrode have to be tapered to allow a small working distance with the likewise tapered Gemini objective lens. Creepage paths and voltage stability are designed to enable accel mode focusing (typical focus voltage $\approx$ -7 kV with respect to ground at 3 keV landing energy, assuming $\phi_{\mathrm{lt}} = 8$ kV and a working distance of 15 mm). Teflon is used throughout as insulating material. The final electrode is part of a grounded cylinder that shields the liner tube to prevent any disturbances to the host system due to the high potential ϕ_{lt} of the liner tube. Several elongated holes in the shield cylinder improve vacuum conditions. Additional bores in the tapered end of the final electrode allow the

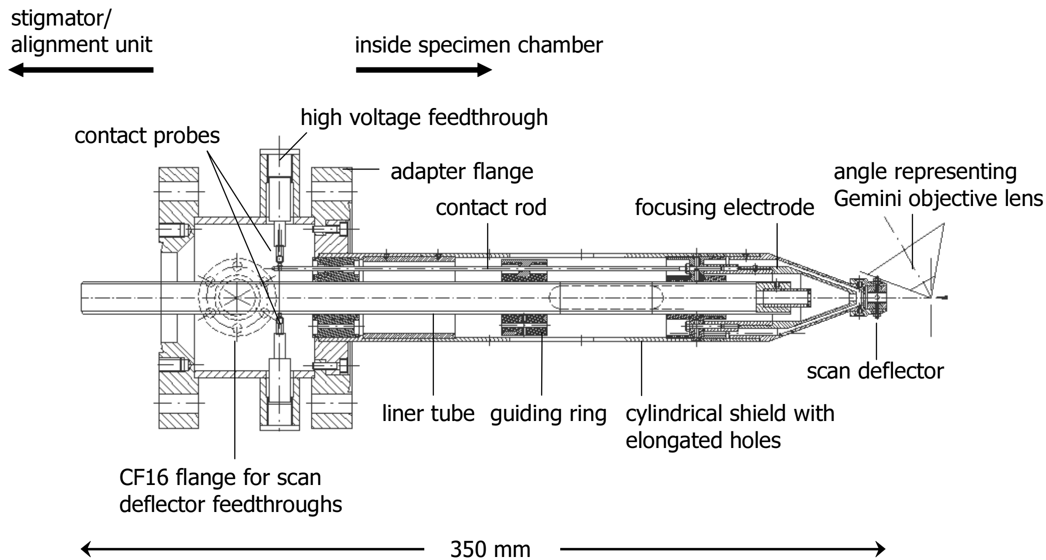

Figure 7.9: Technical drawing of liner tube and objective lens region of the low energy focused ion beam system. The dimensions are chosen for the system to be suitable as an add-on to a standard Gemini microscope specimen chamber (Carl Zeiss NTS).

lead through of wires to contact the scan deflector (see also following section). Both, focusing and final electrode can be aligned with respect to the first electrode bore using three grub screws arranged at 120°. Contacting of the liner tube as well as the focusing electrode is realised using spring-loaded probes that are mounted on commercial high-voltage feedthroughs, which are screwed into the housing after the assembly has been completed. In the case of the focusing electrode the probe contacts a titanium rod which at its far end is screwed into the electrode support. A ceramic ring attached to the liner tube approximately at half length is used to guide this contact rod as well as the wires used to contact the scan deflector. An additional guiding ring is positioned at the proximal end of the liner tube.

7.1.5 Scan deflector

A simple post lens deflector is used for scanning the beam for image acquisition. Two parallel plate dipole elements as shown in fig. 7.10a) generate the scan field in x- and y-direction. The insulator-mounted deflector unit is attached to the tapered end of the objective lens' final electrode (see fig. 7.10b)). Four wires are guided from a CF16 flange situated just above the adapter flange (cf. fig. 7.9) to the final objective lens electrode, where bores allow them to be lead through to the deflection electrodes. The latter are attached to the insulator as in the case

of the beam alignment unit: threaded rods are guided through circular openings within the insulator, screwed into the electrode back, and fastened using small nuts. Although the scan voltages are comparatively low and the deflector is operated with respect to ground potential, high voltage insulated wires have to be used as an accidental contact with the liner tube cannot be ruled out. With the wires being guided entirely within the grounded housing/shielding cylinder, a compact setup is obtained that may easily be adapted to a SEM/TEM specimen chamber. Note that in order to prevent disturbances to the image acquisition system (secondary electron detector) the scan deflector is additionally shielded (cf. section 7.2.2).

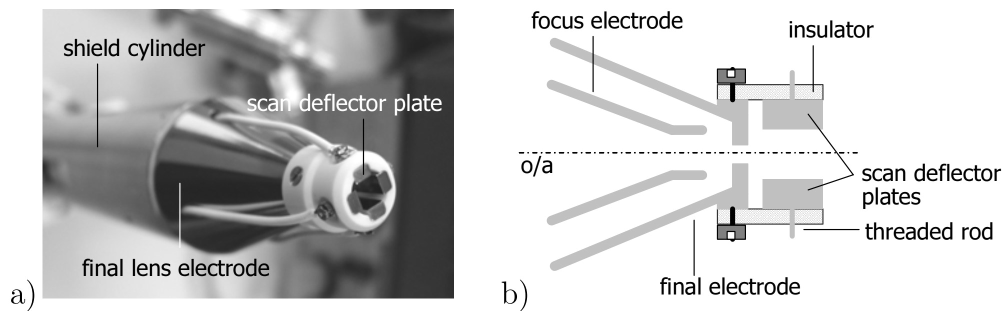

Figure 7.10: a) Perspective view of scan deflector unit. b) Schematic drawing showing how the scan deflection unit is attached to the objective lens' final electrode.

7.2 Test setup design and preliminary experiments

7.2.1 UHV test setup

The initial UHV test setup with horizontally adapted ion beam column is shown in fig. 7.11a). Note that in contrast to the drawing of fig. 7.9 the adapter flange part was based on a CF35 housing for this first system. As work on the vacuum brazed isolation valve was still in progress, a commercial substitute was used, that however did not allow immersion operation. Furthermore, with the power supply available at that time (supply as used by Gnauck, see [1]), only one stage of the beam alignment deflector could be used (stigmator and second stage grounded).

A simple sample holder carrying a TEM100 copper grid was used in the initial experiments. It was mounted on ceramic rods (employing the technique used for the gun lens) and attached to a CF35 flange. The working distance was determined by the length of the rods and consequently could not be varied during operation. Unfortunately, with this setup also a shift of the sample in directions perpendicular to the beam axis was impossible. For secondary electron detection a dedicated UHV Everhart-Thornley detector (ETD) was developed, for which the normally used Perspex light guide was substituted by a glass light guide [112]. The very compact detector design is shown in fig. 7.11b).

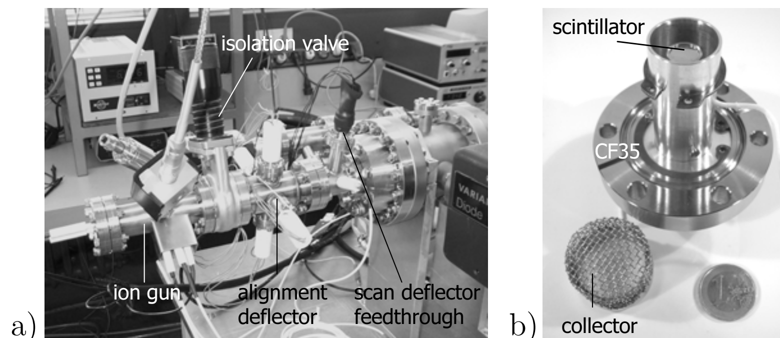

Figure 7.11: a) UHV test setup with horizontally adapted ion beam column. b) Purpose-built UHV Everhart-Thornley detector.

With this very simple and somewhat incomplete setup, first secondary electron images ("beam down") could be acquired as shown exemplarily in fig. 7.12. Note that no beam limiting aperture was used. From these first experimental data - albeit obtained with limited power supply - it became evident that for better imaging results an improved sample handling and an optimised detector-sample geometry was required.

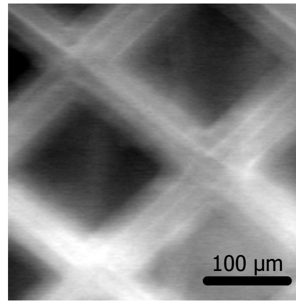

Figure 7.12: Exemplary secondary electron image of a TEM100 copper grid. The image displays a poor signal-to-noise ratio, a distinct fading of the grid bars, and are partly overshone due to the sample-ETD geometry.

7.2.2 HV test setup

ISI SMS 2 chamber. With the availability of a vacuum brazed isolation valve the pure UHV test system was abandoned in favour of a differentially pumped UHV/HV system. The ion beam column was first adapted to the specimen chamber of an ISI SMS 2 scanning electron microscope as shown in fig. 7.13a). A sample stage allows three-dimensional specimen shift as well as tilt and rotation. The chamber is equipped with a customised secondary electron detector (see fig. 7.13b)).

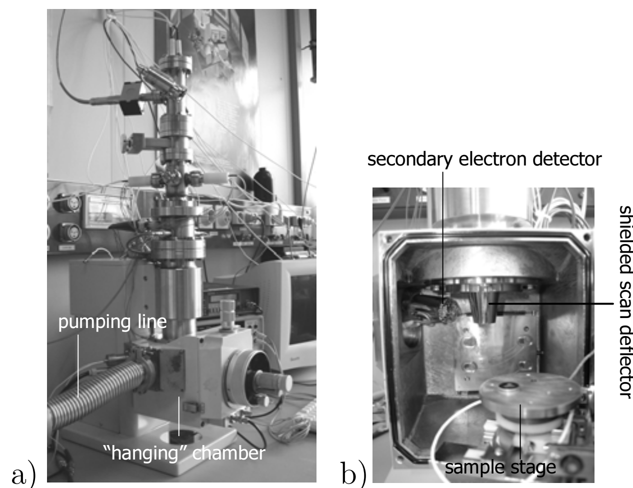

Figure 7.13: a) HV test setup using the ISI SMS 2 chamber. b) Inside view of the specimen chamber.

The system was again operated employing the power supply as used by Gnauck [1] but images were acquired with a beam limiting aperture (differential pumping aperture) of 150 μm in diameter. Exemplary images are shown in fig. 7.14. Obviously, the image quality in terms of signal-to-noise ratio and resolution is

significantly superior compared to the previous setup.

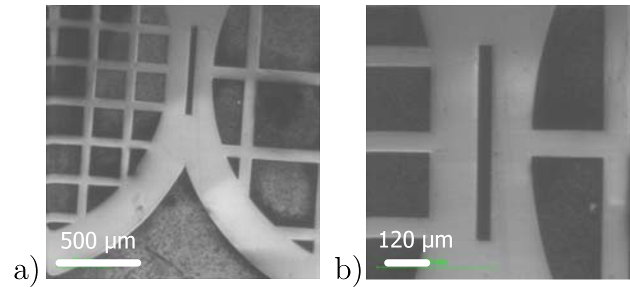

Figure 7.14: Secondary electron images of a TEM100/50 copper grid at a working distance of 36 mm and a final beam energy of 6 keV.

However, due to the "hanging" chamber geometry, the mechanical stability of the test setup was feared to become possibly critical if the redesigned gun head and gun lens (see section 7.1.1) were to be adapted to the ion beam column. Furthermore - and even more severe - was the fact that with the specific pumping setup of the ISI chamber only a HV vacuum of approximately 3×10^{-5} mbar was achievable which is insufficient for the remaining gas molecules not to influence the ion beam: in the case of an accelerated ion (radius r_{ion}) entering a gas volume (molecule radius r_{gas}) the mean free path length λ is calculated according to [113]

$$\lambda = \frac{kT}{\pi(r_{\text{ion}} + r_{\text{gas}})^2 p} \tag{7.2}$$

with k, T and p being the Boltzmann constant, absolute temperature, and pressure, respectively. Taking the value $r_{\text{gas}} = 320$ pm of N_2 for air (reference [113]) and $r_{\text{ion}} = 62$ pm [114] for the gallium ions and assuming a temperature of 20°C, the mean free path length of the ions within the HV setup is approximately 2.9 m. As this corresponds to about six times the length of the HV part of the liner tube, the value appeared to be just acceptable. However, direct vacuum measurements at the scan deflector feedtrough (see fig. 7.9) showed that the vacuum in the liner tube region is approximately one order of magnitude worse than the chamber vacuum, resulting in a correspondingly reduced mean free path length of about 0.29 m.

As a consequence of these considerations, it was decided to improve the system's mechanical stability and vacuum conditions by adapting the ion beam column to a more suitable specimen chamber.

Cambridge S180 chamber. With the adaptation of the ion beam column to the specimen chamber of a Cambridge S180 scanning electron microscope (see fig. 7.15), vacuum conditions could be significantly improved. A large (300 litre) turbomolecular pump is directly attached below the chamber using the maximum

possible pumping cross-section. Consequently a HV base vacuum of typically 6×10^{-7} mbar can be achieved. The vacuum within the liner tube region has also been improved by adding a pumping bypass flange opposite the scan deflector feedthrough and by introducing several slots along the liner tube. Measurements confirmed that the liner tube vacuum is approaching the chamber vacuum after a few hours pumping time.

With its larger mass and being supported on a stable metal frame, the setup also provides sufficient mechanical stability for the newly designed gun area.

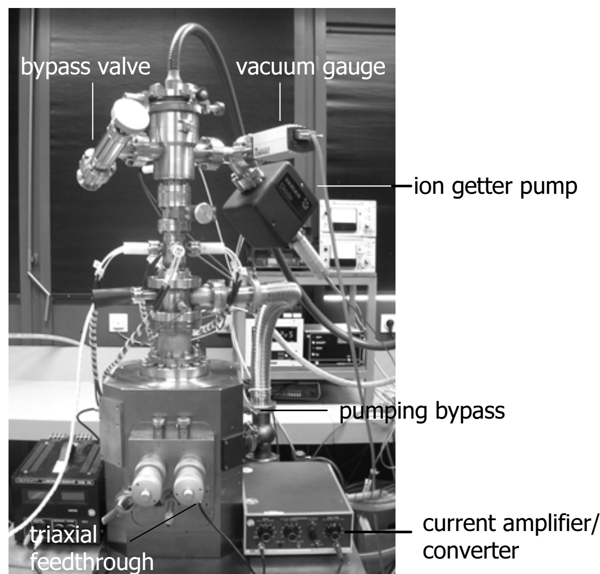

Figure 7.15: Final HV test setup. Ion beam column adapted to a Cambridge specimen chamber.

A sample stage allows specimen translation, rotation, and tilt. The chamber again provides a customised secondary electron detector for imaging and has been additionally equipped with a triaxial current feedthrough for undisturbed measurement of the Faraday cup signal. The latter is either directly used for exact determination of the beam current (typically 50-100 pA) or may be amplified and converted to a voltage signal (using a Keithley current amplifier model 427) for acquiring transmitted current images (see also fig. 8.1). The design of the Faraday cup has been adapted from [115] but has been further improved to provide complete triaxial signal routing.

Chapter 8

Power Supply

As in the case of the just described mechanical design, the implementation of immersion mode operation and accel mode focusing for the low energy focused ion beam system requires a comparatively more demanding column power supply as in the case of standard operation. One major challenge is the realisation of the stigmator and beam alignment unit, which is operated with respect to liner tube potential.

As noted briefly in section 7.2 above, initial experiments were carried out using the supply as used by Gnauck [1] (and provided by Bal-Tec AG, Principality of Liechtenstein) which clearly does not support immersion or accel mode operation. While the development of an improved and purely software controlled supply with added functionality was again started in close cooperation with Bal-Tec, this is still work in progress.

The main focus of this chapter is the description of the proprietary supply with which all of the experimental data presented in the following chapter have been obtained. A separate section is dedicated to a short description of the image acquisition system. For illustration, fig. 8.1 shows a schematic block diagram of the complete setup.

8.1 Column supply

Stability requirements. Any voltage supply is characterised by a remaining voltage ripple that in principle has to be considered when calculating the size of the chromatic aberration disc d_c. Assuming statistically independent contributions, eqn. 4.14 can analogously be expanded to give

$$\begin{aligned} d_{\mathrm{c,RPS}} &= 0.34\, C_{\mathrm{c}} \alpha \sqrt{(\Delta\phi/\phi)^2 + \delta_1^2 + \ldots + \delta_n^2} \\ &\leq 0.34\, C_{\mathrm{c}} \alpha \sqrt{(\Delta\phi/\phi)^2 + n\delta_{\mathrm{max}}^2} \end{aligned} \tag{8.1}$$

where $\delta_1, \ldots, \delta_n$ denote the relative voltage ripples of the n supplies used, and δ_{max} equals the corresponding maximum value. In the case of an ion beam with

energy width $e\Delta\phi = 5$ eV and a mean beam potential $\phi = 4$ kV, a maximum voltage ripple of $1{\times}10^{-4}$ is acceptable resulting in

$$\sqrt{(\Delta\phi/\phi)^2 + n\delta^2_{\max}} = \sqrt{1.6 \times 10^{-6} + 1 \times 10^{-7}} \approx \Delta\phi/\phi$$

for $n = 10$ individual supplies.

High voltage supplies. The gun supply originally used by Mayer [52] has been slightly modified and an Applied Kilovolts HP series cassette (voltage ripple $\leq 10^{-6}$) is now used for generating the emitter base voltage. The built-in heating current supply has been adapted to provide a maximum current of 3 A.

Applied Kilovolts HP series cassettes are also used for supplying the extractor and the liner tube voltages, respectively.

The focusing voltages are generated using bipolar supplies by FUG Rosenheim (HCN 35 12500 and HCN 35 M 6500, respectively) with a voltage ripple of typically 5×10^{-5}. The latter are additionally equipped with an analogue programming port for remote control with which an input voltage range of 0-10 V can be transformed to the maximum voltage range of the supply. In this study the feature was used to wobble the focusing voltages for beam alignment using a common sawtooth pulse generator (see section 9.1).

Beam alignment deflector supply. To enable immersion operation the beam alignment deflector supply is always operated with respect to liner tube potential. The maximum deflector voltage is ±500 V. Each of the four deflector pairs of the beam alignment unit is addressed simultaneously, with one plate set to the positive and the opposing plate set to the negative voltage value of same modulus. With this setting, ideally, the on-axis potential always equals the liner tube potential. Apart from independent control of the individual deflector pairs, it is also possible to excite the two deflector stages using a variable factor. With this, the system operation is significantly simplified. Note that in the current setup this factor is variable between one and three and applies equally to both deflection directions.

Stigmator supply. The development of a software controlled stigmator supply was addressed in form of a final year project within the scope of a collaboration with the University of Applied Science (Fachhochschule für Technik) Esslingen [116]. The maximum stigmator voltage is ±200 V. An additional deflector voltage can be superposed to align the mechanical stigmator axis with the system's optical axis. The quality of alignment may be controlled by wobbling the stigmator voltage using a variable wobble amplitude and frequency. The functionality of the supply has been benchmark tested and a malfunction in the addressing of one of the eight output channels has been found. Unfortunately, this remaining problem has so far prevented the use of the supply within the experimental setup.

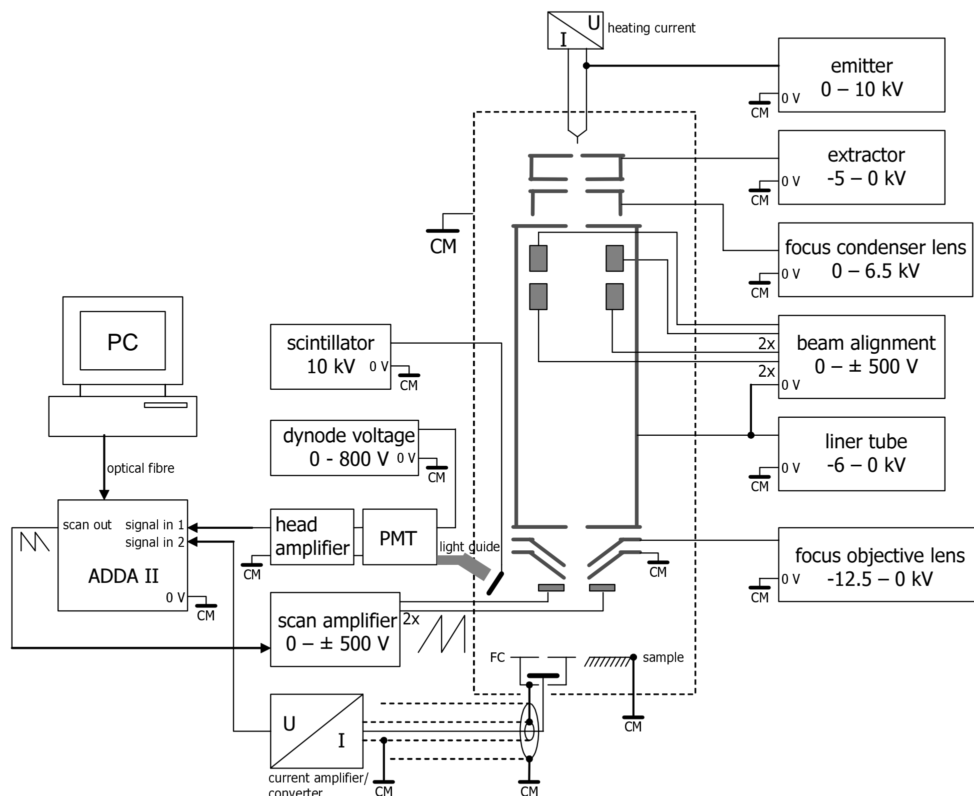

Figure 8.1: Schematic block diagram of the power supply and image acquisition setup. To minimise interference, the signal ground (0 V) of each individual power supply is referenced to a central mass (CM) plate attached at the specimen chamber while the housings are connected to the protective earth conductor. PMT = photomultiplier tube, FC = Faraday cup.

8.2 Beam scanning and image acquisition

The commercial ADDA II unit (Soft Imaging Systems, Münster), which has been successfully used in several other experimental studies (see e.g. [117,118]) before, is used as the base component for the image acquisition setup. The built-in computer controlled sawtooth generator provides analogue x (line) and y (frame) ramp signals with variable amplitude and frequency which are fed into a proprietary scan amplifier. The thus amplified signals are then directly supplied to the scan deflector and the specific choice of the amplification factor consequently determines the imaging field-size for a given working distance. Currently, the amplification factor is variable in discrete steps ranging from 0.5 to 50, resulting in maximum deflection voltages of approximately ±500 V for maximum input voltages of ±10 V.

Image (voltage) signals are digitised synchronously to the scanning ramps after being fed into one of the ADDA II's user-adjustable input channels and are

subsequently displayed using the analySIS program. For optimum performance the image signal amplitude should be of the order of 1 V. In the case of the secondary electron detector, the adjustment is easily achieved by suitably choosing the continously variable dynode voltage of the photomultiplier tube. For the Faraday cup (FC) signal, for which only discrete amplification steps (with limited continous fine-tuning) are possible using the current amplifier/converter, the adjustment is slightly more time-consuming.

Chapter 9

Experimental results

After the mechanical design of the low energy ion beam system and the layout of the test setups has been discussed in some detail in the previous chapters, in the following the emphasis is on the experimental results obtained.

In a first section the standard procedure for beam alignment will be introduced and some remaining limitations of the current setup will be pointed out in that context. A second section will then be dedicated to the evaluation of the experimental data.

9.1 Beam alignment

After any major intervention in the setup (e.g., aperture/source change or realignment of lens parts) the beam has first to be threaded down the ion beam column. For this purpose, generally any of the voltage feedthroughs may be used for current measurement. However, due to electronic background noise and the typically low current amplitude, coaxial feedthroughs are most suited for this task. While the feedthroughs for the liner tube and the focusing voltage of the objective lens (cf. fig. 7.9) are already designed for coaxial connection, special measurement contacts have been developed for the gun lens. During the initial alignment step, the probe current is monitored using a commercial picoamperemeter (Keithley model 427) which allows reliable detection of beam currents of the order of 1 pA.

Once "beam down" has thus been achieved, the output of the secondary electron detector (head amplifier) may be used for maximising the beam current to the probe. For this purpose the beam is not scanned but rather operated in spot mode. Here, the amplitude of the video signal (either observed on a oscilloscope or using the image acquisition software) is assumed to be about proportional to the probe current. The current through the beam limiting aperture can only be maximised using the gun shift described in section 7.1.1. However, any change to the gun lens excitation, e.g., a different extraction or focusing voltage, clearly nullifies this alignment. Note that usually the gun shift is only used to align

the source to the gun lens' optical axis and an additional alignment deflector is employed for maximising the beam current through the aperture (see e.g., alignment procedure in [110]). With the somewhat limited setup used in this study, the maximum achievable beam current at any alignment stage is of the order of 100 pA.

The next step typically involves setting up the image acquisition. Using the maximum possible scanning voltage a very large field of view can be imaged - the actual size clearly depending on the working distance and the beam energy. At these large scanning voltages the performance of the scan amplifier deterioates significantly as shown exemplarily in fig. 9.1. Nevertheless, using this setting, a desired sample position, for example the entrance aperture of the Faraday cup or a suitable test object, can easily be selected. The image quality is then maximised at increasingly higher magnification (i.e., smaller scanning area) by adjusting the focusing voltage settings.

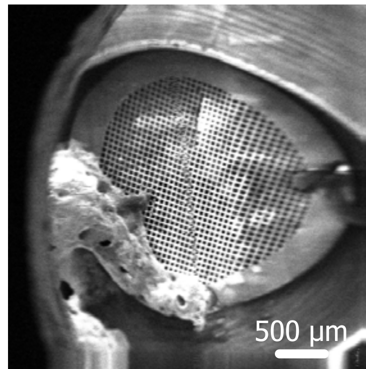

Figure 9.1: Exemplary secondary electron image of a TEM400 copper grid at maximum field of view (scanning voltage). Working distance 15 mm, beam energy 3 keV. The image exhibits strong distortion at the right and bottom edge caused by the deterioation of the scan amplifier performance and beam misalignment. The circular structure at the left edge is part of the deflector shield cylinder.

Subsequently, the beam axis is aligned to the optical axis of the objective lens by using the previously mentioned (see section 8.1) programming feature of the focusing voltage power supply. The procedure relies on image acquisition of a suitable test object (e.g., a TEM copper grid) using the ETD signal. The output of a common sawtooth generator is used as input to the programming port. An adjustable offset of the signal generator initially allows the output voltage of the high power supply to be tuned to approximately the focusing voltage. When the sawtooth amplitude is slowly increased, the image begins to move synchronously to the sawtooth frequency. The amplitude of the movement determines the state of alignment, with a minimum amplitude (ideally zero amplitude) representing the optimum. Minimisation is achieved by suitably exciting the double-stage alignment deflector. Note, that in order to properly visualise the movement, the frame frequency of the image acquisition system has to be larger than the sawtooth frequency. As the maximum pixel frequency of the ADDA II unit is

limited to 1 MHz, this is achieved by choosing a small image size, e.g., 128×128. A certain fine tuning is also possible by suitably adapting the sawtooth frequency, which is usually $\leq$ 1 Hz. Note that this procedure is commonly used in the alignment of any scanning electron microscope, see for example [119]. An alternative alignment procedure also relying on an ADDA II unit has been used in [118]

Even though the amplitude of line-bound interference has been tried to be minimised by appropriate signal mass routing, i.e. connecting the 0 V reference of all power supplies (where possible) to a central mass point at the ion column (see fig. 8.1), a certain mains electromagnetic interference remains visible on the acquired secondary electron images. By choosing the line frequency an integer multiple of the mains frequency, this effect can be partly compensated. Note however, that this method clearly limits the maximum frame frequency and thus is only employed for acquiring images to be used for probe size determination. Naturally, the impact of interferences becomes more severe for images employing the Faraday cup current (i.e., current transmitted through a TEM grid, shadow image) as input signal. This may be attributed to the comparatively much lower signal amplitude and considerably poorer signal to noise ratio.

9.2 Measurements

The resolution of the low energy focused ion beam system has been assessed mainly by visual inspection of secondary electron images, that is the smallest visible structure contrast is used as an estimate for the resolution. Throughout the experiments a beam limiting aperture with a diameter of 100 μm was used and the working distance was kept at approximately 15 mm. The liner tube voltage was V_{booster} = -5 kV. Note that due to remaining problems with the dielectric strength of the condenser lens (limited flashover stability), the latter was operated in internal deceleration mode. As noted in the previous section, the beam current was typically ranging from 80 pA to 120 pA. The minimum possible beam energy that has experimentally been achieved was 1.6 keV. For even lower energies, the liner tube voltage has to be decreased to allow focusing (see discussion in section 4.3.2 and cf. fig. 4.7). At the minimum possible energy the image quality is extremely poor as shown in fig. 9.2.

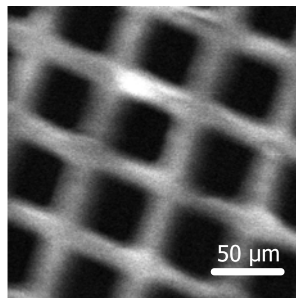

Figure 9.2: Secondary electron image at a beam energy of 1.6 keV, which corresponds to the minimum value for a liner tube voltage of V_{booster} = -5 kV.

Figure 9.3a)-c) shows exemplary images used for resolution measurement at different beam energies. The resolution appears to be limited by residual astigmatism which - in the current setup - cannot be compensated. From these images, the resolution has been estimated to be 300-400 nm for beam energies of 3 keV and 4 keV, respectively. For a beam energy of 2 keV a resolution of 500-600 nm has been found. Figure 9.3d) shows an image of a standard tin on carbon sample commonly used in SEM for resolution measurement.

For energies of 2 keV and 3 keV, respectively, the probe size was also quantified by the knife-edge method using transmitted (Faraday cup) current images as shown exemplarily in fig. 9.4a). Assuming a Gaussian beam profile, the probe size is defined as the rise distance from 12%-88% of the signal intensity (see fig. 9.4b)). A value of 1 μm has been found for both energies. Note however, that apart from the expected deviation of the beam profile from a Gaussian distribution, the applicability of this method for probe size quantification in the low energy ion beam setup is also limited by the roughness of the grid bars and the poor signal to noise ratio.

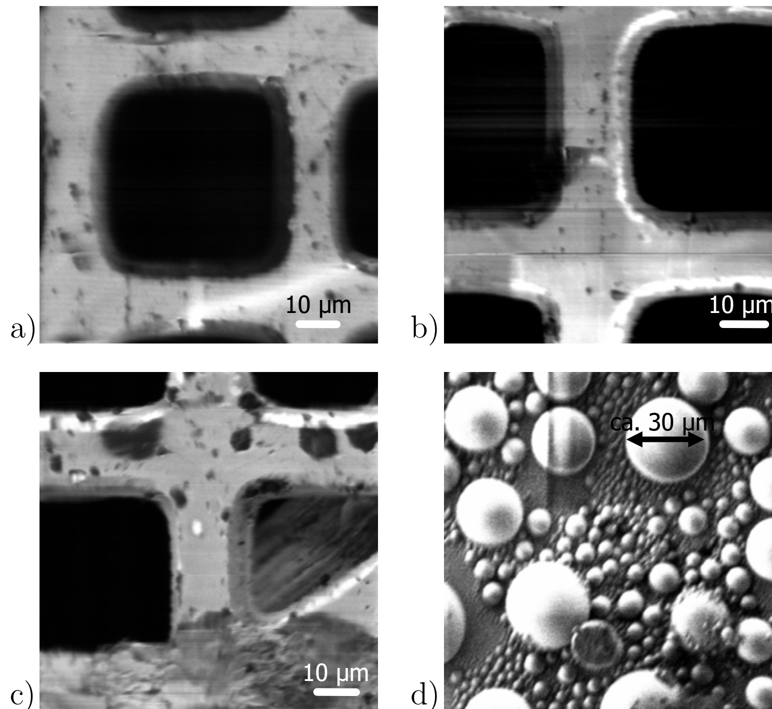

Figure 9.3: Secondary electron images used for resolution measurement. Beam energy a) 2 keV, b) 3 keV, and c) 4 keV. d) shows an image of a standard tin on carbon sample at 3 keV beam energy. The size of the largest sphere is approximately 30 μm.

A quantitative comparison of the system performance at low energies using FFLV-R and FFLV mode (fig. 9.5a)) operation, respectively, has not been attempted. For a meaningful result, the systems should be operated in their respective optimum magnifications, which - given the alignment limitations - cannot be realised with the current setup for an arbitrary combination of beam energy and operation mode.

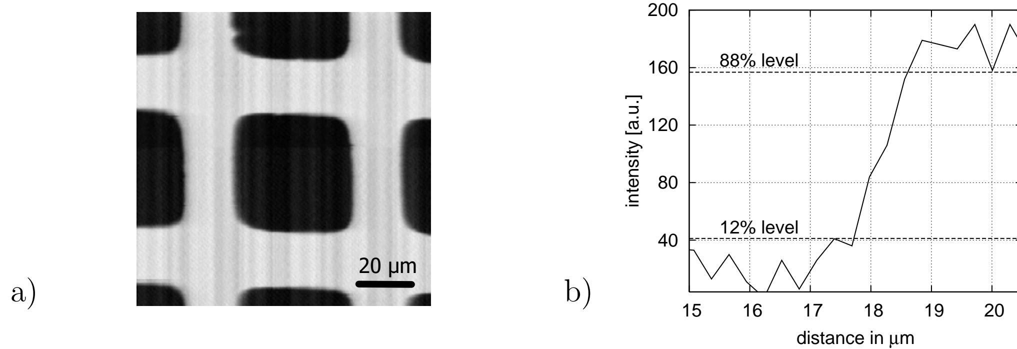

Figure 9.4: a) Transmitted current image of a TEM400 copper grid at 3 keV energy used for probe size determination employing the knife edge method. The vertical lines are artefacts arising from electromagnetic interference. b) Linescan across grid bar indicating the 12% and 88% levels of the signal intensity. The probe size in this case is found to be approximately 1 μm.

At landing beam energies larger than 4 keV the liner tube voltage is reduced to zero, and the system is operated in non-immersion mode. Currently, the maximum beam energy is 7 keV (fig. 9.5b)) and limited by the extractor electrode power supply. Initial measurements indicate an inferior resolution compared to the immersion mode images, albeit this may also be a result of insufficient alignment or the influence of astigmatism.

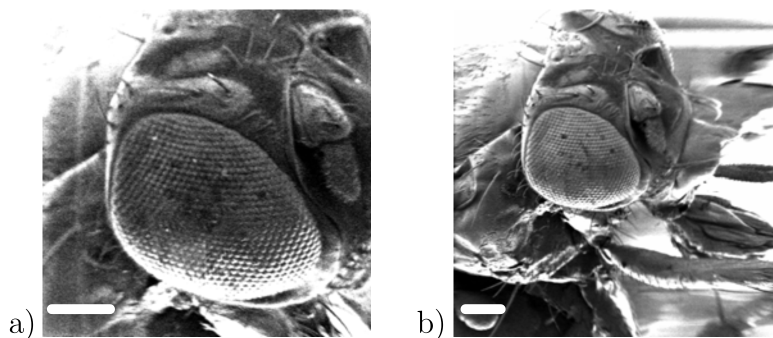

Figure 9.5: Secondary electron images of drosophila melanogaster (fruit fly). a) FFLV mode at 3 keV landing energy. b) Landing energy 7 keV. The length of the measuring bar (lower left corner in both images) roughly equals 100 μm.

Part IV

Summary and Outlook

Chapter 10

Summary

In this study a novel approach towards low energy focused ion beam system design and operation has been presented. The system performance has been investigated both theoretically as well as experimentally using a newly developed ion beam column.

Initially a thorough aberration-optical analysis has been carried out, which comprised the calculation of first-order optical properties and aberration coefficients of individual optical components as well as of the overall system. The results of this analysis have been used as a guideline for the layout and the choice of the favourable operation mode of the experimental test setup. As a consequence, the latter has been designed for acceleration mode operation of gun lens as well as objective lens and immersion operation, i.e. - unlike standard focused ion beam systems - the interlens drift space is set to a high voltage.

During a second and more detailed system simulation the impact of mutual Coulomb interactions on the predicted system performance could also be considered. Methods have been developed to provide an objective measure for quantifying these interaction effects, and it has been shown that the latter may indeed be considered to have a limiting influence for the achievable probe size in the experimental setup. Consequently, possible approaches towards improving the system performance, such as increasing the ion energy within the interlens drift space and shortening the ion column, have been investigated and may now serve as a guideline for the further system development (see also the following chapter).

In parallel to this theoretical investigations, the practical realisation of the ion beam system was initiated. A reliably operating ion beam column has been developed, that - due to the envisaged operation mode - differs considerably from standard FIB setups. All mechanical system components have been developed newly, with some, e.g. the ion gun, having already been redesigned during the course of this study to provide improved functionality. Here the experience gained from early experimental data - obtained with purpose-built test setups - could be beneficially employed. Additionally, for the manufacturing of the air-tight joints required for the isolation valve, the method of vacuum brazing was successfully

introduced. Furthermore, to enable the above mentioned immersion operation, a number of dedicated power supplies has been designed and realised.

Using dedicated measurement instrumentation, the performance of the low energy focused ion beam system could be experimentally investigated. Due to some remaining limitations, regarding beam alignment and the correction of astigmatism, the theoretically predicted probe sizes could so far not be quite achieved. At this stage measured values deviate by a factor of about two to three: While calculations (beam current 100 pA) predict a probe size of about 200 nm at 2 keV landing energy, experimentally a value of approximately 450 nm has been found. For 3 keV landing energy the corresponding values are 180 nm (calculated) and approximately 350 nm (measured). This discrepancy is expected to be resolved with the ongoing redesign of some of the column components, which, however, primarily aims at further improving the system performance in the light of the simulation results obtained during this study.

Chapter 11

Outlook

The further development of the focused ion beam system aims at overcoming the remaining problems of the current experimental ion beam column with the latter serving as a base system. By using the test setups and measurement instrumentation developed during this study, any gain either achieved by an exchange of individual system components or improvement in the power supply can immediately be assessed.

One factor limiting the achievable resolution in the current setup is the remaining astigmatism, which could not be corrected due to the lack of a suitable power supply. With the completion of the latter some immediate improvement in the system performance may thus be expected.

The ion gun is currently undergoing a further redesign [120]. While the basic emitter-extractor geometry as well as the alignment mechanism will remain largely unaltered, a different ceramic insulator will be adapted to allow the extractor electrode to be contacted from "above". This then will enable the electrical separation between the extractor and the first gun electrode. Additionally the gun will be sealed with the new design, using the CF standard to improve vacuum conditions. In the course of this new development, the gun lens will also be redesigned to guarantee sufficient dielectric strength for acceleration mode operation. Furthermore a simple two stage deflector will be included in the lens housing to allow proper alignment of the beam with respect to the vacuum gradient aperture.

In the future setup the simultaneous use of the differential pumping aperture as a beam limiting aperture will be abolished. Alignment of the latter with respect to the beam axis will be guaranteed by means of a mechanical shift mechanism.

Although the alterations introduced above will most certainly come at the cost of an increaesed component length along the beam direction, the interlens drift space length will be kept constant by incorporating the beam alignment/stigmator unit into the liner tube beyond the host system's entrance port.

Finally, it should be noted that in the course of these envisaged improvements, the overall dielectric strength is to be increased (liner tube voltage up to -10 kV) to allow higher immersion ratios and, consequently, an improved system performance.

Bibliography

[1] P. Gnauck: *Entwicklung einer niederenergetischen Flüssigmetall-Rasterionensonde für die in-situ Ionenätzung im Transmissionselektronenmikroskop.* PhD Thesis University of Tuebingen, 2000.

[2] M. Rauscher, E. Plies: *Abschlußbericht Verbundprojekt "Ionenstrahl-Zielpräparation für die Transmissionselektronenmikroskopie".* http://edok01.tib.uni-hannover.de/edoks/e01fb04/378161385.pdf, 2003.

[3] R. Pantel, G. Mascarin, G. Auvert: *Circuit failure identification using focused ion beam and transmission electron microscopy characterisation techniques.* Microelectr. Eng. **49** (1999) 1818–189.

[4] N. Kato: *Reducing focused ion beam damage to transmission electron microscopy samples.* J. Electron Microsc. **53** (2004) 451–8.

[5] P. Goodhew: *Specimen preparation in materials science.* North-Holland Amsterdam, 1972.

[6] N. Kato, Y. Kohno, H. Saka: *Side-wall damage in a transmission electron microscopy specimen of crystalline Si prepared by focused ion beam etching.* J. Vac. Sci. Technol. A **17** (1999) 1201–4.

[7] R. Langford, A. Petford-Long: *Broad ion beam milling of foused ion beam prepared transmission electron microscopy cross sections for high resolution electron microscopy.* J. Vac. Sci. Technol. A **19** (2001) 982–985.

[8] H.-J. Engelmann: *Advantages and disadvantages of TEM sample preparation using the FIB technique.* Prakt. Metallogr. **40** (2003) 163–174.

[9] E. Kirk, D. Williams, H. Ahmed: *Cross-sectional transmisiion electron microscopy of precisely selected regions from semiconductor devices.* Proc. of the Royal Microscopical Society Conference, Bristol, UK, April 10-13 1989. 501–506.

[10] R. J. Young, J. R. A. Cleaver, H. Ahmed: *Gas-assisted focused ion beam etching for microfabrication and inspection.* Microelectron. Eng. **11** (1990) 409–412.

[11] S. Lipp, L. Frey, F. G., E. Demm, S. Petersen, H. Ryssel: *Local material removal by focused ion beam milling and etching.* Nucl. Instr. Meth. Phys. Res. B **106** (1995) 630–635.

[12] R. Langford, A. Petford-Long: *Preparation of transmission electron microscopy cross-sectioon specimens using focused ion beam milling.* J. Vac.

Sci. Technol. A **19** (2001) 2186–2193.

[13] P. Sudraud, G. Assayag, M. Bon: *Focused ion beam millling, scanning electron microscopy, and focused droplet deposition in a single microsurgery tool.* J. Vac. Sci. Technol. B **6** (1988) 234–238.

[14] P. Gnauck, U. Zeile, W. Rau, M. Schumann: *Real time SEM imaging of FIB milling processes for extended accuracy in cross sectioning and TEM preparation.* Microsc. Microanal. **9** (2003) 524–5.

[15] T. Ishitani, Y. Taniguchi, S. Isakozawa, H. Koike, T. Yaguchi, H. Matsumoto, T. Kamino: *Proposals for exact-oint transmission-electron microscopy using focused ion beam specimen-preparation technique.* J. Vac. Sci. Technol. B **14** (1998) 2532–7.

[16] D. Larson, D. Ford, A. Petford-Long, H. Liew, M. Bamire, A. Cerezo, G. Smith: *Field-ion specimen preparation using focused ion-beam milling.* Ultramicroscopy **79** (1999) 287–293.

[17] A. Yamaguchi, T. Nishikawa: *Low-damage specimen preparation technique for transmission electron microscopy using iodine gas-assisted focused ion beam milling.* J. Vac. Sci. Technol. B **13** (1995) 962–6.

[18] A. Leslie, K. Pey, K. Sim, M. Beh, G. Goh: *TEM sample preparation using FIB: practical problems and artifacts.* Proceedings of 21st International Symposium for Testing and Failure Analysis, Nov 6-10 1995. 353.

[19] R. Langford, A. Petford-Long: *Reduction of the side-wall damage and gallium concentration of focused ion beam prepared TEM cross secions.* Proceedings of the 12th EUREM, Brno, Czech Republic, July 9-14 2000.

[20] C. Burkhardt, , P. Gnauck, E. Plies, W. Nisch: *In-situ ion milling in the Transmission Electron Microscope (TEM) using a Low-Voltage Focused Ion Beam (LVFIB).* Proceedings of the 12th EUREM, Brno, Czech Republic, July 9-14 2000.

[21] J. Walker, R. Broom: *Surface damage of semiconductor TEM samples prepared by focused ion beams.* Inst. Phys. Conf. Ser. No 157 (1997) 473–478.

[22] C. Liu, C. Chen, J. Chio, D. Su: *A methodology to reduce ion beam induced damage in TEM specimens prepared by FIB.* Proc. 28th International Symposium for Testing and Failure Analysis, Phoenix, Arizona, 3-7 November 2002.

[23] Q. Gao, M. Zhang, C. Niou, M. Li, K. Chien: *Sidewall damage induced by FIB milling during TEM sample preparation.* Proceedings of the 42nd Annual International Reliability Physics Sysmposium, Phoenix, Arizona, 2004.

[24] F. Altmann: *TEM Präparation mittels low-voltage FIB.* Oral presentation at the 4th Workshop "Präparative Aspekte der TEM", Oberkochen, 2005.

[25] R. Seliger, J. Wang, V. Wang, R. Kubena: *A high intensity scanning ion probe with submicrometer spot size.* Appl. Phys. Lett. **34** (1979) 310.

[26] K. Gamo: *Low Energy Focused Ion Beam Processing.* Beam Solid Interactions: Fundamentals and Applications Symposium, Boston, MA, USA,

Nov. 30 - Dec. 4 1992. 577–86.

[27] D. Narum, R. Pease: *New technique for modelling focused ion beams*. J. Vac. Sci. Technol. B **4** (1986) 154–8.

[28] S. Hirohata, T. Kosugi, H. Sawaragi, R. Aihara, K. Gamo: *Aberration properties of focused ion-beam induced by space charge effect*. J. Vac. Sci. Technol. B **10** (1992) 2814–6.

[29] V. Zworykin, J. Hillier, R. Snyder: *A scanning electron microscope*. ASTM Bulletin **117** (1942) 15.

[30] I. Müllerová, M. Lenc: *Some approaches to low-voltage scanning electron microscopy*. Ultramicroscopy **41** (1992) 399–410.

[31] H. Rose, D. Preikszas: *Outline of a versatile corrected LEEM*. Optik **91** (1992) 31–44.

[32] A. Recknagel: *Theorie des elektrischen Elektronenmikroskops für Selbststrahler*. Z. Physik **117** (1941) 689–708.

[33] B. Lencová: *Electrostatic lenses*. – In: J. Orloff (ed.): Charged Particle Optics, CRC Press LLC, 1997, 177–222.

[34] J. Frosien, E. Plies, K. Anger: *Compound magnetic and electrostatic lenses for low-voltage applications*. J. Vac. Sci. Technol. B **7** (1989) 1874–7.

[35] E. Weimer, J.-P. Martin: *Development of a new ultra-high performance scanning electron microscope*. Electron Microsc. **I** (1994) 67–8.

[36] J. Orloff, L. Swanson, J.-Z. Li, D. Tuggle: *Beam size in a high resolution ion microprobe operated at high current*. Proceedings of the XIIth International Congress for Electron Microsopy, 1990.

[37] J. Orloff: *An optimized two lens optical column for use with a liquid metal ion source*. Microelectronic Engineering **6** (1987) 327–32.

[38] W. Driesel: *Low-energy ion optical system with a liquid-metal ion source for imaging and processing solid structures*. Ultramicroscopy **52** (1993) 65–72.

[39] G. Shedd, P. Russell: *The effects of low-energy ion impacts on graphite observed by scanning tunneling microscopy*. J. Vac. Sci. Technol. A **9** (1990) 1261–4.

[40] M. Komuro, N. Watanabe, H. Hiroshima: *Focused ion beam etching of Si in chlorine gas*. Jap. J. Appl. Phys. **29** (1990) 2288–91.

[41] A. Steckl, H. Mogul, S. Mogren: *Ultrashallow Si p^+-n junction fabrication by low energy Ga focused ion beam implantation*. J. Vac. Sci. Tecnol. B **8** (1990) 1937–40.

[42] A. Steckl, H. Mogul, S. Novak, C. Magee: *Low energy off-axis focused ion beam Ga implantation into Si*. J. Vac. Sci. Technol. B **9** (1991) 2916–9.

[43] H. Mogul, A. Steckl: *Electrical properties of Si p^+-n junctions for 0.25 μm CMOS fabricated by Ga FIB implantation*. IEEE T. Electron. Dev. **40** (1993) 1823–9.

[44] W. Driesel: *Low-energy ion optical system with a liquid-metal ion source for imaging and processing solid structures*. Ultramicroscopy **52** (1993) 65–72.

[45] K. Pak, T. Shimomura, I. Saitoh, H. Yonezu: *Fabrication of a newly devel-*

oped low-energy focused ion beam system and its application to the maskless selective deposition on microarea. Shinku **35** (1992) 899–904.

[46] K. Pak, I. Saitoh, N. O. H. Yonezu: *In-situ maskless selective area epitaxy of GaAs using a low-energy Ga focused ion beam.* J. Cryst. Growth **140** (1994) 244–7.

[47] P. Nebiker, M. Döbeli, R. Mühle, M. Suter, D. Vetterli: *Low energy ion beam irradiation of silicon.* Nuc. Instr. Meth. Phys. Res. B **113** (1996) 205–8.

[48] D. Vetterli, M. Döbeli, R. Mühle, P. Nebiker, C. Musil: *Characterization of focused ion beam induced damage.* Microelectr. Eng. **27** (1995) 339–42.

[49] T. Chikyow, N. Koguchi, A. Shikanai: *Direct Ga deposition by low-energy focused ion-beam system.* Surf. Sci. **386** (1997) 254–8.

[50] T. Chikyow, N. Koguchi: *GaAs microcrystal growth on semiconductor surfaces by low energy focused ion beam.* J. Vac. Sci. Technol. B **16** (1998) 2538–42.

[51] H. Mayer: *Entwicklung einer Gallium-Flüssigmetall-Ionenquelle und Untersuchung ihrer Eigenschaften und Anwendungsmöglichkeiten.* PhD Thesis, University of Tuebingen, 1987.

[52] H.-P. Mayer, K.-H. Gaukler: *Berechnungen elektrostatischer Abbildungssysteme für Flüssigmetall-Feldionenquellen.* Optik **77** (1987) 129–34.

[53] G. Jones, D. Ritchie, E. Linfield, J. Thompson, A. Hamilton: *Ultrahigh vacuum in situ fabrication of three-dimensional semiconductor structures using a combination of particle beams.* J. Vac. Sci.Technol. B **10** (1992) 2834–7.

[54] J. Thompson, G. Jones, D. Ritchie, E. Linfield, A. Churchill, G. Smith, M. Houlton, D. Lee, C. Whitehouse: *Effect of ion energy on Sn donor activation and defect production in molecular beam epitaxy GaAs doped with Sn ions during growth.* J. Appl. Phys. **74** (1993) 4375–81.

[55] J. Thompson, P. Sazio, H. Beere, G. Jones, D. Ritchie, E. Linfield, G. Smith, M. Houlton, C. Whitehouse: *Low-energy focused ion beam doping duringmolecular beam epitaxial growth for the fabrication of three-dimensional devices: the effect of dopant surface segregation.* Jpn. J. Appl. Phys. **34** (1995) 4477–80.

[56] P. Sazio, J. Thompson, G. Jones, E. Linfield, D. Ritchie, M. Houlton, G. Smith: *Use of very low energy in situ focused ion beams for three-dimensional dopant patterning during molecular beam epitaxial growth.* J. Vac. Sci. Technol. B **14** (1996) 3933–7.

[57] D. Narum, R. Pease: *A variable energy focused ion beam system for in situ microfabrication.* J. Vac. Sci. Technol. B **6** (1988) 966–73.

[58] Y. Yau, T. Groves, R. Pease: *Space charge effects in focused ion beams.* J. Vac. Sci. Technol. B **1** (1983) 1141–4.

[59] D. Narum, R. Pease: *Applications of a variable energy focused ion beam system.* J. Vac. Sci. Technol. B **6** (1988) 2115–9.

[60] H. Lee, R. Pease: *Repair of phase-shift masks using low energy focused ion beams.* Jpn. J. Appl. Phys. **32** (1992) 4474–8.

[61] H. Kasahara, H. Sawaragi, R. Aihara, K. Gamo, S. Namba, M. H. Shearer: *A 0-30 keV low-energy focused ion beam system.* J. Vac. Sci. Technol. B **6** (1988) 974–6.

[62] R. Aihara, H. Kasahara, H. Sawaragi: *Optical system for a low-energy focused ion beam.* J. Vac. Sci. Technol. B **7** (1989) 79–82.

[63] T. Kosugi, R. Mimura, R. Aihara, K. Kemo, S. Namba: *Low energy focused ion beam system and application to low damage microprocess.* Jpn. J. Appl. Phys. **29** (1990) 2295–8.

[64] Software by Munro's Electron Beam Software Limited (MEBS), London, UK, www.mebs.co.uk.

[65] H. Sawaragi, H. Kasahara, R. Mimura, W. Thompson, M. H. Shearer: *A focused ion beam system with a retarding mode objective lens.* J. Vac. Sci. Technol. B **9** (1991) 2613–6.

[66] H. Sawaragi, R. Mimura, H. Kasahara, R. Aihara, W. Thompson, M. H. Shearer: *Performance of a combined focused ion and electron beam system.* J. Vac. Sci. Technol. B **8** (1990) 1846–52.

[67] M. Kinokuni, H. Sawaragi, R. Mimura, R. A. A. Forchel: *Development of wide range energy focused ion beam lithography system.* J. Vac. Sci. Technol. B **16** (1998) 2884–8.

[68] S. Nagamachi, Y. Yakamage, H. Maruno, M. Ueda, S. Sugimoto, M. Asari, J. Ishikawa: *Focused ion beam direct deposition of gold.* Appl. Phys. Lett. **62** (1993) 2143–5.

[69] M. Ueda, S. Nagamachi, Y. Yakamage, H. Maruno, J. Ishikawa: *Low-energy focused ion-beam system for direct deposition.* Proceedings of SPIE, 1995. 396–405.

[70] S. Nagamchi, Y. Yakamage, M. Ueda, H. Maruno, J. Ishikawa: *Focused ion-beam direct deposition of metal thin film.* Rev. Sci. Instrum. **67** (1996) 2351–9.

[71] S. Nagamchi, M. Ueda, Y. Yakamage, H. Maruno, J. Ishikawa: *Optical properties of a low energy focused ion beam apparatus for direct deposition.* Rev. Sci. Instrum. **68** (1997) 2331–8.

[72] J. Yanagisawa, K. Kito, K. Monden, K. Gamo: *Low-energy focused ion beam system and direct depostion of Au and Si.* J. Vac. Sci. Technol. B **13** (1995) 2621–4.

[73] J. Yanagisawa, K. Kito, K. Monden, K. Gamo: *Low energy focused ion beam system combined with molecular beam epitaxy system for fabrication of 3-dimensional buried semiconductor structures.* Proceedings of SPIE, 1995. 406–11.

[74] F. Wakaya, A. Nozawa, J. Yanagisawa, Y. Yuba, S. Takaoka, K. Murase, K. Gamo: *Low energy focused ion beam and buried electron waveguides fabrication.* Miroelectron. Eng. **23** (1994) 123–6.

[75] F. Wakaya, J. Yanagisawa, T. Matsubara, H. Nakayama, Y. Yuba, S. Takaoka, K. Murase, K. Gamo: *Fabrication of buried quantum structures using FIB-MBE total vacuum process*. Microelectron. Eng. **35** (1997) 451–4.

[76] J. Yanagisawa, H. Nakayama, O. Matsuda, K. Murase, K. Gamo: *Direct deposition of silicon and silicon-oxide films using low-energy Si focused ion beams*. Nucl. Instr. Meth. Phys. Res. B **127/128** (1997) 893–6.

[77] J. E. Barth, P. Kruit: *Addition of different contributions to the charged particle probe size*. Optik **101** (1996) 101–9.

[78] C.-D. Bubeck, A. Fleischmann, G. Knell, R. Y. Lutsch, E. Plies, D. Winkler: *Miniature electrostatic lens for generation of a low-voltage high current electron probe*. Nucl. Instr. Meth. A **427** (1999) 104–108.

[79] G. Knell: *Optmierung von megnetisch-elektrostatischen Detektor-Objektivlinsen für die Niederspannungs-Rasterelektronenmiroskopie*. University of Tübingen, 1999.

[80] L. Wang: *Design optimization for two lens focused ion beam columns*. J. Vac. Sci. Technol. B **15** (1997) 833–39.

[81] Z. Shao, Y. Wang: *On the optimization of ion microprobes*. J.Vac.Sci.Technol.B **8** (1990) 95–9.

[82] T. Ishitani, Y. Kawanami: *Coarse guidelines in designing focused ion beam optics*. J. Vac. Sci. Technol. B **13** (1995) 371–4.

[83] K. Sakaguchi, T. Sekine: *Focused ion beam optical column design and consideration on minimum attainable beam size*. J. Vac. Sci. Technol. B **16** (1998) 2462–68.

[84] E. Kasper, W. Scherle: *On the analytical calculation of fields in electron optical devices*. Optik **60** (1982) 339–52.

[85] E. Plies: *Electron optics of low-voltage electron beam testing and inspection. Part I: Simulation tools*. Adv. Opt. Electron Microscopy **13** (1994) 123–242.

[86] E. Kasper: *An advanced method for the direct calculation of electron optial aberration discs*. Optik **89** (1991) 23–30.

[87] E. Munro: *Computer-aided design methods in electron optics*. Cambridge University, 1971.

[88] E. Munro, H. C. Chu: *Numerical analysis of electron beam lithography systems. Part II: Computaion of fields in electrostatic deflectors*. Optik **61** (1982) 1–16.

[89] E. Munro, H. C. Chu: *Numerical analysis of electron beam lithography systems. Part III: Calculation of the optical properties of electron focusing systems and dual-channel deflection systems with combined magnetic and electrostatic fields*. Optik **61** (1982) 121–145.

[90] R. Seeliger: *Ein neues Verfahren zur Bestimmung des Öffnungsfehlers vonElektronenlinsen*. Optik **4** (1948) 258.

[91] J. Orloff, L. Swanson: *An asymmetric electrostatic lens for field-emission microprobe applications*. J. Appl. Phys. **50** (1979).

[92] L. Swanson, G. Schwind, A. Bell: *Emission characteristics of a liquid gal-*

lium ion source. Scanning Electron Microscopy (1979) 45–51.

[93] D. Kern: *Theoretische Untersuchungne an rotationssymmetrischen Strahlerzeugungssystemen mit Feldemissionsquelle*. Universität Tübingen, 1978.

[94] M. Lehmann: *Determination and correction of the coherent wave aberration from a single off-axis hologram by means of a genetic algorithm*. Ultramicroscopy **85** (2000) 165–82.

[95] G. Jansen: *Coulomb interactions in particle beams (Adv. Electron. Electron. Phys., Suppl. 21)*. Academic Press, New York, 1990.

[96] P. Kruit, G. Jansen: *Space charge and statistical Coulomb effects*. – In: J. Orloff (ed.): Charged Particle Optics, CRC Press LLC, 1997, 275–318.

[97] H. Rose, R. Spehr: *On the theory of the Boersch effect*. Optik **57** (1980) 339–364.

[98] H. Rose, R. Spehr: *Energy broadening in high-density electron and ion beams: The Boersch effect*. Advances in Electronics and Electron Physics, Supplement **13C** (1983) 475–530.

[99] M. Rauscher, E. Plies: *Optimum mode of operation for a low energy focused ion beam system*. J. Vac. Sci. Technol. **22** (2004) 3004–7.

[100] M. Rauscher, E. Plies: *Impact of Coulomb interactions on the performance of a low energy focused ion beam system*. J. Appl. Phys. **97** (2005) 064908.

[101] P. Kruit, X. Jiang: *Influence of Coulomb interactions on choice of magnification, aperture size, and source brightness in a two lens focused ion beam column*. J. Vac. Sci. Technol. B **14** (1996) 1635–41.

[102] P. Prewett, G. Mair, S. Thompson: *Some comments on the mechanism of emission from liquid metal ion sources*. J.Phys.D: Appl.Phys. **15** (1982) 1339–48.

[103] L. Swanson: *Liquid metal ion sources: mechanisms and applications*. Nucl. Instrum. Meth. Phys. Res. **218** (1983) 347–53.

[104] G. Mair, T. Mulvey: *Liquid metal ion sources in ion microscopy and secondary ion mass spectrometry*. Scanning Electron Microscopy (1985) 959–71.

[105] C. Burkhardt: *Private Communication*.

[106] L. Bischoff, J. Teichert, S. Hausmann, T. Ganetsos, G. Mair: *Investigation and optimization of the emission parameters of alloy liquid metal ion sources*. Nucl. Instr. Meth. Phys. Res. B **161** (2000) 1128–31.

[107] L. Bischoff: *Alloy liquid metal ion sources and their application in mass separated focused ion beams*. Ultramicroscopy **103** (2005) 59–66.

[108] F. Hasselbach: *A ruggedized miniaturized UHV electron biprism interferometer for new fundamental experiments and applications*. Z. Phys. B - Condensed Matter **71** (1988) 443–9.

[109] K. Marianowski: *Private communication*. 2005.

[110] M. Kienle: *Aufbau und Erprobung eines außeraxialen Vielkanalspektrometers für Sekundärelektronen*. PhD Thesis University of Tuebingen, 2002.

[111] J. Baertle: *Berechnung und Bau eines elektrostatischen 12-Pol-Elements*. Diploma thesis University of Tuebingen, 1999.

[112] S. Schubert, R. Lutsch, M. Rauscher, E. Plies: *A miniaturised electrostatic column for high probe current.* Mitteilungen Deutsch. Ges. Elektronenmikroskopie **24** (2003) 12–3.

[113] M. Wutz, H. Adam, W. Walcher, K. Jousten: *Handbuch Vakuumtechnik*. Vieweg Braunschweig, 2000.

[114] A. Hollemann, E. Wiberg: *Lehrbuch der Anorganischen Chemie*. Walter de Gruyter, Berlin New York, 1995.

[115] N. Ollmert: *Bestimmung der Ortsauflösung im Rasterelektronenmikroskop*. Diploma thesis University of Tuebingen, 1995.

[116] D. Dennis: *Entwicklung einer rechnergesteuerten Stigmatorversorgung für die Rasterionenmikroskopie*. Master Thesis University of Applied Science Esslingen, 2005.

[117] M. Rauscher: *Aufbau und Erprobung einer Rastereinheit zur Bestimmung der Auflösung eines miniaturisierten elektrostatischen Linsensystems*. Master Thesis University of Tuebingen, 2001.

[118] Y. Lutsch: *Miniaturisierte elektrostatische Linsen aus konventionellen Blenden für die hochauflösende Niederspannungs-Rasterelektronenmikroskopie*. Dissertation University of Tuebingen, 2002.

[119] D. Chescoe, P. Goodhew: *The operation of transmission and scanning electron microscopes*. Royal Microscopical Society, 1990.

[120] K. Marianowski: *Entwicklung und Test eines verbesserten Strahlkopf- und Strahlerlinsendesigns für eine niederenergetische Rasterionensäule*. Master Thesis University of Tuebingen, 2006.